Published for SISSA by Springer

Received: *August 28, 2023*
Revised: *April 15, 2024*
Accepted: *April 17, 2024*
Published: *May 14, 2024*

Electron and photon efficiencies in LHC Run 2 with the ATLAS experiment

The ATLAS collaboration

E-mail: atlas.publications@cern.ch

Abstract: Precision measurements of electron reconstruction, identification, and isolation efficiencies and photon identification efficiencies are presented. They use the full Run 2 data sample collected by the ATLAS experiment in *pp* collisions at a centre-of-mass energy of 13 TeV during the years 2015–2018, corresponding to an integrated luminosity of 139 fb^{-1}. The measured electron identification efficiencies have uncertainties that are around 30%–50% smaller than the previous Run 2 results due to an improved methodology and the inclusion of more data. A better pile-up subtraction method leads to electron isolation efficiencies that are more independent of the amount of pile-up activity. Updated photon identification efficiencies are also presented, using the full Run 2 data. When compared to the previous measurement, a 30%–40% smaller uncertainty is observed on the photon identification efficiencies, thanks to the increased amount of available data.

Keywords: Hadron-Hadron Scattering

ArXiv ePrint: 2308.13362

https://doi.org/10.1007/JHEP05(2024)162

JHEP05(2024)162

Contents

1 Introduction

The ATLAS detector [1–3] at the Large Hadron Collider (LHC) [4] is used to investigate proton-proton collisions at the highest energies. After the discovery of the Higgs boson in 2012 using four-lepton and diphoton final states [5, 6] and following the deeper understanding of the detector and the hadron collider environment, precision measurements of Standard

JHEP05(2024)162

Model parameters are increasingly viable. Measurements of the weak mixing angle [7], the W boson mass [8] and related cross-sections [9, 10] have proven to be competitive to prior determinations at the LEP or Tevatron colliders. In addition, precision measurements of the Higgs boson properties have become an active area of research [11]. These experimentally challenging precision measurements rely on understanding and controlling the systematic uncertainties of the object reconstruction in the detector extremely well. Electrons and photons are pivotal final state objects in these measurements. This paper describes the performance of electron and photon identification achieved for precision measurements in the LHC Run 2 data taking period (2015–2018).

The methodology to determine the efficiency of electron identification and isolation selection has been significantly updated with respect to what was used for previous publications [12–14], as have the related factors to correct the detector simulation to accurately reflect the data efficiencies. The electron reconstruction efficiencies have been measured using the full Run 2 data. The measurements of the photon efficiencies have been updated to profit from the increased statistics. The results presented here are intended to be the final and most precise for the *pp* collision data taken by the ATLAS experiment during LHC Run 2. They cover the full $\sqrt{s} = 13$ TeV data sample and also include the 2018 data, which is 70% larger than 2015–2017 data sample used for the previous results [13, 14].

Data samples of electrons and photons are recorded using electron and photon triggers whose performance during LHC Run 2 is detailed in ref. [15]. Reconstruction algorithms and energy calibrations are described in refs. [14, 16]. The work presented here is based on these triggering, reconstruction and calibration algorithms. Section 2 introduces the ATLAS detector. A short reminder of how electron and photon objects are reconstructed from the detector signals is given in section 3, followed by an overview of the data samples used in section 4. The general definition of the efficiency measurement along with a description of the changes in methodology are found in section 5, with results on electron reconstruction and identification efficiencies given in section 6 and 7, respectively. Section 8 reports the rejections against backgrounds achieved with the electron reconstruction and identification requirements. Improvements to the pile-up subtraction for the calorimeter isolation and the resulting electron isolation efficiencies are described in section 9. The photon reconstruction efficiency has not been remeasured and is reported in ref. [14]. The photon identification efficiencies can be found in section 10. This paper concludes with section 11.

2 ATLAS detector

The ATLAS detector [1–3] at the LHC covers nearly the entire solid angle around the collision point.[1] It consists of an inner tracking detector surrounded by a thin superconducting

[1] ATLAS uses a right-handed coordinate system with its origin at the nominal interaction point (IP) in the centre of the detector and the z-axis along the beam pipe. The x-axis points from the IP to the centre of the LHC ring, and the y-axis points upwards. Cylindrical coordinates (r, ϕ) are used in the transverse plane, ϕ being the azimuthal angle around the z-axis. The pseudorapidity is defined in terms of the polar angle θ as $\eta = -\ln\tan(\theta/2)$. Angular distance is measured in units of $\Delta R \equiv \sqrt{(\Delta\eta)^2 + (\Delta\phi)^2}$. The transverse energy is $E_{\mathrm{T}} = E/\cosh(\eta)$.

solenoid, electromagnetic and hadron calorimeters, and a muon spectrometer incorporating three large superconducting air-core toroidal magnets.

The inner-detector system (ID) is immersed in a 2 T axial magnetic field and provides charged-particle tracking in the range of $|\eta| < 2.5$. The high-granularity silicon pixel detector covers the vertex region and typically provides four measurements per track, the first hit normally being in the insertable B-layer installed before Run 2 [2, 3]. It is followed by the silicon microstrip tracker (SCT), which usually provides eight measurements per track. These silicon detectors are complemented by the transition radiation tracker (TRT), which enables radially extended track reconstruction up to $|\eta| = 2.0$. The TRT provides electron identification capability through the detection of transition radiation photons. It consists of small-radius drift tubes ('straws') interleaved with a polymer material creating transition radiation for particles with a large Lorentz factor. This radiation is absorbed by the Xe-based gas mixture filling the straws, discriminating electrons from hadrons over a wide energy range. Due to gas leaks, some TRT modules are filled with an Ar-based gas mixture. The ID is surrounded by a superconducting solenoid producing a 2 T magnetic field that ensures an accurate reconstruction of tracks from the primary *pp* collision region. It also ensures the identification of tracks from secondary vertices, permitting an efficient reconstruction of photon conversions in the ID up to a radius of about 800 mm.

The calorimeter system covers the pseudorapidity range $|\eta| < 4.9$. The electromagnetic (EM) calorimeter is a lead/liquid-argon (LAr) sampling calorimeter with an accordion geometry. It is divided into a barrel section (EMB) covering the pseudorapidity region $|\eta| < 1.475$,[2] and two endcap sections (EMEC) covering $1.375 < |\eta| < 3.2$. The barrel and endcap calorimeters are immersed in three LAr-filled cryostats, and are radially segmented into three layers for $|\eta| < 2.5$. The first layer, covering $|\eta| < 1.4$ and $1.5 < |\eta| < 2.4$, has a thickness of about 4.4 radiation lengths (X_0) and is finely segmented in the η direction, typically 0.003×0.1 in $\Delta\eta \times \Delta\phi$ in the EMB, to provide an event-by-event discrimination between single-photon showers and overlapping showers from the decays of neutral hadrons. The second layer, which collects most of the energy deposited in the calorimeter by photon and electron showers, has a thickness of about $17X_0$ and a granularity of 0.025×0.025 in $\Delta\eta \times \Delta\phi$. A third layer, which has a granularity of 0.05×0.025 in $\Delta\eta \times \Delta\phi$ and a depth of about $2X_0$, is used to correct for leakage beyond the EM calorimeter for high-energy showers. In front of the accordion calorimeter, a thin presampler layer (PS), covering the pseudorapidity interval $|\eta| < 1.8$, is used to correct for energy loss upstream of the calorimeter. The PS consists of an active LAr layer with a thickness of 1.1 cm (0.5 cm) in the barrel (endcap) and has a granularity of $\Delta\eta \times \Delta\phi = 0.025 \times 0.1$. The transition region between the EMB and the EMEC, $1.37 < |\eta| < 1.52$, has a large amount of material in front of the first active calorimeter layer ranging from $5X_0$ to almost $10X_0$. This section is instrumented with scintillators located between the barrel and endcap cryostats, and covering up to $|\eta| = 1.6$.

The hadronic calorimeter, surrounding the EM calorimeter, consists of a steel/scintillator tile calorimeter in the range of $|\eta| < 1.7$ and two copper/LAr calorimeters spanning $1.5 < |\eta| < 3.2$. The acceptance is extended by two copper/LAr and tungsten/LAr forward calorimeters extending up to $|\eta| = 4.9$, and hosted in the same cryostats as the EMEC.

[2]The EMB is split into two half-barrel modules, which cover the positive and negative η regions.

The muon spectrometer comprises separate trigger and high-precision tracking chambers measuring the deflection of muons in a magnetic field generated by the superconducting air-core toroidal magnets. Three layers of precision tracking chambers covers the region $|\eta| < 2.7$, complemented by cathode-strip chambers in the forward region, where the background is highest. The muon trigger system covers the range $|\eta| < 2.4$.

Events are selected by the first-level trigger system implemented in custom hardware, followed by selections made by algorithms implemented in software in the high-level trigger [17]. The first-level trigger accepts events from the 40 MHz bunch crossings at a rate below 100 kHz, which the high-level trigger further reduces to record events to disk at about 1 kHz.

An extensive software suite [18] is used in data simulation, in the reconstruction and analysis of real and simulated data, in detector operations, and in the trigger and data acquisition systems of the experiment.

3 Electron and photon objects

3.1 Reconstruction of electron and photon candidates

The reconstruction of electron and photon objects starts from variable-sized topological clusters combining cells from the EM and hadronic calorimeters [19, 20]. The energies of the EM calorimeter cells in the cluster are used to reconstruct the EM energy of the cluster. Those clusters that have an EM energy above 400 MeV and a ratio of EM energy to the total cluster energy above 0.5 [14] are selected as so-called EM topo-clusters. These EM topo-clusters are considered for further use in electron and photon reconstruction [14].

Tracks are reconstructed in the ID [13, 14] using either the standard track reconstruction [21] or an alternative procedure that accounts for energy losses due to bremsstrahlung in the pattern recognition [13]. Using a sliding window algorithm on EM calorimeter cells [19], tracks can be loosely matched to fixed-sized clusters. They are then refitted with a Gaussian sum filter algorithm to improve the accuracy of the fitted track parameters. These tracks are then further used for electron and photon reconstruction.

Initial electron candidates are reconstructed from the EM topo-clusters described above that are matched to one or several tracks. The primary track of the electron is chosen using a metric that depends on the extrapolation of the track from the perigee to the second layer of the EM calorimeter and uses either the measured track momentum or the magnitude of its momentum that has been rescaled to match the cluster energy. Details of the matching criteria and the ranking in case more than one track can be matched are described in ref. [13].

Initial photon candidates can either be reconstructed as converted or unconverted photon candidates.[3] A converted photon object is based on an EM topo-cluster matched to one or several conversion vertices. The tracks described above are used to reconstruct the conversion vertices following the procedure described in refs. [14, 22, 23]. Two types of vertices are employed: two-track conversion vertices using opposite-charged tracks and single-track conversion vertices using single tracks without hits in the innermost sensitive layers.

[3] In ATLAS, around 30% of photons convert in the detector material before the LAr calorimeter. Because of the very different shower development, the identification, isolation and calibration of converted or unconverted photons is done separately.

The matching of the conversion vertices to the EM topo-cluster is based on the extrapolation of the conversion candidate to the second sampling layer of the calorimeter. The difference of the extrapolated η and ϕ coordinates of the conversion and the EM topo-cluster centre is required to be smaller than 0.05 or 0.1 for double- or single-track conversions, respectively. An unconverted photon is reconstructed from an EM topo-cluster that is not matched to an electron track or a conversion vertex.

Using these initial electron and photon candidates, the final EM clusters are built from all clusters matched to the candidates. If an electron candidate has undergone bremsstrahlung radiation, which mostly occurs in the bending plane, it might be reconstructed as two clusters. This happens for about 10% of the clusters, mainly in the forward and the transition regions [14]. Therefore for all electron and photon candidates, nearby EM topo-clusters are merged to form the final EM cluster. Starting from the highest-energy EM cluster, nearby clusters within $\Delta\eta \times \Delta\phi = 0.075 \times 0.125$ of their respective barycentres are merged with the initial cluster unless they were already used. For electrons and converted photons, additional clusters within $\Delta\eta \times \Delta\phi = 0.125 \times 0.3$ are considered if their best matched track or conversion vertex is the same as for the original cluster. These final EM clusters are retained as part of the electron and photon objects and can also be referred to as superclusters [14]. After applying initial position corrections and energy calibrations to the merged EM clusters, the track and conversion vertex matching procedures are repeated to build electron and photon objects. Their energies are again calibrated using the procedure described in refs. [14, 16].

3.2 Selection of electron and photon candidates

As a final step, discriminating variables are constructed to separate prompt electrons or photons from background objects. In this context, prompt electrons or photons are understood to be stemming from the hard-scattering vertex or from the decay of heavy resonances such as Higgs, W, and Z bosons, whilst background objects are jets misidentified as electrons or photons, non-prompt electrons from decays of b- and c-hadrons, or even electrons misreconstructed as photons and vice versa. The discriminating variables can be grouped into three types that are either related to properties of the track, the shower development in the different layers of the calorimeter, or the matching between the track and the calorimetric cluster. For both electrons and photons, these identification selection requirements are applied as a function of $|\eta|$ and transverse energy (E_{T}). A detailed overview of their definition is given in table 1 of ref. [14]. For the identification of electrons, these variables are combined into a likelihood classifier, as detailed in ref. [14]. Three sets of identification selection requirements are defined (Loose, Medium, and Tight), which correspond to increasingly restrictive selections [13] and hence increasingly suppressed background, at the cost of also reducing signal acceptance. These identification requirements are valid in the pseudorapidity range $|\eta| < 2.47$.

Photons are identified in the pseudorapidity range $|\eta| < 2.37$ using sets of selection criteria [22] on EM shower shape variables. Three identification selection criteria exist, named Loose, Medium and Tight. The former two are employed in the trigger, whilst the Tight criterion is the primary photon identification selection employed for ATLAS analyses. They are defined in ref. [14].

JHEP05(2024)162

A number of different isolation variables exist. The photon isolation has not been updated with regards to ref. [14] and is not discussed further in this publication. The electron calorimeter isolation [13], $E_{\mathrm{T}}^{\mathrm{coneXX}}$, is calculated by summing the transverse energy of positive-energy topological clusters[4] whose barycentre falls within a cone centred around the electron cluster barycentre. Here, XX refers to the size of the employed cone, $\Delta R = \mathrm{XX}/100$. Frequently, XX is set to 20 for calorimeter isolation. The energy of the electron itself, as well as contributions from pile-up activity, are subtracted using the methodology described in section 9. The track isolation variable ($p_{\mathrm{T}}^{\mathrm{coneXX}}$) is defined as the scalar sum of the transverse momenta of selected tracks within a cone of size $\Delta R = \mathrm{XX}/100$ centred around the electron track direction. For track isolation, XX is often set to 20 or 30. The tracks are required to originate from the primary vertex of the event[5] and to fulfil minimum quality requirements as detailed in ref. [14]. Tracks matched to the electron cluster are in general excluded from the calculation; however, refining the procedure documented in ref. [14], tracks that are further than $|\Delta\eta| > 0.01$[6] away from the primary electron track are still added to the isolation cone. This improves the background rejection for $E_{\mathrm{T}} > 100$ GeV significantly compared with previous publications. In simulated $t\bar{t}$ events,[7] the rejection is larger by more than a factor of two, depending on the electron identification and isolation selection, without degrading the prompt-electron efficiency. For prompt electrons produced in cascade decays of high-momentum heavy particles where other decay products can be very close to the electron direction, an alternative track isolation is defined with a variable cone size ($p_{\mathrm{T}}^{\mathrm{varconeXX}}$). In this case, the cone size shrinks for larger transverse momentum of the primary electron candidate:

$$\Delta R = \min\left(\frac{10}{E_{\mathrm{T}}[\mathrm{GeV}]}, \Delta R_{\mathrm{max}}\right), \tag{3.1}$$

where $\Delta R_{\mathrm{max}} = \mathrm{XX}_{\mathrm{max}}/100$ is the maximum cone size.

4 Datasets and simulated-event samples

4.1 Selection of the data

The studies documented in this paper use the full pp collision data recorded by the ATLAS detector between 2015 and 2018 (Run 2), with the LHC operating at a centre-of-mass energy of $\sqrt{s} = 13$ TeV and a bunch spacing of 25 ns. In this period, the LHC delivered colliding beams with a peak instantaneous luminosity up to $L = 2.1 \times 10^{34}\,\mathrm{cm}^{-2}\mathrm{s}^{-1}$, achieved in 2018,

[4]The LAr signal is electronically shaped to suppress noise contributions [24] which in some cases cause fluctuations to lead to cells being reconstructed with negative energies. As the signal-over-noise criterion for topological cluster formation uses the absolute energies [19], clusters can be reconstructed with negative energy but are not considered here.

[5]The primary vertex is defined to be the one with the largest scalar sum of transverse momenta of the associated tracks.

[6]$\Delta\eta$ is evaluated after the tracks have been extrapolated to the EM calorimeter.

[7]Simulated using the Powheg Box v2 [25–28] generator at next-to-leading-order QCD with the NNPDF3.0nlo [29] PDF set and the h_{damp} parameter set to 1.5 times the top quark mass [30]. The events were interfaced to Pythia 8.230 [31] to model the parton shower, hadronisation, and underlying event, with parameters set according to the A14 tune [32] and using the NNPDF2.3lo set of PDFs [33]. The decays of bottom and charm hadrons were performed by EvtGen 1.6.0 [34].

and an average number of pp interactions per bunch crossing $\langle\mu\rangle$ of 13, 25, 38, and 34 for 2015, 2016, 2017, and 2018 data, respectively. After applying beam, detector, and data-quality criteria the total integrated luminosity of the data is $139\,\mathrm{fb}^{-1}$ [35]. The uncertainty in the combined 2015–2018 integrated luminosity is 1.7% [36], obtained using the LUCID-2 detector [37] for the primary luminosity measurements.[8]

The measurements of the electron reconstruction, identification and isolation efficiencies use a large sample of $Z \to e^+e^-$ events selected with single-electron triggers. The single-electron high-level trigger has an E_T threshold ranging from 24 GeV in 2015 and most of 2016 to 26 GeV at the end of 2016, and during 2017 and 2018; it requires a Tight identification and loose tracking-based isolation criteria [14].

A sample of $J/\psi \to e^+e^-$ events was collected for studies with low-E_T electrons using dedicated prescaled dielectron triggers with asymmetric electron E_T thresholds ranging from 4 to 14 GeV. Each of these triggers requires Tight trigger identification and E_T above a certain threshold for one trigger object, while only requiring the electromagnetic cluster E_T to be higher than some other (lower) threshold for the second object.

Samples of $Z \to \ell^+\ell^-\gamma$ events (with ℓ being an electron or a muon), used to measure photon identification efficiency at low E_T, are selected with the same non-prescaled single-lepton triggers as the $Z \to e^+e^-$ events described above. Additionally, dielectron triggers are used with electron E_T thresholds ranging from 12 to 24 GeV and Loose identification. Events with Z boson decays into muons are selected using a single muon with a loose tracking-based isolation criterion and a transverse momentum threshold of 26 GeV and a dimuon trigger with p_T thresholds at 14 GeV [15, 39]. The muons are reconstructed as described in ref. [40].

Inclusive QCD samples and inclusive-photon production samples, used to measure photon identification efficiency at high E_T, are selected with prescaled and non-prescaled single-photon triggers [15] with Loose identification. The lowest transverse energy threshold of these triggers is 10 GeV.

4.2 Monte Carlo event simulation

Various Monte Carlo (MC) event generators were employed to simulate the signal and background samples ($Z \to e^+e^-$, $J/\psi \to e^+e^-$, $Z \to e^+e^-\gamma$, $Z \to \mu^+\mu^-\gamma$, inclusive-photon production and tree-level $2 \to 2$ QCD production including also top-quark pair and weak vector-boson production). These were used to perform the studies discussed in this paper. Simulation details additional to those provided below can be found in ref. [14].

The generated signal and background events were processed through the full ATLAS detector simulation [41] based on Geant4 [42]. The MC events were simulated with additional interactions in the same or neighbouring bunch crossings to match the pile-up conditions during LHC operations. The overlaid pp collisions were generated with the soft QCD processes of Pythia8 [31] using the A3 set of tuned parameters [43] and the NNPDF2.3lo PDF set [33]. Although this set of tuned parameters improves the modelling of minimum-bias data relative to the set used in the past (A2 [44]), it overestimates by roughly 3% the hadronic

[8] The final luminosity for Run 2 was determined be $140\,\mathrm{fb}^{-1}$ with an uncertainty of 0.83% [38]. The impact on the presented efficiency measurement is fully negligible. Therefore the presented results have not been updated using the new integrated luminosity.

activity as measured using charged-particle tracks. Simulated events were reweighted to reproduce the distribution of the average number of interactions per bunch crossing in data, scaled down by a factor 1.03 [45].

Studies presented throughout this paper using MC simulation select electrons originating from $Z \to e^+e^-$ or $J/\psi \to e^+e^-$ decays, or photons from $Z \to \ell^+\ell^-\gamma$, inclusive-photon production samples, or other processes using generator-level information. The matching of the reconstructed and generated electrons is based on their ID track [46]. The reconstructed electrons are classified as genuine if this track is reconstructed from the primary electron, or from secondary particles produced in a material interaction of the primary electron or of final state radiation emitted collinearly. Reconstructed and generator-level photons are matched based on their distance in η–ϕ space between the EM cluster barycentre and the extrapolation of the photon direction to the 2nd layer of the EM calorimeter.[9]

5 Electron efficiency measurements

The efficiency of reconstructing, triggering on, and selecting a genuine, prompt electron can be factorized into different terms:

$$\varepsilon_{\text{total}} = \varepsilon_{\text{EMclus}} \times \varepsilon_{\text{reco}} \times \varepsilon_{\text{id}} \times \varepsilon_{\text{iso}} \times \varepsilon_{\text{trigger}}. \tag{5.1}$$

In equation (5.1), $\varepsilon_{\text{EMclus}}$ is the probability to reconstruct an EM-cluster given a genuine electron. This efficiency is computed as the ratio of the number of reconstructed EM clusters, N_{cluster}, and the number of produced electrons, N_{all}. It is evaluated entirely from MC simulation, where the reconstructed cluster is associated to a genuine electron produced at generator level, and is found to be above 99% for electrons with $E_{\text{T}} > 10$ GeV [14].

The reconstruction efficiency, $\varepsilon_{\text{reco}}$, reflects the performance of the track reconstruction and its association with the cluster. It is obtained from the number of reconstructed electron candidates with a track, N_{reco}, divided by the number of EM cluster candidates, N_{cluster}. The identification efficiency, ε_{id}, is the probability of a reconstructed electron to satisfy a certain identification criterion. It is defined as the number of identified and reconstructed electron candidates, N_{id}, divided by N_{reco}. The isolation efficiency, ε_{iso}, is the probability of an identified electron to pass requirements on the track or calorimeter isolation. It is calculated as the number of identified electron candidates satisfying the isolation, identification, and reconstruction requirements, N_{iso}, divided by N_{id}. Only $\varepsilon_{\text{reco}}$, ε_{id}, ε_{iso} efficiencies are further discussed in this paper.

Finally, the trigger efficiency, $\varepsilon_{\text{trigger}}$, is calculated as the number of (reconstructed, identified, and isolated) electron candidates passing the trigger requirements, N_{trig}, divided by N_{iso} [15].

All efficiencies except $\varepsilon_{\text{EMclus}}$ are estimated directly from data using tag-and-probe methods that select from unbiased samples of electrons produced in the decays of well-known resonances, such as $Z \to e^+e^-$ or $J/\psi \to e^+e^-$, unbiased samples of electrons produced in

[9]In an elliptical cone of $\eta \times \phi = 0.025 \times 0.5$ the highest E_{T} generator-photon is chosen as a match. If none is found, the leading particle in the cone is matched instead independent of particle type. If no particle is found, the closest particle in a cone of $\Delta R = 0.1$ is used.

the particle's decay. One of the electrons must satisfy strict selection requirements and serves as a tag, while the second electron serves as a probe. The efficiency of a given requirement is then computed by applying it to the probe sample after accounting for residual background contamination [12–14]. If both the electrons satisfy the tag requirements, each of them are used as tag and the event provides two probes. This is necessary in order not to bias the probe selection.

The biggest challenge in the efficiency measurements is the estimation of probes that originate from background rather than signal processes. This background is largest for the sample of cluster probes, but the fraction of such events is reduced with each efficiency step given in equation (5.1), from left to right. Various data-based background estimation methods are used as described in the relevant sections below.

The accuracy of the observed electron efficiency plays an important role when using MC simulation to predict physics processes. In order to achieve reliable results, the MC simulated events need to be corrected to reproduce as closely as possible the efficiencies measured in data. This is achieved by applying a multiplicative correction factor in the MC simulation in addition to the other event weights that are used e.g to scale to luminosity, or to accurately reflect the detector resolution. The correction factor to improve the modelling of the efficiency is defined as the ratio of the efficiency measured in data to that determined from MC events where the same efficiency measurement method is used in both the data and MC simulation. A dedicated correction factor is measured for each of the efficiencies in equation (5.1) separately. The advantage of using these correction factors is that they are universally applicable whilst absolute efficiencies might differ from physics process to physics process. As shown below, these correction factors are normally close to unity with deviations arising from a mismodelling in the simulation of tracking properties, shower shapes in the calorimeters, or the isolation from other energy deposits. As their application brings data and MC simulation closer together, this helps to remove biases from predictions and to avoid constraints and shifts in likelihood fits when extracting results.

Systematic uncertainties in the correction factors are evaluated by varying the requirements on the selection of the candidate sample, as well as varying the details of the background-subtraction [12–14]. How these variations are used to construct the central values and their uncertainties depends on the method used and is described in the respective method sections below.

The statistical uncertainty of the efficiency in a single variation of the measurement is calculated assuming a binomial distribution. The statistical uncertainty related to the subtracted background is also included in the overall statistical uncertainty.

6 Electron reconstruction

The electron reconstruction efficiency, $\varepsilon_{\text{reco}}$, is measured in bins of electron E_{T} and η with bin edges at $E_{\text{T}} = \{15, 20, 25, 30, 35, 40, 45, 50, 60, 80, 150, \infty\}$ GeV and $\eta = \pm\{0, 0.1, 0.6, 0.8, 1.15, 1.37, 1.52, 1.81, 2.01, 2.37, 2.47\}$. The binning in η is driven by the detector geometry, e.g. the transition region between EMB and EMEC ($1.37 < |\eta| < 1.52$), the acceptance of the presampler ($|\eta| < 1.81$) and the region where the strip granularity changes to be coarser ($|\eta| = 2.37$).

JHEP05(2024)162

The electron reconstruction efficiency is only measured for $E_{\mathrm{T}} > 15$ GeV. Below 15 GeV, the large backgrounds make the measurement unreliable and using low-mass resonances like J/ψ is equally challenging. The electron reconstruction efficiency is defined as the efficiency to reconstruct a prompt electron with a good quality track[10] and with a good quality cluster[11] from all reconstructed EM clusters. Including track and cluster quality requirements in the measurement of the reconstruction efficiency reduces it by about 0.5% compared to the previous publications [14].

The measurements are performed using a tag-and-probe method based on the $Z \to e^+e^-$ invariant mass to estimate both the signal and background as described in ref. [47]. Events are recorded using the single-electron triggers described in section 4. An event must have at least one tag electron with $E_{\mathrm{T}} > 25$ GeV outside the calorimeter transition region $1.37 < |\eta| < 1.52$. It must pass the Tight identification. To estimate systematic uncertainties, two alternative tag selection requirements are used that vary the amount of backgrounds and thus test the robustness of the background estimate: either the Medium or Tight identification, both in combination with an isolation criterion of $E_{\mathrm{T}}^{\mathrm{cone40}} < 5$ GeV. The tag must be associated with the object that fired the trigger. Additionally, a probe object must be present, defined as a reconstructed EM cluster that is isolated by $\Delta R > 0.4$ from any jet reconstructed with the anti-k_{T} algorithm [48, 49] using a radius parameter of 0.4 with $p_{\mathrm{T}} > 20$ GeV. Candidates that are likely to stem from a photon conversion are discarded [14]. The invariant mass of the tag and the probe is restricted to be in the range $m_{ee} \in [60, 250]$ GeV and only the highest-mass pair is chosen in case there is more than one. No charge requirements are applied.

The measurement of the reconstruction efficiencies uses separate methods to estimate backgrounds from data for EM clusters *with and without* an associated track:

1. For the sample of EM cluster with associated tracks, non-electron backgrounds are estimated using a template created by inverting identification and isolation selection requirements on the probe to select a pure background sample [12, 47]. Two different variations of this background selection are used, each of which is normalised simultaneously in the low and high mass region of the invariant mass distribution ([60, 70] GeV and [120, 250] GeV respectively).

2. For the sample of EM clusters without associated tracks, it is difficult to construct a data-driven template. Therefore, backgrounds from photons or jets are determined using a third order polynomial fit in sidebands regions around the invariant mass of the Z boson. This fit function was found to provide a numerically stable description of the background with a good fit quality. Four different sets of sideband regions are employed: [70, 80] GeV and [100, 110] GeV; [60, 80] GeV and [100, 120] GeV; [50, 80] GeV and [100, 130] GeV; [55, 70] GeV and [110, 125] GeV. Signal contributions in these sidebands are subtracted using estimates from MC simulation [12, 47].

[10] Defined as a track that has at least 7 precision hits in one of the silicon trackers and at least one pixel hit.

[11] Defined as a cluster that is not affected by the presence of a dead front-end board in the first or second sampling, or by the presence of a dead HV region affecting the three layers of EM calorimeter, or by the presence of a masked cell in the core.

JHEP05(2024)162

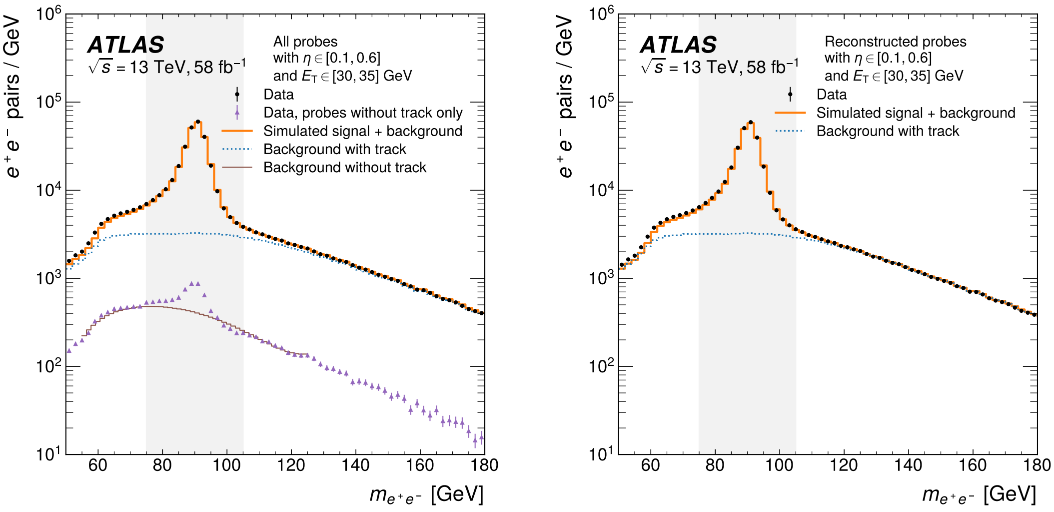

(a) (b)

Figure 1. Example of the $m_{e^+e^-}$ distribution used to determine the electron reconstruction efficiency, using 2018 data and probes with $E_T \in [30, 35]$ GeV and $|\eta| \in [0.1, 0.6]$. The shaded band indicates the nominal mass range used for efficiency extraction. The Monte-Carlo-simulated signal added to the total background is shown for illustration purposes; it is not used in the determination of the data efficiencies. (a) Including all probe clusters, whether reconstructed as an electron or not. The background with a track is shown separately. Also shown is the data component without track, as is an example background without track determined by fitting a polynomial to it in the sidebands [55, 70] GeV and [110, 125] GeV. (b) Including all reconstructed probes. Since these all have a track, there is only one background component.

The signal yields are extracted by counting the background-subtracted data events in a window around the Z-boson mass. The efficiency is calculated directly from the background-subtracted data yields. As systematic variations, the ranges [70, 110] GeV, [75, 105] GeV and [80, 100] GeV are used. Varying the selection of the tag as well as of the background template selections and the definition of the sideband regions and mass windows, yields in total 72 systematic variations of the measurement. The efficiency is taken to be the mean value of these whilst the root mean square of them is taken as systematic uncertainty. Example $m_{e^+e^-}$ distributions are shown in figure 1.

The electron reconstruction efficiency is very high with values between 98-99%; however, it drops at higher $|\eta|$ and in the calorimeter transition region. Electron reconstruction efficiencies corresponding to the kinematics of simulated $Z \to e^+e^-$ events are shown in figure 2 as a function of the electron transverse energy and pseudorapidity, respectively. The correction factors are shown in the middle panels of the figures. The systematic uncertainties on the correction factors are less than 0.5% over most of the kinematic range and less than 0.1% for $E_T > 30$ GeV. They are generally within 1% from unity. The correction factors for electrons with energies below $E_T < 15$ GeV are not accessible in data measurements. They are therefore taken to be 1 with uncertainties of 2% and 5% for electron within $|\eta| < 1.37$ and $|\eta| > 1.37$ respectively to conservatively cover the values and uncertainties of the correction factors measured at low E_T. The efficiencies measured as function of η are symmetric within uncertainties between the negative and positive ranges of electron pseudo-rapidity.

JHEP05(2024)162

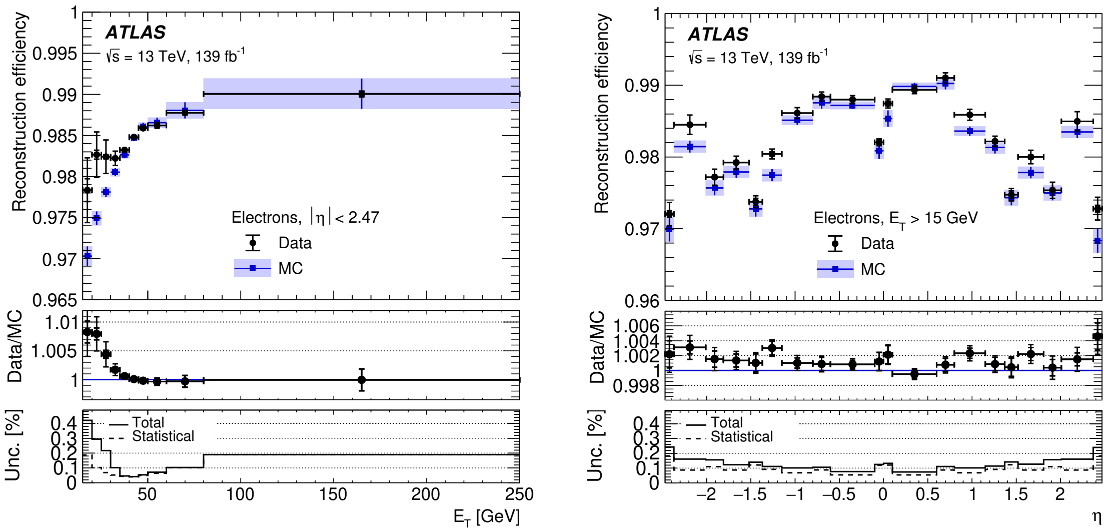

(a) (b)

Figure 2. Reconstruction efficiencies of electrons from $Z \to e^+e^-$ decays as a function of the electron E_T (a) and η (b) respectively. The top panels show the efficiencies obtained in data and simulation with their statistical and total uncertainties displayed as inner and outer error bars. The middle panels show their ratio which is applied as correction factor in analyses. The bottom panels show the relative statistical and total uncertainties on the data/MC ratio.

Figure 3 shows the reconstruction efficiencies for different years of data taking as a function of the number of primary vertices in the events, which is closely correlated with the number of additional *pp* interaction in an event. The efficiency generally rises as a function of pile-up. For example, there is a larger probability to match tracks with the clusters reconstructed from genuine electrons which otherwise might have only been reconstructed as clusters without tracks. The purity of the sample of reconstructed electrons also decreases with pile-up as further discussed in section 8. Generally, these effects are well-described in the MC simulation as evidenced by the flat data/MC ratio displayed in the middle panel of the figure. This indicates that correction factors have no strong dependence on the amount of pile-up.

7 Electron identification

Electron identification efficiencies are measured in 234 bins of electron E_T and η. The bin edges lie at $E_T = \{4.5, 7, 10, 15, 20, 25, 30, 35, 40, 45, 50, 60, 80, 150, \infty\}$ GeV and $\eta = \pm\{0, 0.1, 0.6, 0.8, 1.15, 1.37, 1.52, 1.81, 2.01, 2.37, 2.47\}$. To enhance statistics, some η bins are merged for $E_T < 20$ GeV and the absolute value of η is used for $E_T > 150$ GeV. For precision measurements, a finer granularity in η is available that has 52 bins instead of 20.[12]

For electrons with 4.5 GeV $< E_T <$ 20 GeV, identification efficiencies are measured in $J/\psi \to e^+e^-$ events. In the bin $p_T \in [15, 20]$ GeV, the correction factors from the J/ψ measurement are statistically combined with the ones from the Z measurements discussed

[12]The bin edges for this finer granularity lie at $\eta = \pm\{0, 0.1, 0.2, 0.3, 0.4, 0.5, 0.6, 0.7, 0.8, 0.9, 1, 1.1, 1.2, 1.3, 1.37, 1.52, 1.6, 1.65, 1.7, 1.8, 1.9, 2, 2.1, 2.2, 2.3, 2.4, 2.47\}$.

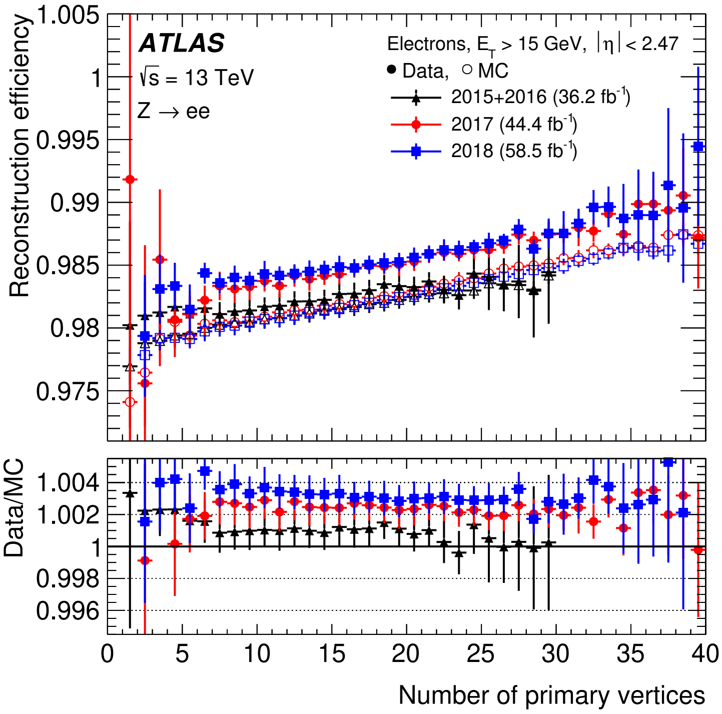

Figure 3. Reconstruction efficiencies of electrons from $Z \to e^+e^-$ decays as a function of number of primary vertices. The top panel shows the efficiencies obtained in data and simulation with their respective combined systematic and statistical uncertainties. The lower panel shows their ratios.

below. Events with $J/\psi \to e^+e^-$ decays are recorded with the triggers described in section 4 and are required to contain at least two oppositely charged electron candidates with $E_{\mathrm{T}} > 4.5$ GeV and $|\eta| < 2.47$. If more than two electrons pass the selection criteria, the pair with invariant mass closest to the J/ψ mass is considered. The tag electron must pass Tight identification, and it is required to be outside the calorimeter transition region, $1.37 < |\eta| < 1.52$. Both the tag and the probe electrons must be matched within $\Delta R < 0.07$ to the trigger objects that prompted the recording of the event. The trigger efficiency for electromagnetic clusters is high and was found not to bias the properties of the probe electron. Unlike previously, no isolation requirements are applied to the electrons in the nominal case. To suppress background from photon conversions and hadronic jets, the tag and the probe candidates must be separated from each other by $\Delta R > 0.15$.

For electrons with $E_{\mathrm{T}} > 15$ GeV, identification efficiencies are measured using $Z \to e^+e^-$ events. Events are recorded using the single-electron triggers and must contain two electron candidates with $|\eta| < 2.47$ and opposite charge. The tag electron must have $E_{\mathrm{T}} > 27$ GeV, and lie outside the calorimeter transition region $1.37 < |\eta| < 1.52$. It must pass the Tight identification and a track isolation requirement of $p_{\mathrm{T}}^{\mathrm{cone20}}/p_{\mathrm{T}} < 0.1$. It must be associated with the object that fired the trigger. The efficiency is extracted by counting the background-subtracted data yields in the range $m_{e^+e^-} \in [75, 105]$ GeV.

The background due to objects other than prompt electrons, e.g. light- and heavy-flavour hadrons or photon-conversions and Dalitz decays, cannot be simulated reliably using MC

JHEP05(2024)162

simulation. It is therefore determined from data. In $Z \to e^+e^-$ events, two methods are used to measure the background and their results are statistically combined. The first method, called Z mass, uses the electron-positron invariant mass, $m_{e^+e^-}$, as the discriminating variable between signal and background. The second, called Z isolation, uses the amount of energy in an isolation cone around the probe electron. Both methods are described in refs. [12–14] and here the improvements from the previous results are discussed.

7.1 $J/\psi \to e^+e^-$ measurement

Similarly to the methodology in refs. [12–14], the invariant-mass distribution of the two J/ψ electron candidates in the range [1.8, 4.6] GeV is fitted with functions to extract three contributions: J/ψ events, $\psi(2S)$ events, and the background from hadronic jets, heavy flavour decays, and electrons from conversions. The J/ψ and $\psi(2S)$ contributions are each modelled with a Crystal Ball function convoluted with a Gaussian function. The background is determined by fitting a third-order Chebyshev polynomial that was chosen for its numerical stability. In addition, where possible, combinatorial backgrounds from two random electron candidates that fall into the mass window are also considered. This is achieved by defining a same-charge region where the tag and the probe electron have the same charge and otherwise pass the normal criteria. If this region contains a sufficiently large number of events, which is on average more than 25 events per bin, then another component is added to the signal-region fit: a fifth-order Chebyshev polynomial that is fitted simultaneously in the same-charge and signal region. This treatment allows a better modelling of the background by adding an additional constraint on the combinatorial background. It is based on the assumption that the shape of the mass distribution is similar for the same charge and the opposite charge sign regions, but is only possible if there is sufficient statistics. This improved the agreement of the fit model with the data with respect to the previous publication.

$J/\psi \to e^+e^-$ events come from a mixture of prompt and non-prompt J/ψ production, with relative fractions depending both on the triggers used to collect the data and on the E_{T} of the probe electrons. Non-prompt J/ψ production can occur e.g. in b-hadron decays. Only the prompt J/ψ production yields prompt electrons, which are expected to behave similarly as those electrons from physics processes of interest to analyses. The non-prompt J/ψ production is therefore considered to be a source of background. To suppress this background, the pseudo-proper lifetime[13] t_0 of the reconstructed J/ψ is required to be -1 ps $< t_0 < 0.2$ ps. The residual non-prompt fraction in bins of probe electron E_{T} and η is calculated by using MC simulation and the ATLAS measurement using $J/\psi \to \mu^+\mu^-$ [51] of the non-prompt fraction in bins of J/ψ p_{T} and η. It is subtracted from the fitted J/ψ signal. The use of the more recent measurement [51] compared to the previous methodology [52] gives an improved estimate of the non-prompt fraction that has an uncertainty that is up to a factor of five smaller than previously.

[13]The pseudo-proper lifetime is defined as $t_0 = L_{xy} \cdot m_{\mathrm{PDG}}^{J/\psi}/p_{\mathrm{T}}^{J/\psi}$, where L_{xy} is the displacement of the J/ψ vertex from the primary vertex projected onto the flight direction of the J/ψ in the transverse plane, $m_{\mathrm{PDG}}^{J/\psi}$ is the nominal J/ψ mass [50] and $p_{\mathrm{T}}^{J/\psi}$ is the J/ψ-reconstructed transverse momentum. The ratio $m_{\mathrm{PDG}}^{J/\psi}/p_{\mathrm{T}}^{J/\psi}$ is the transverse component of the inverse of the relativistic factors, $\frac{1}{\beta\gamma}$.

JHEP05(2024)162

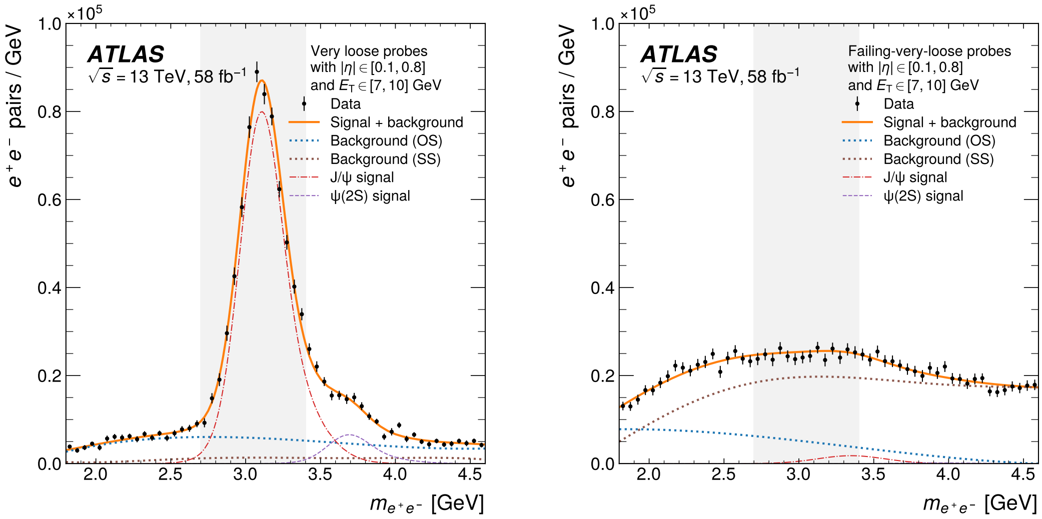

(a) (b)

Figure 4. Examples of nominal signal and background fits to the $m_{e^+e^-}$ distribution used to determine the efficiency denominator in the $J/\psi \to e^+e^-$ measurement, using 2018 data and probes with $E_{\mathrm{T}} \in [7, 10]$ GeV and $|\eta| \in [0.1, 0.8]$. The shaded band indicates the nominal mass range used for efficiency extraction. (a) Including all reconstructed probes that pass the very loose likelihood identification. The J/ψ meson peak around 3.1 GeV is clearly visible. (b) Including all reconstructed probes that fail the very loose likelihood identification. There is only a small signal component in a large background. Due to poor momentum modelling and combinatorial effects, the observed J/ψ meson peak is shifted to about 3.3 GeV. The $\psi(2S)$ component is so small that it is barely visible in the figure.

After background subtraction, the efficiency is extracted in the range $m_{e^+e^-} \in [2.7, 3.4]$ GeV. To improve the modelling of signal and background in the selection that enters the denominator of the efficiency, the selection of these probes is split into two orthogonal selections: into probes that fail or pass a very loose likelihood identification which is looser than the usual loose criterion. Hence, those probes that fail it only contribute to the denominator of the efficiency. An example of the $m_{e^+e^-}$ distribution for each of these selections, along with the various fitted signal and background contributions, is shown in figure 4. Example $m_{e^+e^-}$ distributions with probes passing the various likelihood identification working points are shown in figure 5.

The following variations are performed to establish systematic uncertainties of the low-p_{T} efficiency measurement:

- Changing the mass window for efficiency extraction to $m_{e^+e^-} \in [2.8, 3.3]$ GeV.
- Raising the upper limit of the pseudo-proper lifetime to $t_0 < 0.4$ ps.
- Adding an isolation criterion on the probe: $p_{\mathrm{T}}^{\mathrm{cone20}}/p_{\mathrm{T}} < 0.02$, $p_{\mathrm{T}}^{\mathrm{cone20}}/p_{\mathrm{T}} < 0.15$, or $E_{\mathrm{T}}^{\mathrm{cone20}} < 0.2$. This helps to vary the amount of non-prompt J/ψ background without impacting the efficiency of the prompt J/ψ sample significantly as tested on simulation. Applying the isolation to the probe gives a larger variation than applying it on the tag.
- Adding an isolation criterion on both the tag and the probe: $p_{\mathrm{T}}^{\mathrm{cone20}}/p_{\mathrm{T}} < 0.15$.
- Changing the Chebyshev polynomial for opposite-charge background to second order.

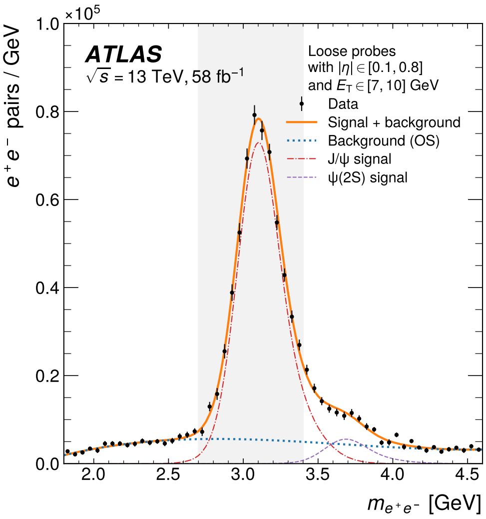

(a)

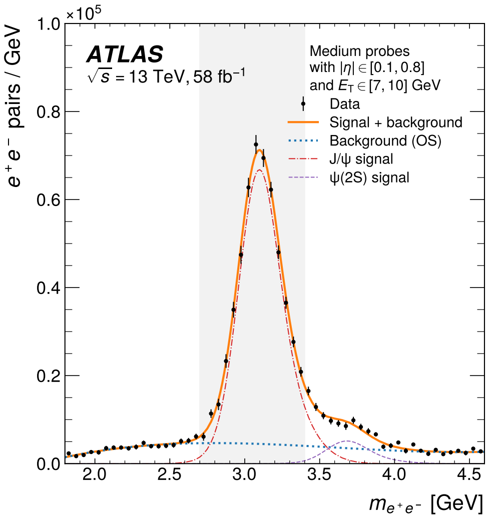

(b)

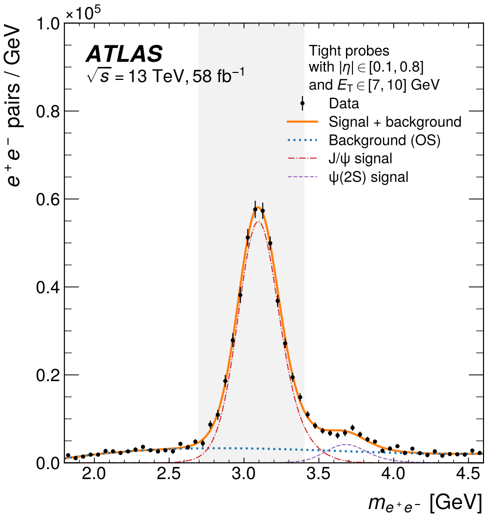

(c)

Figure 5. Examples of nominal signal and background fits to the $m_{e^+e^-}$ distribution used to determine the efficiency numerators in the $J/\psi \to e^+e^-$ measurement, using 2018 data and probes with $E_\mathrm{T} \in [7, 10]$ GeV and $|\eta| \in [0.1, 0.8]$. The shaded band indicates the nominal mass range used for efficiency extraction. The probes passing Loose, Medium, Tight identification are included in (a), (b), (c), respectively, yielding the amount of signal in the numerator of the corresponding efficiency. For electrons candidates passing identification criteria, there is often not enough events to determine the combinatorial background using the same charge region.

JHEP05(2024)162

Unlike for the methods using $Z \to e^+e^-$ events, the systematic variations are not combined by type. Instead, all variations for which the signal-region fit had a goodness of fit of χ^2 per number of degrees of freedom of less than 4 are included and their root mean square distance from the nominal is taken to be the uncertainty. The reason for this different treatment is that the J/ψ region suffers from much larger statistical fluctuations as well as modelling issues and individual systematic variations can yield a quite different efficiency value. Therefore this treatment can be understood as a regularisation procedure that reduces the effect of outliers. Less than 5% of the systematic variations across all measurements are discarded due to this requirement.

7.2 *Z*-mass method

The Z-mass method uses reference $m_{e^+e^-}$ distributions for signal and background, referred to as templates, obtained respectively in $Z \to e^+e^-$ MC simulation and using control regions in data. Previously, the background under the Z-boson peak was estimated by normalising a background template in sidebands of the $m_{e^+e^-}$ distribution. A long-standing limitation of this method was a tension between normalising the background in the low-mass compared to the high-mass sideband, which was reflected in a large systematic uncertainty. The reason for this tension was found to be the considerably different levels of signal contamination in the low- and high-mass sidebands and a non-optimal method to describe and normalize this signal contamination when creating the background template, biasing its shape. A new iterative procedure was devised to reliably subtract the background and to reduce dependence on the MC predictions. This yields a significantly more reliable efficiency measurement. The following steps are performed as part of the Z-mass method:

- The background templates are defined using a background control region where the probe electron is required to fail a relaxed version of the Loose likelihood identification and to have a minimum amount of energy deposited close-by, $E_{\mathrm{T}}^{\mathrm{cone30}}/p_{\mathrm{T}} > 0.1$.

- These background templates still contain signal contamination, which is subtracted in a step called *template cleaning*. The template cleaning consists of fitting the background template using a suitable polynomial for the background and a template for $Z \to e^+e^-$ contamination obtained from MC simulation to extract the relative contributions of the background and the contamination of the signal to the background template. The scaled signal contamination is then subtracted to create a pure background template.

- The pure background template and the MC signal template are fitted to the data in the signal region to extract the background normalization. Post-fit, the scaled background template is then subtracted from the data. As a result of residual miscalibrations and inaccuracies of the MC description of the Z line shape, a discrepancy between the data and the MC simulation of a few percent can be observed.

- Therefore weighting factors are extracted to describe the signal invariant mass distribution better in data. These weighting factors are obtained only for probes passing the Tight identification and are calculated as the ratio of the background-subtracted data to the signal MC prediction in bins of $m_{e^+e^-}$. The Tight probes only have small background and therefore give a pure, unbiased signal shape with the greatest confidence.

- The weighting factors are applied to all signal $m_{e^+e^-}$ distributions taken from the MC simulation, independent of the requirements applied to the probe electrons, and for both the background control region and the signal region.

- This procedure is iterated once more, starting from the *template cleaning*, the first step in the procedure.

The systematic uncertainties of the Z-mass method are estimated by varying choices in the method and taking the resulting efficiencies as systematic variations of the nominal one. The variations are:

- The background control region is varied by changing the very loose likelihood identification the candidate probes need to fail or alternatively the isolation requirement is varied to $E_{\mathrm{T}}^{\mathrm{cone40}}/p_{\mathrm{T}} > 0.07$.

- The signal region fit is repeated using only $m_{e^+e^-}$ ranges below or above the Z-boson peak, respectively.

- In all fits, the fit uncertainty is applied to the normalisations of the templates as a systematic variations.

- The tag electron isolation is tightened by adding the requirement $E_{\mathrm{T}}^{\mathrm{cone40}} < 5$ GeV.

- The efficiency is extracted by counting the background-subtracted data yields in the $m_{e^+e^-}$ ranges $[70, 110]$ GeV and $[80, 100]$ GeV.

The systematic uncertainties evaluated as described above are summed in quadrature.

Examples of $m_{e^+e^-}$ distributions used as the sensitive variable to establish the amounts of signal and background in the Z-mass method are shown in figure 6 for the case including all reconstructed probes (as in the identification efficiency denominator) and including probes passing the different identification working points (as in the numerator of the corresponding efficiency). For simplicity, the figures include probes over the full used pseudorapidity range $|\eta| < 2.47$, whereas the actual measurement is done in bins of η.

7.3 *Z*-isolation method

The Z-isolation method relies on the amount of transverse energy in an isolation cone of radius $\Delta R = \mathrm{XX}/100$ around the probe electron, $E_{\mathrm{T}}^{\mathrm{coneXX}}$, to distinguish between signal and background. Background templates are defined in data in a background-enriched region where the charges of the tag and probe candidate are required to have the same sign and the probes must fail cuts on various identification variables. The requirements are designed to be as uncorrelated with $E_{\mathrm{T}}^{\mathrm{coneXX}}$ as possible so as to avoid bias. The signal contamination is subtracted from the background templates using MC simulation.

JHEP05(2024)162

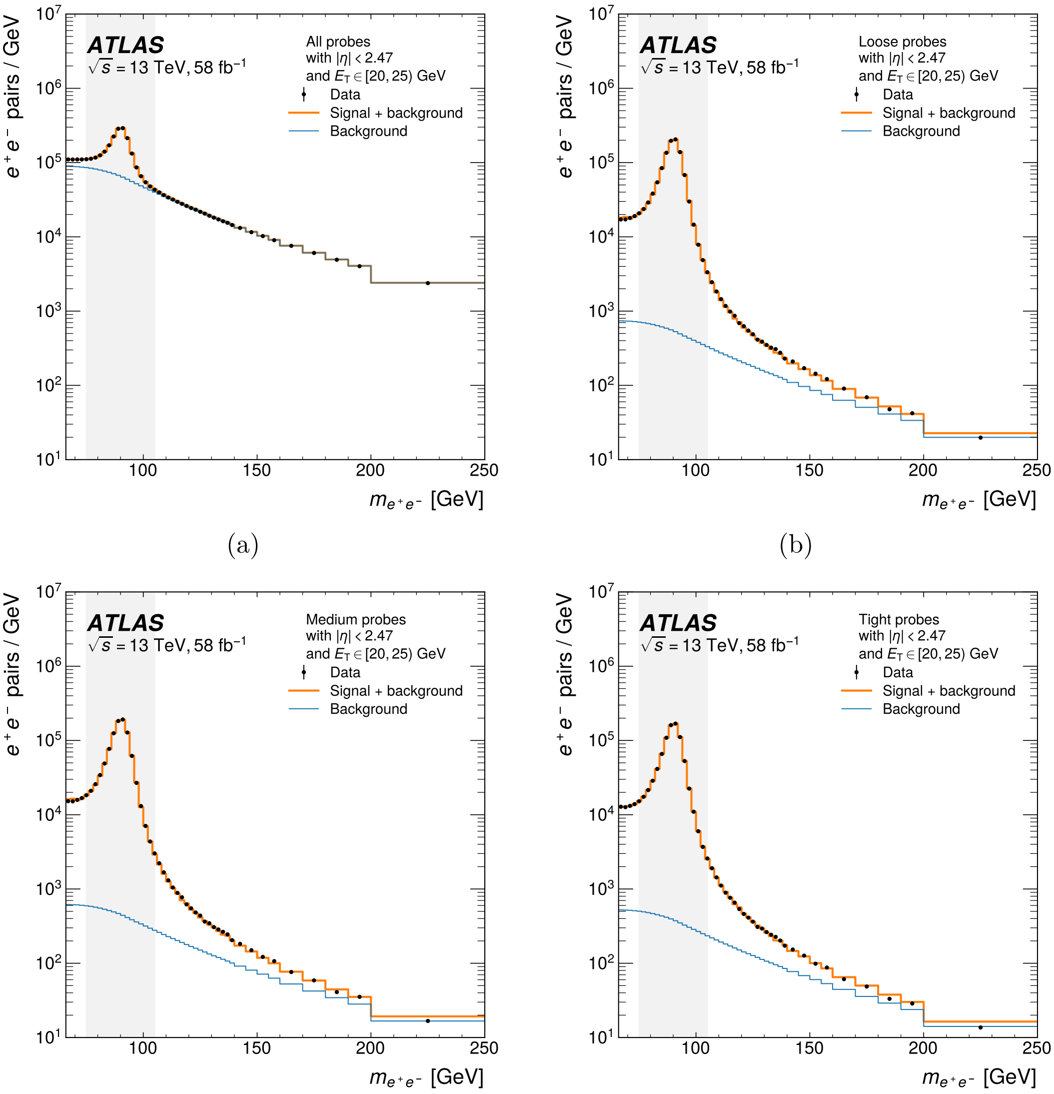

Figure 6. Examples of nominal signal and background template fits to the $m_{e^+e^-}$ distribution in the Z-mass method, using probes with $E_T \in [20, 25]$ GeV. The Z-boson peak around 91 GeV is clearly visible. The shaded band indicates the nominal mass range used for efficiency extraction. (a) Including all the reconstructed probes, yielding the amount of signal in the denominator of the efficiency. Including probes passing the (b) Loose, (c) Medium, (d) Tight identification, respectively, yielding the amount of signal in the numerator of the corresponding efficiency.

JHEP05(2024)162

The exact selection of the background templates, one nominal and one systematic variation, is done using the MC-simulated QCD sample by choosing template definitions in each E_{T}-η bin that minimise the bias defined as

$$\text{bias} = \left| \frac{N^{\text{template}}(E_{\mathrm{T}}^{\text{cone30}} < 7.5\ \text{GeV})}{N^{\text{template}}(E_{\mathrm{T}}^{\text{cone30}} > 7.5\ \text{GeV})} \frac{N^{\text{all}}(E_{\mathrm{T}}^{\text{cone30}} > 7.5\ \text{GeV})}{N^{\text{all}}(E_{\mathrm{T}}^{\text{cone30}} < 7.5\ \text{GeV})} - 1 \right|, \tag{7.1}$$

where $N(*)$ signifies a yield of MC-simulated background probes in the tag-and-probe region with requirement $*$ applied to the probe, and the superscripts "all" and "template" indicate that either all MC-simulated background probes are used, or only those passing the template selection, respectively. The bias variable quantifies how well the background template reproduces the true (MC-simulated) ratio of the background in the $E_{\mathrm{T}}^{\text{cone30}}$ high tails and at low $E_{\mathrm{T}}^{\text{cone30}}$.

In most E_{T}-η bins, the chosen templates contain less than 5% signal contamination. However, for $|\eta| > 1.81$, $E_{\mathrm{T}} > 25$ GeV this increases to about 25%. There are two different template definitions that are used depending mostly on the probe electron E_{T}.

The efficiency is extracted by considering the yields in the Z-boson peak region with probe isolation $E_{\mathrm{T}}^{\text{cone30}} < 12.5$ GeV. The background is estimated by normalising the background template in the region $E_{\mathrm{T}}^{\text{cone30}} > 12.5$ GeV, where the signal contamination has been subtracted using MC simulation.

Figure 7 shows examples of the distribution of the probe isolation variable $E_{\mathrm{T}}^{\text{cone30}}$ in data along with the signal and background predictions. It can be seen that signal electrons are more isolated than the background and that the two contributions together describe the observed isolation distributions reasonably well, when considering that there are some modelling problems in the MC simulation.

The following variations are performed to estimate systematic uncertainties of the Z-isolation method:

- Using an alternative background template chosen based on the bias defined in eq. (7.1). It is the same for the whole kinematic phase space and effectively is the second-least biased template found.
- Scaling the normalisation of signal contamination subtracted from the background (both the template and the tail region where it is normalised) by an estimated ±30% to conservatively account for modelling uncertainties.
- Using $E_{\mathrm{T}}^{\text{cone40}}$ to define the background normalisation and signal regions (instead of $E_{\mathrm{T}}^{\text{cone30}}$).
- Varying the $E_{\mathrm{T}}^{\text{cone30}}$ boundary defining the background normalisation and signal regions to 10 GeV and 15 GeV.
- An additional tag electron isolation $E_{\mathrm{T}}^{\text{cone30}} < 7.5$ GeV is applied.
- The efficiency is extracted by counting the background-subtracted data yields in the $m_{e^+e^-}$ ranges $[70, 110]$ GeV and $[80, 100]$ GeV.

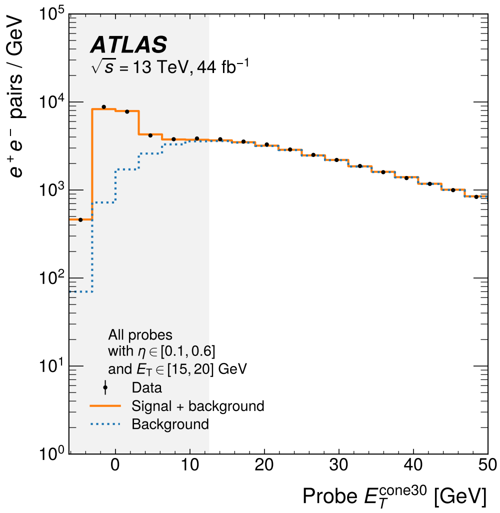

(a)

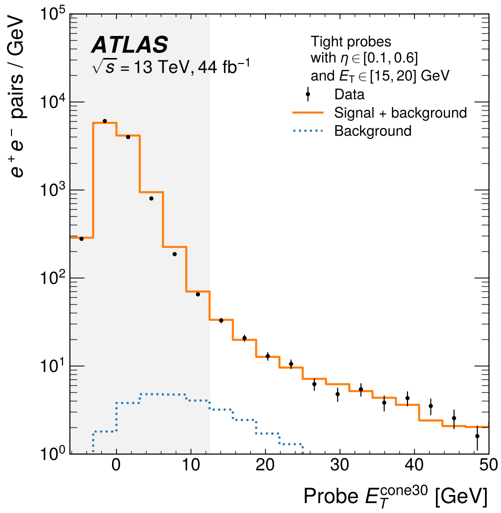

(b)

Figure 7. Examples of the probe $E_{\mathrm{T}}^{\mathrm{cone30}}$ isolation variable distribution with the corresponding signal and background, using probes with $\eta \in [0.1, 0.6]$ and $E_{\mathrm{T}} \in [15, 20]$ GeV. The nominal mass requirement $m_{e^+e^-} \in [75, 105]$ GeV is already applied. The background template is normalised in the tail $E_{\mathrm{T}}^{\mathrm{cone30}} > 12.5$ GeV. The shaded area, $E_{\mathrm{T}}^{\mathrm{cone30}} < 12.5$ GeV, shows the nominal region used for efficiency extraction. (a) Including all the reconstructed probes, yielding the amount of signal in the denominator of the efficiency. (b) Including probes passing Tight identification, yielding the amount of signal in the numerator of the corresponding efficiency.

The systematic variations are combined in the same way as in the Z-mass method, i.e., each of them is interpreted as one symmetric systematic uncertainty. In the case where the systematic uncertainty is evaluated by varying a parameter up and down, the uncertainty is symmetrised and the largest variation is used as a systematic source.

7.4 Combination

To calculate the final results for the identification efficiency, the correction factors obtained with the Z methods are combined by averaging them weighted by their uncertainties in each E_{T}-η bin independently but taking into account their correlations following the procedure in ref. [53]. During the combination, those uncertainties that stem from the modelling of the backgrounds are treated as uncorrelated since they are specific to each of the two Z methods. However, the uncertainty related to the signal definition, estimated by varying the $m_{e^+e^-}$ window and the uncertainty from varying the amount of background by tightening the isolation requirements on the tag electron are treated as fully correlated. In addition, statistical uncertainties are treated as fully correlated for the signal events between the two methods whilst background events are considered to be uncorrelated. The improvements to the Z-mass and Z-isolation methods have both shrunk the systematic uncertainties in each method and significantly improved the agreement between the two methods, which was previously driving their combined uncertainty. Whilst there were differences of up to 2% between the methods, this has now been reduced to less than 0.5% on average.

In a final step, the Z correction factors are combined with those obtained using the J/ψ resonance in the overlapping E_{T} range, $[15, 20]$ GeV. This combination uses a χ^2 minimization with a profiling of the systematic uncertainties following the method reported in ref. [54]. Thanks to the reported improvements, the uncertainties on the combined corrections factors have been halved compared with previous measurements [14].

7.5 Results

The measured identification efficiencies for the various working points are shown in figure 8(a) as a function of E_{T} and in figure 8(b) as a function of η. In each case, the respective other variable is integrated over. The ratio of efficiencies in data and MC simulation is close to unity, typically within 5%. Except for $p_{\mathrm{T}} < 15$ GeV, the efficiencies are slightly lower in data than in simulation. Looser identification criteria show a better agreement between data and MC simulation. The efficiencies generally decrease for lower transverse momenta.[14] The efficiencies measured as function of pseudo-rapidity are found to be mostly symmetric between the negative and positive ranges of η, especially when considering uncertainties.

In figure 9, the individual measurement methods in their respective range of applicability and the combination are shown. The Medium identification efficiencies are shown for electrons in simulated $Z \to e^+e^-$ events with the corrections factors applied such that they reflect the data efficiencies. They give a general idea of the performance in various kinematic domains that are of interest in ATLAS analysis even if they are based on the $Z \to e^+e^-$ topology and do not necessarily reflect the efficiencies of other processes. The comparison of the relative uncertainties of the individual methods to the results of the combination illustrate the impressive improvements in the energy range above 15 GeV where the systematic uncertainties dominate over the statistical uncertainties.

Figure 10 shows comparisons of the new combined Tight identification efficiencies to the previous ATLAS measurement using data from the years 2015–2017 [14]. The new measurement is in good agreement with the previous one. When evaluated by integrating over the electron kinematics in simulated $Z \to e^+e^-$ events, the efficiency uncertainty has decreased by almost one third for the Loose working point and by more than half for the Medium and Tight working points. The uncertainty decrease is quite independent of η, small for low p_{T} (< 15 GeV) and high p_{T} (> 80 GeV), and large for the p_{T} range between these extremes.

Figure 11 depicts the uncertainties on the data-to-MC correction factor for the Medium identification efficiencies as a function of the transverse energy of the electron for the main pp run periods at the LHC, namely Run 1 data taking at collision energies of $\sqrt{s} = 7$ TeV (2011) and $\sqrt{s} = 8$ TeV (2012) as well as Run 2 data taking at $\sqrt{s} = 13$ TeV (2015–2018). The experiment has been able to tune the definition of the Medium identification to reach target efficiencies of about 80 % for each of the data-taking periods despite the significant increase in pile-up for the 13 TeV data. Despite the increased backgrounds, the uncertainties on the data/MC correction factors have been reduced for most of the energy range except for $E_{\mathrm{T}} < 40$ GeV, where the low pile-up environment of the 2011 data-taking period had allowed

[14] For the Loose identification criterion, an updated version of the likelihood was created using more appropriate shower-shapes in the tuning process that has a better efficiency specifically in the p_{T} range of 15–20 GeV, and it is used for $H \to 4\ell$ analyses [55], but is not shown here.

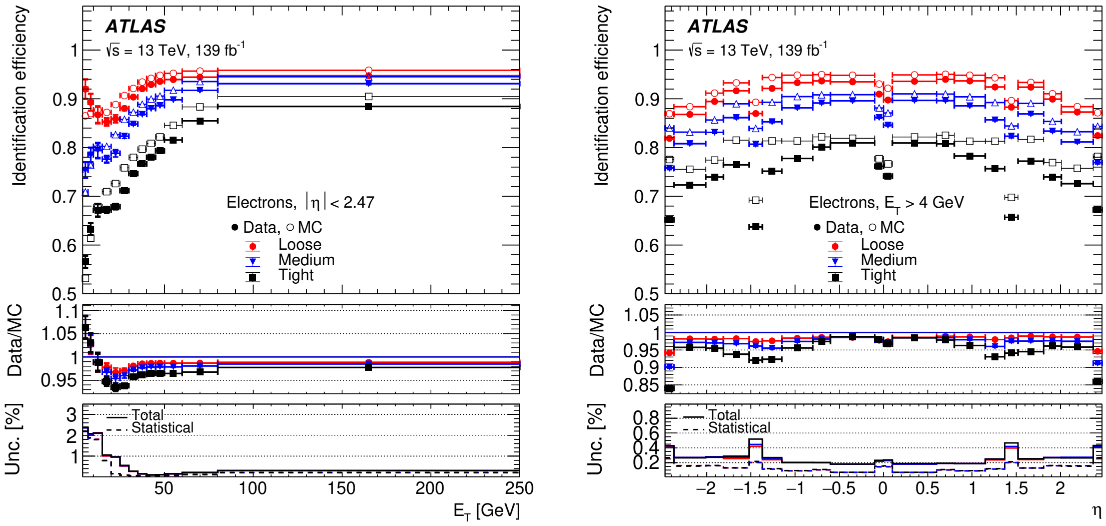

(a) (b)

Figure 8. Identification efficiencies of electrons from $Z \to e^+e^-$ decays as a function of the electron's (a) transverse momentum and (b) pseudorapidity for the different identification working points. The top panels show the efficiencies obtained in data and simulation with their statistical and total uncertainties displayed as inner and outer error bars. The middle panels show their ratio that is applied as correction factor in analyses. The bottom panels show the relative statistical and total uncertainties in the data/MC ratio.

to employ the W-boson resonance for efficiency determination in addition to the methods used in 2015–2018 [56]. The comparison is made between the respective correction factors used in high precision analyses, which are applicable only down to transverse energies of 20 GeV.

8 Background rejection

Section 6 and 7 introduced the measurement of the prompt electron efficiencies and the MC to data correction factors. Of equal interest is the knowledge of the background rejection and of how well the rejection is modelled in the MC simulation. Whilst this is not immediately applicable in physics analyses, it is important for their design. The signature of a cluster with a matched track can be caused by a variety of particles other than electrons, and the fact that electrons and jets are reconstructed independently of each other causes prompt electron candidates to be reconstructed as jets and vice versa. The knowledge of the general rates of jet production combined with rejection rates can therefore give indications of expected backgrounds. In the following, rejection rates of the reconstruction are studied in data by determining how many jets are also reconstructed as electrons. Rejection rates of the identification with respect to the reconstruction can only be studied using MC simulation because of the large rejection rates leading to large amounts of prompt electrons in any data samples.

JHEP05(2024)162

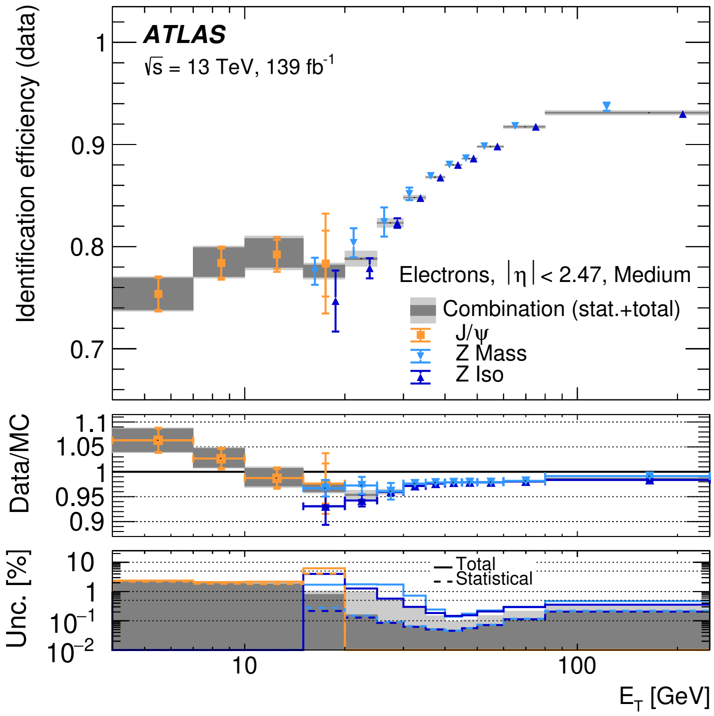

Figure 9. Data electron identification efficiencies using the J/ψ and Z resonance are shown as a function of the electron's transverse energy. They are obtained by applying correction factors to the electrons from $Z \to e^+e^-$ events before the integration over η and therefore reflect the underlying kinematics of $Z \to e^+e^-$ events. The Medium identification working point is shown for the breakdown of individual measurements that enter the combination as well as the results of the combination. The middle panel contains the ratio of the measured to the MC-simulated efficiencies. The bottom panel gives the relative uncertainties with the horizontal dotted lines indicating uncertainties of 0.1, 0.5, 1, 5 and 10%.

8.1 Measurement of the background rejection of the electron reconstruction in data

The background rejection of the electron reconstruction is measured using the production of Z bosons in association with jets. Jets are reconstructed using the anti-k_t algorithm with a radius parameter of $R = 0.4$ and topological clusters as input [20, 48]. Jets originating from pile-up are rejected using an algorithm based on the fraction of tracks originating from the primary vertex [57] or outside the ID coverage based on missing transverse momentum [58]. Jets are calibrated as reported in ref. [59]. Events are selected requiring at least two oppositely charged electrons passing the medium identification criteria and isolated from hadronic activity measured using tracks, $p_{\mathrm{T}}^{\mathrm{cone20}}/p_{\mathrm{T}} < 0.15$. The invariant mass of the dielectron system is required to lie between 81.18 GeV $< m_{e^+e^-} <$ 101.18 GeV and the pair closest to the Z-boson mass is taken to consist of prompt electrons, whilst all other reconstructed electron candidates in the event are assumed to be backgrounds misreconstructed as electron candidates. These electron candidates are required to be reconstructed and satisfy the general quality requirements described in section 6. Jets closer than $\Delta R = 0.4$ to the electrons

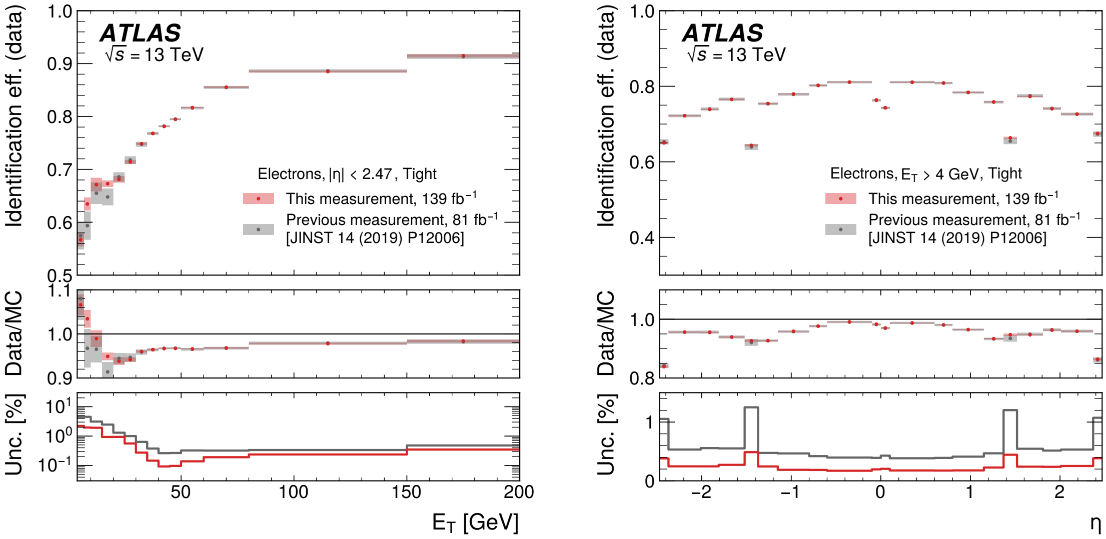

(a) (b)

Figure 10. Comparison of the new combined Tight identification efficiencies to the previous ATLAS measurement using data from the years 2015–2017 [14] as a function of the electron's (a) transverse energy and (b) pseudorapidity. The middle panels contain the ratio of the measured to the MC-simulated efficiencies. The bottom panels give the relative uncertainty of the combination of measurements.

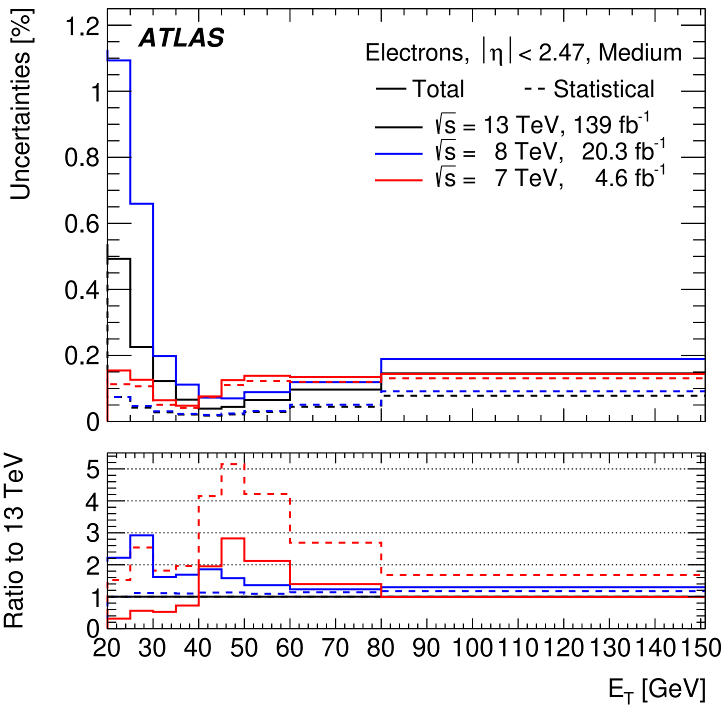

Figure 11. Uncertainties on the data-to-MC correction factors shown for the underlying kinematics of $Z \to e^+e^-$ events at 13 TeV, as a function of the electron's transverse energy. The Medium identification working point is shown and compared for the main pp data-taking periods at the LHC.

forming the pair closest to the Z mass are removed. Only those electrons reconstructed in the central region having $|\eta| < 2.47$ and $E_{\mathrm{T}} > 30$ GeV are considered for the rejection measurement. MC studies suggest that electroweak processes with a Z boson and additional prompt isolated electrons contribute less than 0.5% to the selected events and therefore no attempt was made to subtract prompt isolated electrons. For the study, only the 2017 pp data using 44 fb^{-1} with a mean number of interactions per bunch crossing of 37.8 is used. The pile-up in this data sample is slightly larger than in the other years of data taking, but given its relatively small contribution to background electrons of 5-10 %, can still be taken as representative of the other years.

The selected jets and the electron candidates have very different energy scales, as depicted in figure 12. Here the relative difference between jet and associated fake electron, normalised to the jet p_{T}, $\frac{p_{\mathrm{T}}^{\mathrm{jet}} - p_{\mathrm{T}}^{\mathrm{e}}}{p_{\mathrm{T}}^{\mathrm{jet}}}$, is shown for all fake electrons with a transverse energy above 4 GeV and for those with $E_{\mathrm{T}} > 18$ GeV. In most cases, an electron candidate reconstructed from a jet has only about 10% of the p_{T} of its jets. The large difference in the p_{T} distributions between jets and their associated reconstructed background electrons explains the breadth of the energy difference distribution. Figure 12(a) is dominated by very low E_{T} electrons as without further restrictions any jet with an electromagnetic energy component of more than 4 GeV is likely to be reconstructed as an electron. Once a suitable energy requirement of $E_{\mathrm{T}} > 18$ GeV is applied to suppress backgrounds (figure 12(b)), the peak of the distribution shifts to lower values of $\frac{p_{\mathrm{T}}^{\mathrm{jet}} - p_{\mathrm{T}}^{\mathrm{e}}}{p_{\mathrm{T}}^{\mathrm{jet}}}$, indicating that the reconstructed electrons on average have an E_{T} more similar to the jet p_{T}.

The efficiency to reconstruct an electron from a genuine jet is measured as $\frac{n_{\mathrm{electrons}}}{n_{\mathrm{all\ jets}}}$ where n_{electron} is the number of reconstructed electron candidates and $n_{\mathrm{all\ jets}}$ is the number of all jets. The rejection is measured as function of the p_{T} of its associated jet and is shown in figure 13 where again all fake electrons ($E_{\mathrm{T}} > 4$ GeV) and those with $E_{\mathrm{T}} > 18$ GeV are studied separately. In addition to the jet p_{T} an approximation of the electron E_{T} is given below the x-axis, calculated as $(1 - 0.88)$ and $(1 - 0.68)$ times the jet p_{T} using the most probable values in the distributions in figure 12. The reconstruction efficiency of background electron candidates with $E_{\mathrm{T}} > 4$ GeV rises very quickly and reaches about 60% to reconstruct a 12 GeV electron from a 100 GeV jet. For background electron candidates with $E_{\mathrm{T}} > 18$ GeV the efficiency ranges from 0.05×10^{-3} at a jet p_{T} of 30 GeV to 0.03 at a $p_{\mathrm{T}}^{\mathrm{jet}}$ of 50 GeV and steeply rises to almost 0.5 in data above 100 GeV for both jets and electrons.

There is some tension between the measured and predicted efficiencies for low-p_{T} electrons (figure 13(a)). However, when considering electrons with p_{T} above 18 GeV (figure 13(b)), the measured efficiencies agree within the systematic uncertainties of the jet calibration with the predictions from the MC simulation except at the highest energy scales where the prediction overshoots the data and the data efficiency drops slightly due to problems in the track-to-cluster matching in the dense environments of these highly boosted jets.

8.2 Expected background rejection of the electron identification requirements

The Loose, Medium and Tight identification requirements introduced in section 3.2 are designed to deliver fixed signal selection efficiencies for prompt electrons on top of the reconstruction. For prompt electrons, the background can be classified in three main categories,

JHEP05(2024)162

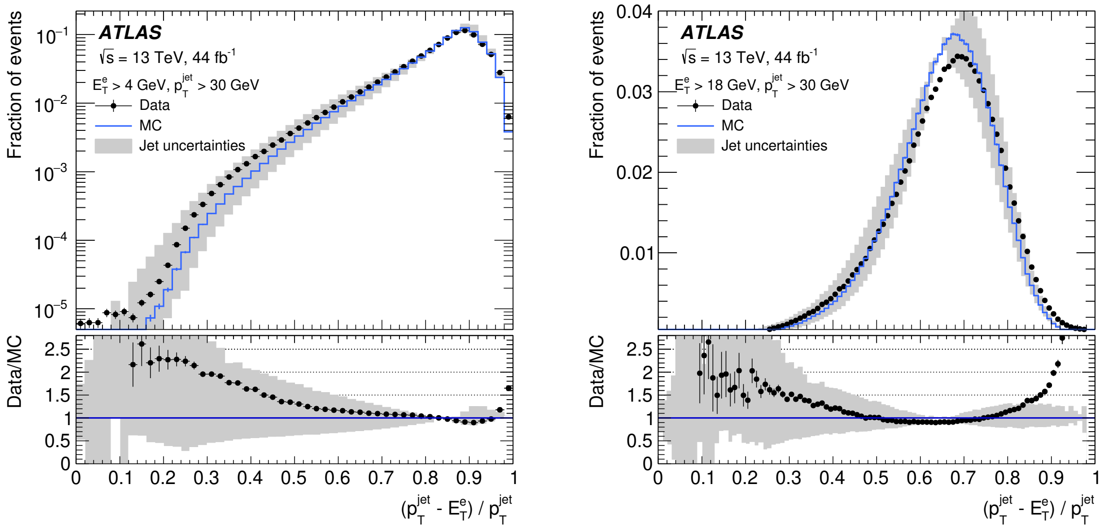

(a) (b)

Figure 12. The energies of the jet and its associated electron are compared using their p_{T} difference divided by the jet p_{T}, $\frac{p_{\mathrm{T}}^{\mathrm{jet}}-E_{\mathrm{T}}^{\mathrm{e}}}{p_{\mathrm{T}}^{\mathrm{jet}}}$. The data is shown as markers whereas the MC prediction is shown as a histogram. The grey area indicates the systematic uncertainties of the jet energy calibration. Only additional reconstructed electron candidates in Z-boson events are included. The electron pair forming the Z boson as well as their associated jets were removed if closer than $\Delta R < 0.4$. Jets are required to have $p_{\mathrm{T}}^{\mathrm{jet}} > 30$ GeV. (a) shows the comparison for all additional reconstructed electrons with $|\eta| < 2.47$ and $E_{\mathrm{T}}^{\mathrm{e}} > 4$ GeV, whilst (b) shows the same comparison for reconstructed electrons with $|\eta| < 2.47$ and $E_{\mathrm{T}}^{\mathrm{e}} > 18$ GeV.

namely non-isolated electrons from heavy-flavour (HF) decays, background electrons from photon conversions and Dalitz decays, and light-flavour hadrons (LF). Additionally, electrons coming from pile-up can be identified, comprised of both prompt and non-prompt electrons as well as hadrons. Using MC simulation collision samples of inclusive $2 \rightarrow 2$ QCD production, which includes top-quark pair and weak vector-boson production at leading order (in the following referred to as inclusive QCD production), filtered at particle level to mimic a first-level EM trigger requirement, these three background categories can be investigated. The distinction between the different sources of signal background is obtained using truth-level information from the MC simulation employing a matching of the reconstructed track hits to energy deposits left by truth-level particles on their way through the detector.

Figure 14 shows the fraction of the different categories to the total background as a function of E_{T}, $|\eta|$ and number of primary vertices. Only reconstructed electrons in the central region of the ATLAS detector ($|\eta| \leq 2.47$) with $E_{\mathrm{T}} > 17$ GeV are considered. The total background is dominated by the LF hadrons when considering reconstructed electrons. Electrons from photon conversions represent the second most abundant background, while HF decays constitute less than 1% of the total background and pile-up background contributes about 5 % on average but with a stronger dependence on the number of reconstructed primary vertices. The composition of the different sources across the E_{T} spectrum differs only slightly with less HF electron candidates at high E_{T}. Photon conversions increase with

JHEP05(2024)162

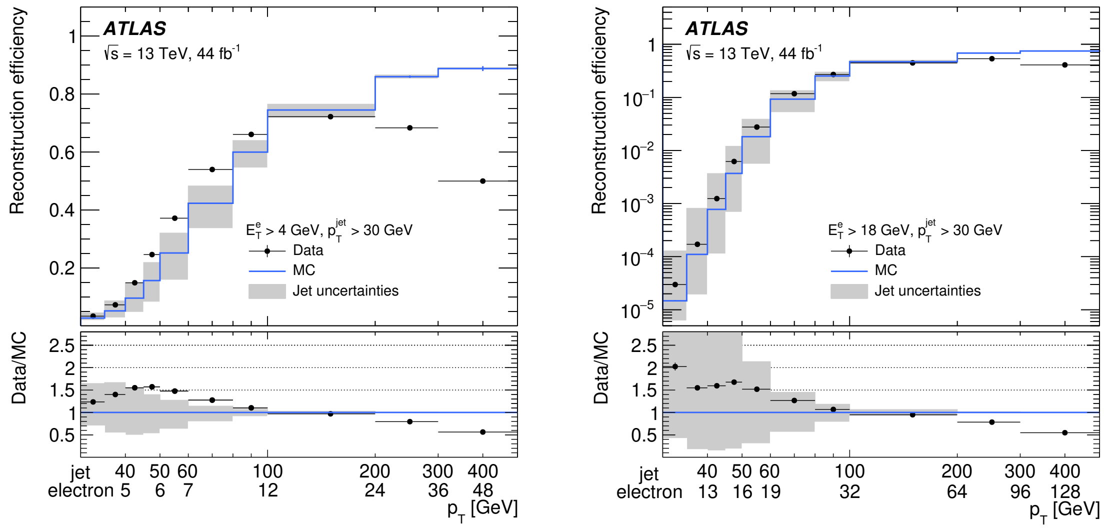

(a) (b)

Figure 13. The efficiencies to reconstruct an electron from a jet are shown as function of the jet transverse momentum. The data is shown as markers whereas the MC prediction is shown as a histogram. The grey area indicates the systematic uncertainties of the jet energy calibration. Only additional reconstructed electron candidates in Z-boson events are included. The electron pair forming the Z boson as well as their associated jets were removed if closer than $\Delta R < 0.4$. Jets are required to have $p_{\mathrm{T}}^{\mathrm{jet}} > 30$ GeV. (a) shows the efficiency for all reconstructed electrons with $|\eta| < 2.47$ and $E_{\mathrm{T}}^{\mathrm{e}} > 4$ GeV, whilst (b) shows the same comparison for reconstructed electrons with $|\eta| < 2.47$ and $E_{\mathrm{T}}^{\mathrm{e}} > 18$ GeV. Additionally, an approximate electron energy is shown on the horizontal axis that is obtained by scaling the jet transverse momentum according to the most probable value of the relative energy difference as shown in figure 12. Due to this approximation, in (b) efficiencies are shown also for bins with an approximate $E_{\mathrm{T}}^{\mathrm{e}} < 18$ GeV. These are populated by electrons carrying a larger than average fraction of the jet energy.

higher values of $|\eta|$ due to the increased material photons traverse and accordingly the higher probability for conversions. As the material distribution of the detector as implemented in the simulation is symmetric around $\eta = 0$, the fraction of photon conversions is perfectly symmetric for positive and negative pseudo-rapidity.

Table 1 details the background rejections in MC simulations for the different categories of backgrounds and their fractions as determined for inclusive QCD production. These numbers are not directly comparable with those published in ref. [12] as the reconstruction algorithms and the identification requirements have changed since the 2012 data taking at $\sqrt{s} = 8$ TeV. The rejections obtained in Run 2 are worse by a factor of about 1.5 due to the increased pile-up, which makes the calorimetric shower shapes more similar between signal and background, decreasing the achievable rejection at a fixed signal efficiency. The composition of the background is relatively even in Run 2 for the different identification requirements and background categories with about one third consisting of HF background, one half consisting of light flavour backgrounds and the rest made up from background electrons. However, the amount of heavy flavour, light flavour or electron backgrounds depends heavily on the production processes considered and is therefore reflective of the inclusive 2→2 QCD sample

JHEP05(2024)162

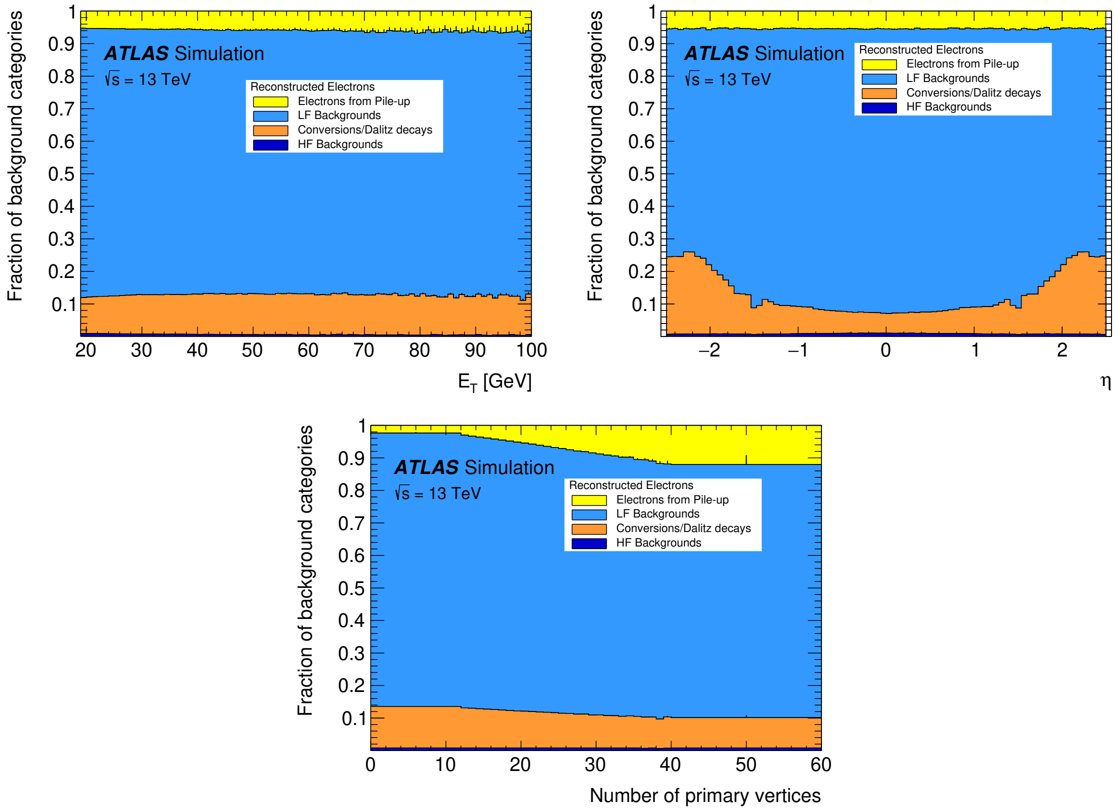

Figure 14. For the selected sample of reconstructed background electrons, the fraction of four background categories relative to the total background is shown as a function of E_{T}, $|\eta|$ and the number of primary vertices in a MC simulation sample of inclusive QCD production. Only statistical uncertainties are shown.

at the higher centre-of-mass energy. It will differ significantly for different event selections (e.g. requiring b-tagged jets in the event) and the predominant background processes involved.

The efficiencies to select a light flavour jet or a background electron as a prompt lepton using the Tight identification are less than 1% whereas about 20% of heavy flavour decays are identified as prompt leptons. The stark difference between heavy flavour and light flavour efficiencies motivates studies to target the different background categories using specific identification selections in future. Figure 15 shows the identification efficiency of signal electrons as determined in MC simulation versus the background rejection.

9 Electron isolation

9.1 Improved pile-up subtraction for the calorimeter isolation

As described in section 3.2, the calorimeter isolation is calculated from energy deposits in the calorimeter cells, $E_{\mathrm{T,raw}}^{\mathrm{isol}}$, and corrected by removing the energy of the electron or photon candidate and contributions from pile-up and underlying event. The explicit calculation for the calorimeter isolation reads as:

$$E_{\mathrm{T}}^{\mathrm{coneXX}} = E_{\mathrm{T,raw}}^{\mathrm{isolXX}} - E_{\mathrm{T,core}} - E_{\mathrm{T,leakage}}(E_{\mathrm{T}}, \eta, XX) - E_{\mathrm{T,pile\text{-}up}}(\eta, XX), \tag{9.1}$$

JHEP05(2024)162

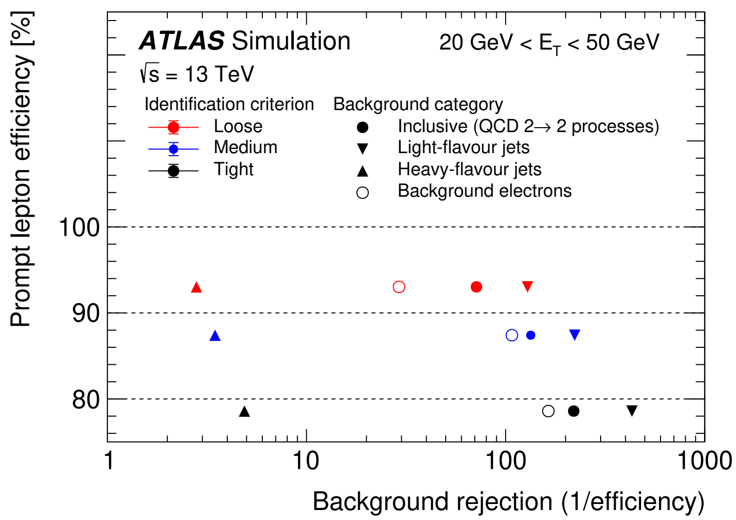

Figure 15. The identification efficiency of signal electrons as determined in MC simulation are shown as a function of the background rejection, defined as the ratio of the number of all reconstructed fake electrons to those passing identification criteria. All three identification criteria, Loose, Medium and Tight, are shown for each of the background electron categories as well as for inclusive QCD production.

$20\,\text{GeV} < E_\text{T} < 50\,\text{GeV}$								
Selection	MC efficiency [%] $Z \to e^+e^-$ signal	MC efficiency [%] Background	Background composition [%]			MC efficiency [%] for background categories		
			HF	bkg e	LF	HF	bkg e	LF
Loose	93.03 ± 0.01	1.401 ± 0.008	22.1	29.6	48.3	35.7 ± 0.5	3.43 ± 0.04	0.776 ± 0.007
Medium	87.41 ± 0.01	0.748 ± 0.006	32.3	15.0	52.6	28.8 ± 0.4	0.93 ± 0.02	0.450 ± 0.005
Tight	78.59 ± 0.01	0.455 ± 0.005	39.1	16.2	44.7	20.5 ± 0.4	0.61 ± 0.02	0.232 ± 0.004

Table 1. Background efficiency of different identification selections for inclusive QCD production. The electron candidates are required to have transverse energies between 20 GeV and 50 GeV and electrons from W- and Z-boson decays are removed at particle level. The composition of the sample is categorized according to MC simulation information: non-isolated electrons from heavy-flavour decays, background electrons from photon conversions and Dalitz decays, and light-flavour hadrons. The sample of reconstructed background electrons consists of 0.9% HF, 12.1% photon conversions and Dalitz decays (denoted by bkg e) and 87.1% LF. The background identification efficiency for each category is quoted. For completeness, the identification efficiency for prompt leptons from $Z \to e^+e^-$ decays, measured from MC simulation, is also given. The uncertainties are statistical only.

where XX is the size of the employed isolation cone. $E_{\text{T,core}}$ is the energy of the EM calorimeter cells contained in a $\Delta\eta \times \Delta\phi = 5 \times 7$ (in EM-middle-layer cell units) rectangular cluster around the barycentre of the EM cluster and is a measure of the energy of the electron or photon candidate. The advantage of this definition is its robustness in the presence of pile-up. The disadvantage is that it does not subtract all the electron energy and an additional leakage correction, $E_{\text{T,leakage}}$, is needed. This leakage is parameterised as a function of E_T and $|\eta|$ of the electron or photon candidate using MC simulation samples of single electrons and single photons without pile-up. Additionally, a correction for the pile-up and underlying-event

JHEP05(2024)162

contribution to the isolation cone, $E_{\mathrm{T,pile\text{-}up}}$, is estimated in situ event per event, based on the ambient energy density [60], and optimized using a $Z \to e^+e^-$ data sample as described below.

The $E_{\mathrm{T,pile\text{-}up}}$ term in equation (9.1) is measured using an improved methodology compared to refs. [12–14]. Here, $E_{\mathrm{T,pile\text{-}up}}$ is constructed as the median pile-up energy density, ρ^{median}, multiplied by the area delimited by the isolation cone of ΔR. The core area of the 5×7 cluster (see section 3) is subtracted such that $E_{\mathrm{T,pile\text{-}up}}$ represents the median energy deposited by pile-up in the isolation cone. The value of ρ^{median} is measured event-by-event following ref. [60]. For each event, the k_t jet-clustering algorithm [49, 61] with radius parameter $R = 0.5$ is used to construct jets from the topological clusters. Furthermore, the jet transverse momentum (p_T^{jet}) and the jet area (A^{jet}) are used to compute the energy density of each jet ($\rho^{\mathrm{jet}} = p_T^{\mathrm{jet}}/A^{\mathrm{jet}}$) that is then used to calculate the median energy density ρ^{median} from the jets of that event.

The ρ^{median} value should change monotonically as a function of rapidity; however, detector effects introduce non-monotonic dependences. With increasing $|\eta|$ the granularity of the detector becomes coarser and calorimeter cells become larger, thus noise thresholds are set to higher values and therefore soft energy depositions from pile-up are less likely to form topological clusters [20]. As a consequence, ρ^{median} must be determined as a function of η. In the past, ρ^{median} was measured only in two pseudorapidity regions, $|\eta| < 1.5$ and $1.5 < |\eta| < 3.0$ [14] (in the following denoted by "2-region" approach), which fails to reproduce the smooth dependency of the average pile-up density as a function of η. For the results presented here, this procedure has been updated. The modulation f_η of the median energy density relative to a reference value $\rho^{\mathrm{median}}_{\mathrm{central}}$ in a small $|\eta|$-range is used in combination with the event-by-event value of $\rho^{\mathrm{median}}_{\mathrm{central}}$. The value of $\rho^{\mathrm{median}}_{\mathrm{central}}$ is measured in the region $|\eta| < 1.5$ where pile-up density can be reliably determined per event, whereas measurements of densities in smaller areas require averaging over a large number of events. Measuring the modulation f_η of the median energy density relative to a central reference $\rho^{\mathrm{median}}_{\mathrm{central}}$ therefore allows to introduce a smooth variation of the pile-up density as a function of η without suffering from the large fluctuations that occur when ρ^{median} is determined for small $|\eta|$ ranges event-by-event.

The transverse pile-up energy is then calculated as:

$$E_{\mathrm{T,pile\text{-}up}} = \rho^{\mathrm{median}}_{\mathrm{central}} \times \sum_{\eta} A_\eta f_\eta = \rho^{\mathrm{median}}_{\mathrm{central}} \times \zeta(\eta), \tag{9.2}$$

where the f_η denote the energy densities relative to $\rho^{\mathrm{median}}_{\mathrm{central}}$ in a specific η-range and the A_η denotes the area contributing in that bin with the core area of the 5×7 EM cluster removed. The relative modulation ζ_η is the total sum of the energy density relative to $\rho^{\mathrm{median}}_{\mathrm{central}}$ calculated for a specific area, e.g. an isolation cone of $E_{\mathrm{T}}^{\mathrm{cone30}}$, around an axis defined by a given η.

The f_η are determined in $Z \to e^+e^-$ data events by simultaneously fitting the median isolation energy in two isolation rings, $E_{\mathrm{T}}^{\mathrm{cone30}} - E_{\mathrm{T}}^{\mathrm{cone20}}$ and $E_{\mathrm{T}}^{\mathrm{cone40}} - E_{\mathrm{T}}^{\mathrm{cone30}}$, as a function of η and $\rho^{\mathrm{median}}_{\mathrm{central}}$. The areas of the isolation rings defined by $0.2 < \Delta R < 0.3$ and $0.3 < \Delta R < 0.4$ have the advantage of being less sensitive to the energy of the electron leaking into the isolation area; therefore on average the isolation energy is dominated by pile-up. Only electrons with $40\ \mathrm{GeV} < E_{\mathrm{T}} < 45\ \mathrm{GeV}$ are used and backgrounds are negligible. This is referred as the "smooth correction" in the following. Figure 16(a) shows this median isolation energy in the two isolation rings as measured in data as a function of $\rho^{\mathrm{median}}_{\mathrm{central}}$ in one central η-region

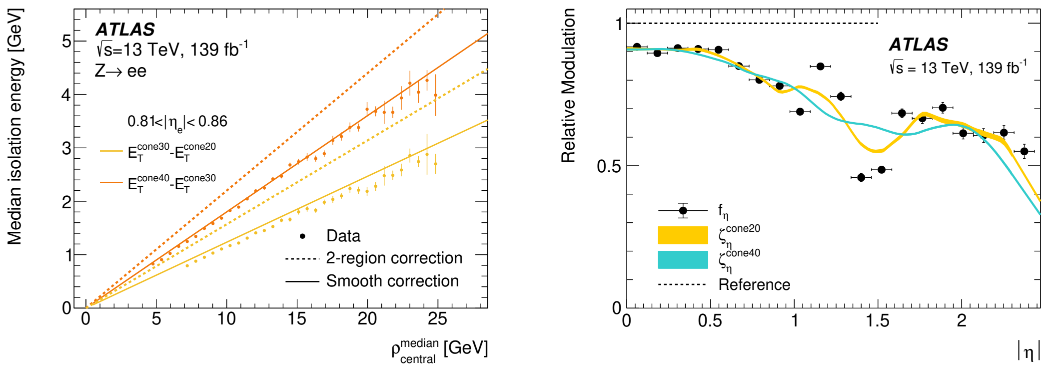

(a) (b)

Figure 16. (a) Median of the isolation distribution without pile-up subtraction as a function of the central ($|\eta| < 1.5$) energy density, for two isolation rings around the electron, in the $0.81 < |\eta| < 0.86$ region. The data points are compared with the improved smooth pile-up subtraction values (solid line), and to the 2-region correction (dashed line), respectively. (b) Fit parameters f_η and resulting ζ_η for $E_{\mathrm{T}}^{\mathrm{cone20}}$ and $E_{\mathrm{T}}^{\mathrm{cone40}}$ versus $|\eta|$. The statistical uncertainty of the fit parameters f_η and the propagated uncertainties on $\zeta(\eta_e)$ are shown. The results are obtained from a $Z \to e^+e^-$ data sample. The range where the reference value of $\rho_{\mathrm{central}}^{\mathrm{median}}$ is measured on an event-by-event basis is also shown as dashed line.

($0.81 < |\eta| < 0.86$). The data measurement is compared with the estimate obtained with the previously used 2-region correction and the new method using the smooth correction. Whilst the former overestimates the data measurement, the latter agrees very well. This is also visible in figure 16(b) where the modulation relative to $\rho_{\mathrm{central}}^{\mathrm{median}}$ are shown for f_η as data points. Additionally, the calculated relative median isolation energy for two specific cone sizes, $\zeta_\eta^{\mathrm{cone20}}$ and $\zeta_\eta^{\mathrm{cone40}}$, are shown as a function of η. It is also notable that the extracted relative median isolation energies are smaller than one. This indicates that the energy density of k_t-jets is not an optimal proxy for the energy density in the fixed sized cones used for the isolation variables, also because k_t -jets are usually clustered around a collimated energy deposit whereas the isolation cones around electromagnetic objects are meant to collect diffuse energy deposits. The $|\eta|$-dependence of the energy from pile-up that is measured as relative modulation is clearly visible.

The performance of the various improvements discussed in this section is illustrated in figure 17, which shows a comparison between the selection efficiencies achievable using the previous method with that of the improved pile-up subtraction method. To help the comparison, the selections on the isolation are chosen such that similar efficiencies in the $|\eta| < 0.6$ region are achieved. The results are obtained from a $Z \to e^+e^-$ data sample with the method described in section 5, using probe electrons with $E_T > 25$ GeV passing the Tight identification selection. As these efficiencies are only for comparison purposes, no background subtraction is performed. It can be seen that the efficiency corresponding to the improved smooth pile-up subtraction method is more stable versus η in the $|\eta| > 1.2$ region. When compared with $E_{\mathrm{T}}^{\mathrm{cone40}}$, a smaller impact is observed for $E_{\mathrm{T}}^{\mathrm{cone20}}$ because of the smaller cone size used to define this calorimeter isolation variable. The improvement leads to better calorimetric isolation at high $|\eta|$ of a few percentage points.

JHEP05(2024)162

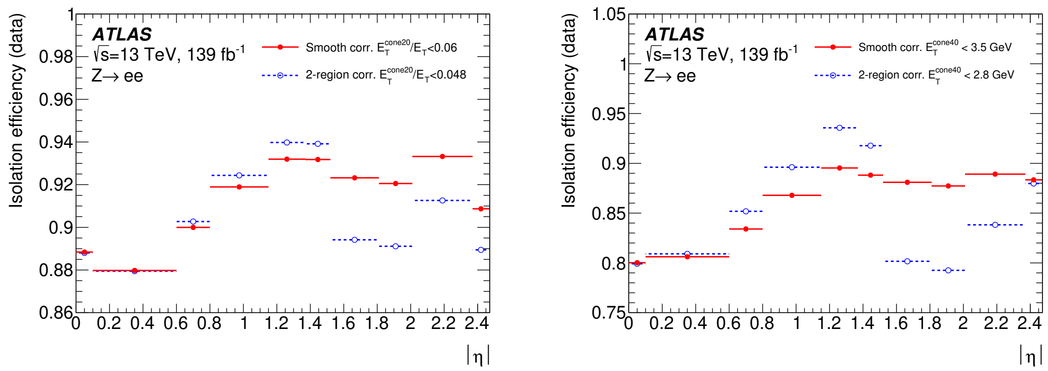

(a) (b)

Figure 17. (a) Efficiency comparison for two calorimeter isolation selection criteria defined with $E_{\mathrm{T}}^{\mathrm{cone20}}$, illustrating the impact of using the 2-region and the improved smooth pile-up corrections discussed in the text. To better see the improvement, the isolation selection criterion defined with the 2-region pile-up correction is chosen such that it has a similar efficiency in the $|\eta| < 0.6$ region. (b) A similar comparison performed for two calorimeter isolation selection criteria defined with $E_{\mathrm{T}}^{\mathrm{cone40}}$. The results are obtained from a $Z \to e^+e^-$ data sample. The efficiencies are computed with the method described in section 5, using probe electrons with $E_T > 25$ GeV passing the Tight identification selection. As these efficiencies are only for comparison purposes, no background subtraction is performed. Only the (very small) statistical uncertainties are shown.

Selection criteria	Calorimeter isolation	Track isolation
HighPtCaloOnly	$E_{\mathrm{T}}^{\mathrm{cone20}} < \max(0.015 \times p_{\mathrm{T}}, 3.5\ \mathrm{GeV})$	—
TightTrackOnly_VarRad	—	$p_{\mathrm{T}}^{\mathrm{varcone30}}/p_{\mathrm{T}} < 0.06$
TightTrackOnly_FixedRad	—	$p_{\mathrm{T}}^{\mathrm{varcone30}}/p_{\mathrm{T}} < 0.06$ for $E_{\mathrm{T}} < 50$ GeV
		$p_{\mathrm{T}}^{\mathrm{cone20}}/p_{\mathrm{T}} < 0.06$ for $E_{\mathrm{T}} > 50$ GeV
Tight_VarRad	$E_{\mathrm{T}}^{\mathrm{cone20}}/p_{\mathrm{T}} < 0.06$	$p_{\mathrm{T}}^{\mathrm{varcone30}}/p_{\mathrm{T}} < 0.06$
Loose_VarRad	$E_{\mathrm{T}}^{\mathrm{cone20}}/p_{\mathrm{T}} < 0.20$	$p_{\mathrm{T}}^{\mathrm{varcone30}}/p_{\mathrm{T}} < 0.15$

Table 2. Definition of the electron isolation selection criteria. All working points use a cone size of $\Delta R = 0.2$ for calorimeter isolation, and $\Delta R_{\mathrm{max}} = 0.3$ or 0.2 for track isolation. $p_{\mathrm{T}}^{\mathrm{varcone30}}$ uses a variable cone size and is defined in equation (3.1).

9.2 Electron isolation criteria and efficiency measurements

The implementation of isolation criteria is specific to the physics analysis needs, and is a compromise between a highly efficient identification of prompt electrons, isolated or produced in a busy environment, and a good rejection of backgrounds. The different electron isolation selection criteria used in ATLAS are presented in table 2, and are defined with fixed requirements on the calorimeter or the track isolation variables. To increase the rejection of hadronic activity, the TightTrackOnly_FixedRad selection criterion use $p_{\mathrm{T}}^{\mathrm{varcone30}}$ for $E_{\mathrm{T}} < 50$ GeV and $p_{\mathrm{T}}^{\mathrm{cone20}}$ for $E_{\mathrm{T}} > 50$ GeV.

Figure 18 shows the electron isolation efficiency measured in data recorded in 2018, and the corresponding data-to-MC simulation ratios as a function of the electron E_{T} and η, and of

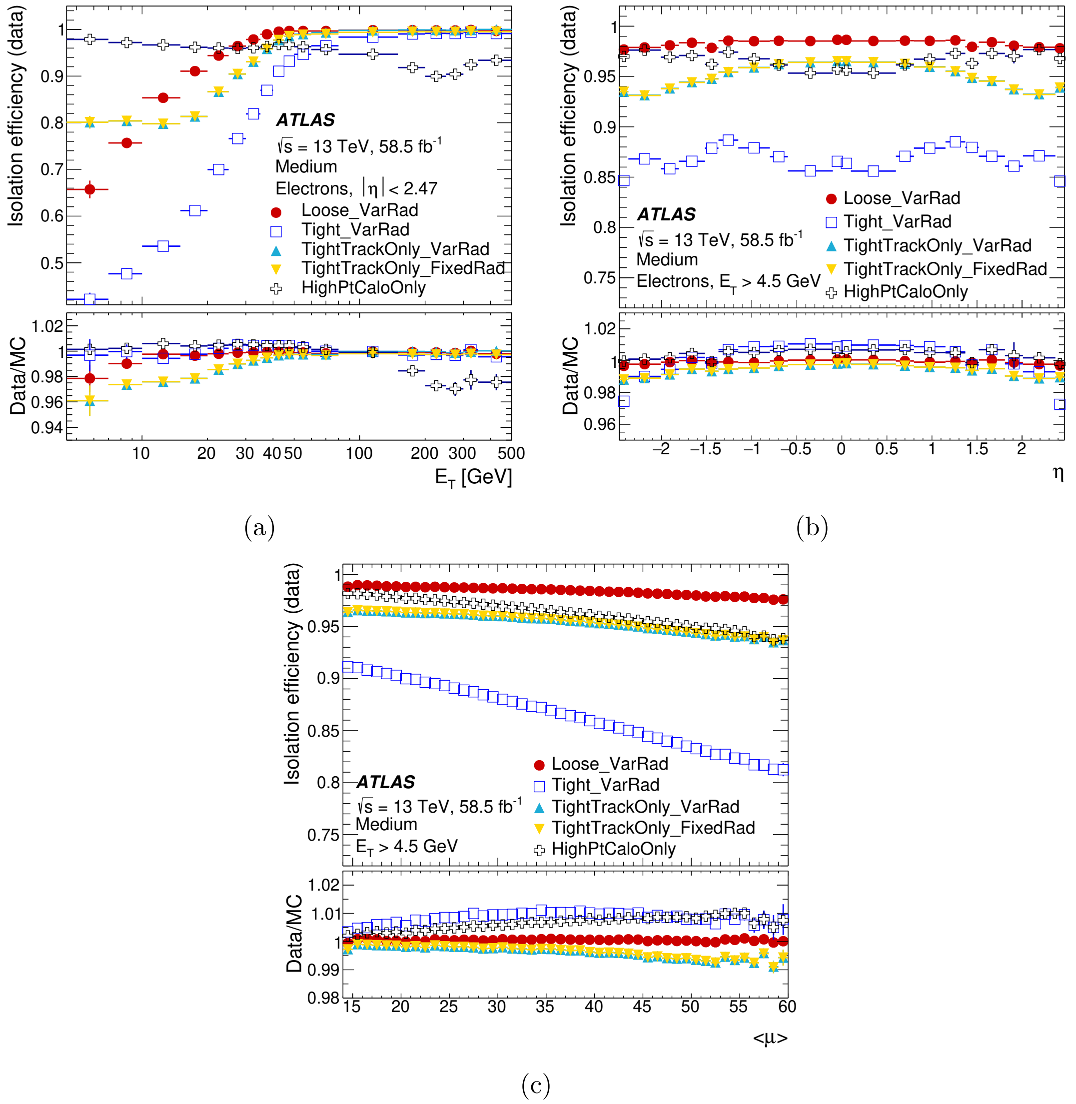

Figure 18. Efficiency of the different isolation working points for electrons from inclusive 2018 data $Z \to e^+e^-$ events as a function of the (a) electron E_{T}, (b) electron η and (c) the average number of interactions per bunch crossing $\langle\mu\rangle$. The electrons are required to fulfil the Medium selection from the likelihood-based electron identification. The lower panel shows the ratio of the efficiencies measured in data and in MC simulations. The total uncertainties are shown, including the statistical and systematic components.

the average number of pile-up interactions $\langle\mu\rangle$ for the isolation selection criteria summarized in table 2. These results are obtained using a sample enriched in $Z \to e^+e^-$ events recorded in 2018, where the probe electrons satisfy the Medium identification selection. Separate measurements were performed also using the Loose and Tight identification selections. The method used to compute the electron isolation efficiency and the associated uncertainties is described in section 7.2. The Tight_VarRad selection criterion gives the highest background rejection below 60 GeV and the most significant difference in shape in η. The HighPtCaloOnly isolation working point gives the highest rejection in the high-E_{T} region ($E_{\mathrm{T}} > 100$ GeV).

JHEP05(2024)162

The behaviour at high E_{T} for HighPtCaloOnly is expected, as the definition of this working point changes around 233 GeV in electron E_{T} (the cut-value for $E_{\mathrm{T}}^{\mathrm{cone20}}$ is changed from $0.015 \times p_{\mathrm{T}}$ to 3.5 GeV). The efficiencies are symmetric for positive and negative values of the pseudo-rapidity for all of the considered isolation working points.

The track isolation variables are largely independent of pile-up, due to the rejection of tracks originating from pile-up vertices or with large transverse impact parameters relative to the primary vertex. This is not the case for the calorimeter isolation [14], as shown in figure 18(c). The Tight_VarRad selection criterion give the highest pile-up dependency, the isolation efficiency decreasing from 91% at low $\langle\mu\rangle$ to 82% when $\langle\mu\rangle$ is around 60.

The overall differences between data and MC simulation are less than 5%–7% depending on the working point, with the largest difference observed for HighPtCaloOnly isolation criterion. For electrons with E_{T} higher than 500 GeV no measurement can be performed because of the limited number of data events, and the results from the [350, 500] GeV bin are linearly extrapolated up to 2 TeV with uncertainties up to 40%, depending on the isolation selection criteria. Overall, the extrapolation uncertainty is dominated by the propagation of the statistical uncertainty in the highest E_{T} measurements.

The efficiency correction factors obtained for the MC simulation are smoothed versus E_{T}, using the SMART smoothing algorithm through ROOT [62, 63], taking into account the statistical uncertainties on the corrections. The statistical uncertainties on the smoothed correction values are estimated with pseudo-data, applying the same smoothing procedure to multiple pseudo-data instances, and computing the root-mean-square of the smoothed pseudo-data values. The total uncertainties on the correction factors range from 5% to less than 0.1% in the E_{T} range from 10 to 200 GeV.

10 Photon identification

Photon identification efficiencies are measured separately for converted and unconverted photons in 68 bins of photon E_{T} and η. For both the converted and unconverted photons the same binning is used with edges at $E_{\mathrm{T}} = \{10, 15, 20, 25, 30, 35, 40, 45, 50, 60, 80, 100, 125, 150, 175, 250, 350, \infty\}$ GeV and $|\eta| = \{0, 0.6, 1.37, 1.52, 1.81, 2.37\}$. No measurements are carried out for the bin defined by $|\eta| = \{1.37, 1.52\}$ as it coincides with the transition region of the ATLAS calorimeter and is not used in analyses using photons.

Photon identification efficiency measurements are carried out using three different methods that are detailed in ref. [22] and that are combined to yield correction factors for analyses. In all cases, photons are required to satisfy the Loose isolation criterion defined in ref. [14] and therefore, in contrast to the presented electron efficiencies, the photon efficiencies are measured relative to this isolation criterion.

For the first method, probe photons from a sample of radiative $Z \to \ell\ell\gamma$ decays are used, collected as described in section 4 and selected by requiring an invariant mass of the three-body system, 80 GeV $< m_{\ell\ell\gamma} <$ 100 GeV, and of the lepton-pair invariant mass, 40 GeV $< m_{\ell\ell} <$ 83 GeV. Backgrounds and signal events are determined using a MC-based template fit to the observed three-body invariant-mass distribution. The main uncertainty in this method comes from the low statistics especially at high photon E_{T} bins, which is the main weakness of the method. The dominant systematic uncertainty comes from the MC generator modelling uncertainty.

A matrix method [22] is used on the second data sample consisting of inclusive photons passing the Loose identification criterion employed in the trigger as described in section 4. This sample is dominated by a background from hadronic jets that must be accounted for. This is achieved using a matrix method that constructs four regions made up of photon candidates that either pass or fail the Tight identification, and pass or fail track-based isolation cuts. For each region, the numbers of signal and background events are unknown. However, since the isolation efficiencies for signal and background from each region are known, the efficiency for photons passing the Loose identification criteria to also satisfy the Tight identification can be extracted. The isolation efficiencies for signal and background are extracted from MC simulation and a jet-enriched control sample selected by inverting identification criteria respectively. This method is only capable of determining the efficiency for Loose photon candidates to pass the Tight selection. Therefore it is further multiplied with the efficiency of reconstructed photon candidates to satisfy the Loose identification as determined from simulation. This correction is however typically less than 5%, and even smaller at high E_{T} where the matrix method has the most impact in the combination of the three measurements. The dominant systematic uncertainty comes from the method's non-closure related to the imperfect assumption that isolation and identification efficiencies employed in the method are perfectly independent of each other.

The third method is called "electron extrapolation" and uses the electrons from $Z \to e^+e^-$ decays employing the same data sample as in the electron efficiency measurements. In the selection, loose photon isolation requirements are applied additionally to the electron candidates. Then, the electron shower shape variables are modified by applying Smirnov transformations to resemble those of photons based on information from simulated $Z \to e^+e^-$ events and the inclusive-photon production sample. After the shower shapes have been modified, the efficiencies are measured using a similar method as for electrons (described in section 5), using the invariant mass distribution of the electron pair to distinguish signal and backgrounds. The method closure uncertainty is the dominant uncertainty at low E_{T} in most of η regions with uncertainties up to 20%. It comes from the method's non-closure connected to ignorance of possible correlations between the different shower shapes during the transformation procedure. However, it decreases as a function of E_{T} and for $E_{\mathrm{T}} > 100$ GeV other sources of uncertainty become important such as limited MC statistics, and variations of the applied Smirnov transformations.

The measurement done using radiative Z-boson decays and the one where the matrix method is applied to an inclusive sample of photons were performed using the full Run 2 data, whilst the measurement using electron extrapolation uses the 2015–2017 data with an integrated luminosity of 81 fb^{-1}. Further details of the measurements and of the determination of systematic uncertainties can be found in ref. [14].

Figures 19 and 20 show the results of the three efficiency measurements for unconverted and converted photons, respectively, as a function of p_{T} in the four different regions of $|\eta|$. The upper panels of the figures only show the data efficiencies, whilst the lower panels display the ratio of the efficiencies determined from data and those observed in MC simulation. Before determining the efficiencies in the MC simulation, the photon shower shapes were corrected to better match the data as described in ref. [22]. Similarly, in analyses, first the photon shower shapes are corrected and then the data-to-MC simulation ratio is applied to account for residual differences between the identification selection efficiencies. For this purpose, the data-to-MC simulation ratios from the three measurement methods described above are combined using a weighted average in each E_{T}–η bin, assuming the statistical and systematic uncertainties to be uncorrelated among the methods. For the statistical uncertainties, this is an approximation, but one that largely holds: the electron extrapolation uses an independent data sample, whilst there is some overlap between the sample of radiative Z-boson decays used and the inclusive sample of photons, which contains the former. However most of the events in the inclusive photon sample stem from photon+jet production.

The result of the combination of the efficiency ratios is also shown in the lower panels of figures 19 and 20. The total uncertainty of the combined ratio ranges between 5% at low E_{T} and about 0.4% at high E_{T} for unconverted photons, and between 7% (low E_{T}) and about 0.7% (high E_{T}) for converted photons. The over-all improvement is of the order of 30%–40%, slightly larger than what is expected from the increase in statistics alone, as some aspects of the determination of the systematic uncertainty are also statistically limited.

JHEP05(2024)162

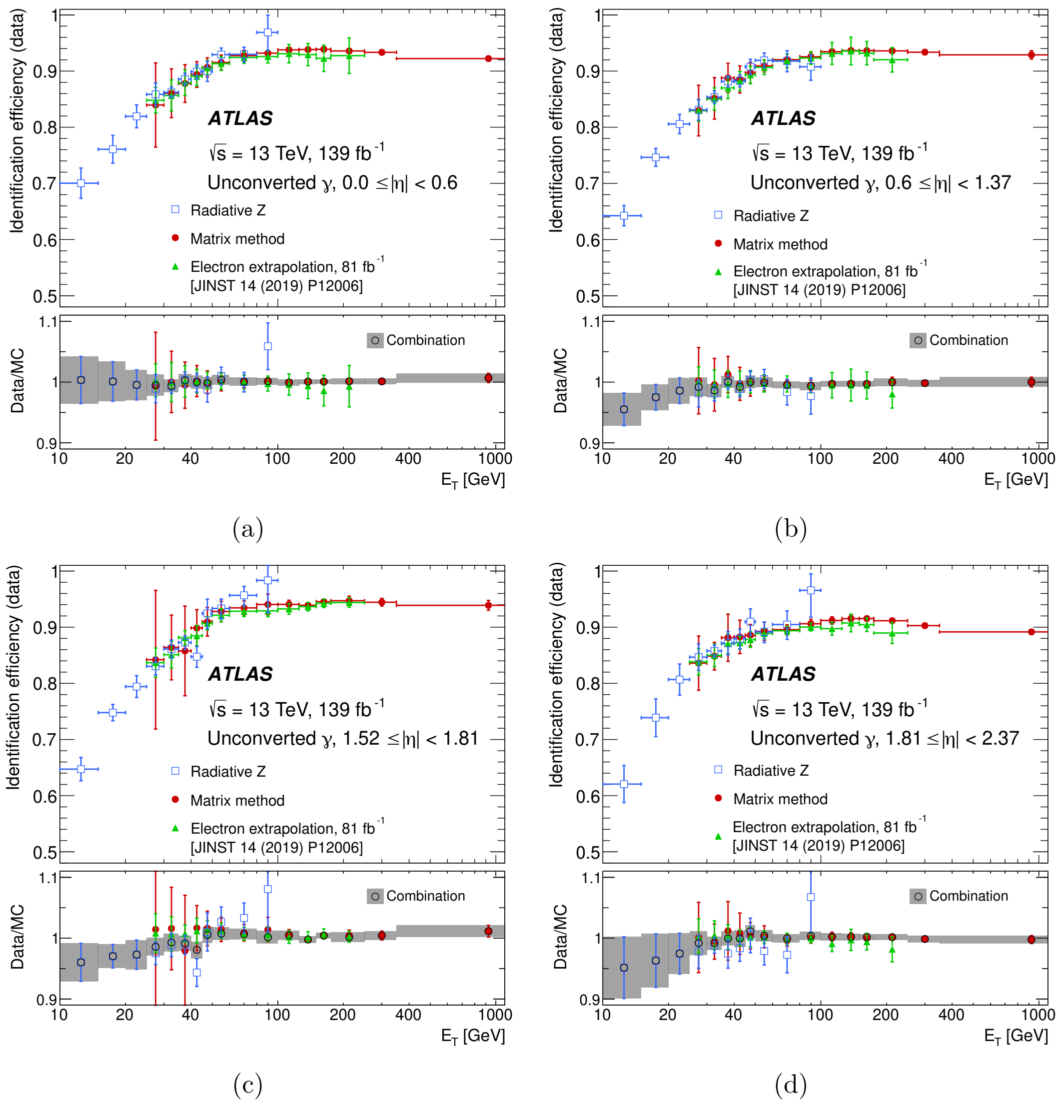

Figure 19. The photon identification efficiency measured in data, and the ratio of data-to-MC simulation efficiencies, for unconverted photons with a Loose isolation requirement applied as preselection, as a function of E_{T} in four different $|\eta|$ regions. The results for the electron extrapolation were not updated with regards to ref. [14]. The combined correction factor, obtained using a weighted average of correction factors from the individual measurements, is also presented; the band represents the total uncertainty.

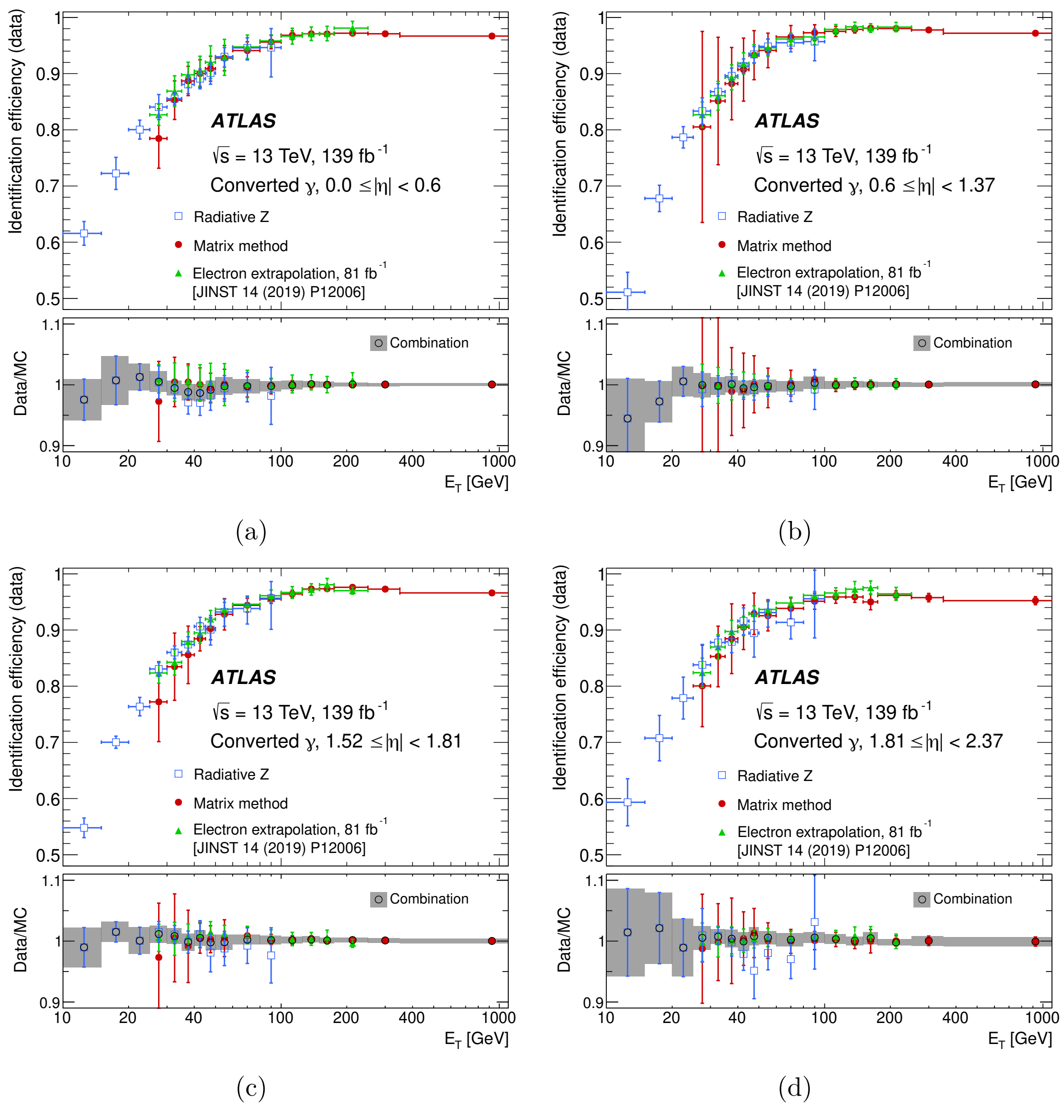

Figure 20. The photon identification efficiency measured in data, and the ratio of data-to-MC simulation efficiencies, for converted photons with a Loose isolation requirement applied as preselection, as a function of E_{T} in four different $|\eta|$ regions. The result for the electron extrapolation were not updated with regards to ref. [14]. The combined scale factor, obtained using a weighted average of scale factors from the individual measurements, is also presented; the band represents the total uncertainty.

11 Conclusion

Measurements of electron reconstruction, identification, and isolation efficiencies, and photon efficiencies have been presented. These use the full Run 2 data with a luminosity of 139 fb^{-1} collected by the ATLAS experiment during the years 2015–2018. The uncertainties on these results are up to 50% smaller than the previously published measurements. The improvements have been achieved not only by including more data but more importantly by significant updates to the methodology of the measurements used, including optimising the background subtraction and the combination of measurements, and the update of the subtraction of pile-up contamination in the case of selections based on isolation variables. These measurements and the derived correction factors are to-date the most precise measurements using the Run 2 data and are the basis of ATLAS precision analyses in the Higgs boson, electroweak, and top quark sector. Improvements in the definitions of the isolation variables enhanced the stability of the signal efficiencies over the full η range and significantly increased the rejection of non-prompt electrons at large transverse momenta. The presented measurements will have a significant impact on future ATLAS precision measurements.

Acknowledgments

We thank CERN for the very successful operation of the LHC and its injectors, as well as the support staff at CERN and at our institutions worldwide without whom ATLAS could not be operated efficiently.

The crucial computing support from all WLCG partners is acknowledged gratefully, in particular from CERN, the ATLAS Tier-1 facilities at TRIUMF/SFU (Canada), NDGF (Denmark, Norway, Sweden), CC-IN2P3 (France), KIT/GridKA (Germany), INFN-CNAF (Italy), NL-T1 (Netherlands), PIC (Spain), RAL (U.K.) and BNL (U.S.A.), the Tier-2 facilities worldwide and large non-WLCG resource providers. Major contributors of computing resources are listed in ref. [64].

We gratefully acknowledge the support of ANPCyT, Argentina; YerPhI, Armenia; ARC, Australia; BMWFW and FWF, Austria; ANAS, Azerbaijan; CNPq and FAPESP, Brazil; NSERC, NRC and CFI, Canada; CERN; ANID, Chile; CAS, MOST and NSFC, China; Minciencias, Colombia; MEYS CR, Czech Republic; DNRF and DNSRC, Denmark; IN2P3-CNRS and CEA-DRF/IRFU, France; SRNSFG, Georgia; BMBF, HGF and MPG, Germany; GSRI, Greece; RGC and Hong Kong SAR, China; ISF and Benoziyo Center, Israel; INFN, Italy; MEXT and JSPS, Japan; CNRST, Morocco; NWO, Netherlands; RCN, Norway; MEiN, Poland; FCT, Portugal; MNE/IFA, Romania; MESTD, Serbia; MSSR, Slovakia; ARRS and MIZŠ, Slovenia; DSI/NRF, South Africa; MICINN, Spain; SRC and Wallenberg Foundation, Sweden; SERI, SNSF and Cantons of Bern and Geneva, Switzerland; MOST, Taipei; TENMAK, Türkiye; STFC, United Kingdom; DOE and NSF, United States of America.

Individual groups and members have received support from BCKDF, CANARIE, CRC and DRAC, Canada; CERN-CZ, PRIMUS 21/SCI/017 and UNCE SCI/013, Czech Republic; COST, ERC, ERDF, Horizon 2020, ICSC-NextGenerationEU and Marie Skłodowska-Curie Actions, European Union; Investissements d'Avenir Labex, Investissements d'Avenir Idex and ANR, France; DFG and AvH Foundation, Germany; Herakleitos, Thales and Aristeia

JHEP05(2024)162

programmes co-financed by EU-ESF and the Greek NSRF, Greece; BSF-NSF and MINERVA, Israel; Norwegian Financial Mechanism 2014-2021, Norway; NCN and NAWA, Poland; La Caixa Banking Foundation, CERCA Programme Generalitat de Catalunya and PROMETEO and GenT Programmes Generalitat Valenciana, Spain; Göran Gustafssons Stiftelse, Sweden; The Royal Society and Leverhulme Trust, United Kingdom.

In addition, individual members wish to acknowledge support from Chile: Agencia Nacional de Investigación y Desarrollo (FONDECYT 1190886, FONDECYT 1210400, FONDECYT 1230987); China: National Natural Science Foundation of China (NSFC — 12175119, NSFC 12275265); European Union: European Research Council (ERC — 948254), Horizon 2020 Framework Programme (MUCCA — CHIST-ERA-19-XAI-00), Italian Center for High Performance Computing, Big Data and Quantum Computing (ICSC, NextGenerationEU), Marie Sklodowska-Curie Actions (EU H2020 MSC IF GRANT NO 101033496); France: Agence Nationale de la Recherche (ANR-20-CE31-0013, ANR-21-CE31-0013, ANR-21-CE31-0022), Investissements d'Avenir Idex (ANR-11-LABX-0012), Investissements d'Avenir Labex (ANR-11-LABX-0012); Germany: Baden-Württemberg Stiftung (BW Stiftung-Postdoc Eliteprogramme), Deutsche Forschungsgemeinschaft (DFG — CR 312/5-1); Italy: Istituto Nazionale di Fisica Nucleare (FELLINI G.A. n. 754496, ICSC, NextGenerationEU); Japan: Japan Society for the Promotion of Science (JSPS KAKENHI 22H01227, JSPS KAKENHI JP21H05085, JSPS KAKENHI JP22H04944); Netherlands: Netherlands Organisation for Scientific Research (NWO Veni 2020 — VI.Veni.202.179); Norway: Research Council of Norway (RCN-314472); Poland: Polish National Agency for Academic Exchange (PPN/PPO/2020/1/00002/U/00001), Polish National Science Centre (NCN 2021/42/E/ST2/00350, NCN UMO-2019/34/E/ST2/00393, UMO-2020/37/B/ST2/01043, UMO-2021/40/C/ST2/00187); Slovenia: Slovenian Research Agency (ARIS grant J1-3010); Spain: BBVA Foundation (LEO22-1-603), Generalitat Valenciana (Artemisa, FEDER, IDIFEDER/2018/048), La Caixa Banking Foundation (LCF/BQ/PI20/11760025), Ministry of Science and Innovation (RYC2019-028510-I, RYC2020-030254-I), PROMETEO and GenT Programmes Generalitat Valenciana (CIDEGENT/2019/023, CIDEGENT/2019/027); Sweden: Swedish Research Council (VR 2022-03845, VR 2022-04683), Knut and Alice Wallenberg Foundation (KAW 2017.0100, KAW 2018.0157, KAW 2019.0447); Switzerland: Swiss National Science Foundation (SNSF — PCEFP2_194658); United Kingdom: Leverhulme Trust (Leverhulme Trust RPG-2020-004); United States of America: Neubauer Family Foundation.

References

[1] ATLAS collaboration, *The ATLAS experiment at the CERN Large Hadron Collider*, 2008 *JINST* **3** S08003 [INSPIRE].

[2] ATLAS collaboration, *ATLAS Insertable B-Layer technical design report*, CERN-LHCC-2010-013, CERN, Geneva, Switzerland (2010).

[3] ATLAS IBL collaboration, *Production and integration of the ATLAS Insertable B-Layer*, 2018 *JINST* **13** T05008 [arXiv:1803.00844] [INSPIRE].

[4] L. Evans and P. Bryant, *LHC machine*, 2008 *JINST* **3** S08001 [INSPIRE].

[5] ATLAS collaboration, *Observation of a new particle in the search for the Standard Model Higgs boson with the ATLAS detector at the LHC*, *Phys. Lett. B* **716** (2012) 1 [arXiv:1207.7214] [INSPIRE].

[6] CMS collaboration, *Observation of a new boson with mass near* 125 *GeV in pp collisions at* $\sqrt{s} = 7$ *and* 8 *TeV*, *JHEP* **06** (2013) 081 [arXiv:1303.4571] [INSPIRE].

[7] ATLAS collaboration, *Measurement of the forward-backward asymmetry of electron and muon pair-production in pp collisions at* $\sqrt{s} = 7$ *TeV with the ATLAS detector*, *JHEP* **09** (2015) 049 [arXiv:1503.03709] [INSPIRE].

[8] ATLAS collaboration, *Measurement of the W-boson mass in pp collisions at* $\sqrt{s} = 7$ *TeV with the ATLAS detector*, *Eur. Phys. J. C* **78** (2018) 110 [*Erratum ibid.* **78** (2018) 898] [arXiv:1701.07240] [INSPIRE].

[9] ATLAS collaboration, *Measurement of angular correlations in Drell-Yan lepton pairs to probe* $Z/\gamma*$ *boson transverse momentum at* $\sqrt{s} = 7$ *TeV with the ATLAS detector*, *Phys. Lett. B* **720** (2013) 32 [arXiv:1211.6899] [INSPIRE].

[10] ATLAS collaboration, *Measurement of the Drell-Yan triple-differential cross section in pp collisions at* $\sqrt{s} = 8$ *TeV*, *JHEP* **12** (2017) 059 [arXiv:1710.05167] [INSPIRE].

[11] ATLAS collaboration, *Measurement of the total and differential Higgs boson production cross-sections at* $\sqrt{s} = 13$ *TeV with the ATLAS detector by combining the* $H \to ZZ^* \to 4\ell$ *and* $H \to \gamma\gamma$ *decay channels*, *JHEP* **05** (2023) 028 [arXiv:2207.08615] [INSPIRE].

[12] ATLAS collaboration, *Electron efficiency measurements with the ATLAS detector using* 2012 *LHC proton-proton collision data*, *Eur. Phys. J. C* **77** (2017) 195 [arXiv:1612.01456] [INSPIRE].

[13] ATLAS collaboration, *Electron reconstruction and identification in the ATLAS experiment using the* 2015 *and* 2016 *LHC proton-proton collision data at* $\sqrt{s} = 13$ *TeV*, *Eur. Phys. J. C* **79** (2019) 639 [arXiv:1902.04655] [INSPIRE].

[14] ATLAS collaboration, *Electron and photon performance measurements with the ATLAS detector using the* 2015–2017 *LHC proton-proton collision data*, 2019 *JINST* **14** P12006 [arXiv:1908.00005] [INSPIRE].

[15] ATLAS collaboration, *Performance of electron and photon triggers in ATLAS during LHC run* 2, *Eur. Phys. J. C* **80** (2020) 47 [arXiv:1909.00761] [INSPIRE].

[16] ATLAS collaboration, *Electron and photon energy calibration with the ATLAS detector using* 2015–2016 *LHC proton-proton collision data*, 2019 *JINST* **14** P03017 [arXiv:1812.03848] [INSPIRE].

[17] ATLAS collaboration, *Performance of the ATLAS trigger system in* 2015, *Eur. Phys. J. C* **77** (2017) 317 [arXiv:1611.09661] [INSPIRE].

[18] ATLAS collaboration, *The ATLAS collaboration software and firmware*, ATL-SOFT-PUB-2021-001, CERN, Geneva, Switzerland (2021).

[19] W. Lampl et al., *Calorimeter clustering algorithms: description and performance*, ATL-LARG-PUB-2008-002, CERN, Geneva, Switzerland (2008).

[20] ATLAS collaboration, *Topological cell clustering in the ATLAS calorimeters and its performance in LHC run* 1, *Eur. Phys. J. C* **77** (2017) 490 [arXiv:1603.02934] [INSPIRE].

JHEP05(2024)162

[21] T. Cornelissen et al., *Concepts, design and implementation of the ATLAS New Tracking (NEWT)*, ATL-SOFT-PUB-2007-007, CERN, Geneva, Switzerland (2007).

[22] ATLAS collaboration, *Measurement of the photon identification efficiencies with the ATLAS detector using LHC run* 2 *data collected in* 2015 *and* 2016, *Eur. Phys. J. C* **79** (2019) 205 [arXiv:1810.05087] [INSPIRE].

[23] ATLAS collaboration, *Measurement of the photon identification efficiencies with the ATLAS detector using LHC run*-1 *data*, *Eur. Phys. J. C* **76** (2016) 666 [arXiv:1606.01813] [INSPIRE].

[24] N.J. Buchanan et al., *Design and implementation of the front end board for the readout of the ATLAS liquid argon calorimeters*, 2008 *JINST* **3** P03004 [INSPIRE].

[25] S. Frixione, P. Nason and G. Ridolfi, *A positive-weight next-to-leading-order Monte Carlo for heavy flavour hadroproduction*, *JHEP* **09** (2007) 126 [arXiv:0707.3088] [INSPIRE].

[26] P. Nason, *A new method for combining NLO QCD with shower Monte Carlo algorithms*, *JHEP* **11** (2004) 040 [hep-ph/0409146] [INSPIRE].

[27] S. Frixione, P. Nason and C. Oleari, *Matching NLO QCD computations with parton shower simulations: the POWHEG method*, *JHEP* **11** (2007) 070 [arXiv:0709.2092] [INSPIRE].

[28] S. Alioli, P. Nason, C. Oleari and E. Re, *A general framework for implementing NLO calculations in shower Monte Carlo programs: the POWHEG BOX*, *JHEP* **06** (2010) 043 [arXiv:1002.2581] [INSPIRE].

[29] NNPDF collaboration, *Parton distributions for the LHC run II*, *JHEP* **04** (2015) 040 [arXiv:1410.8849] [INSPIRE].

[30] ATLAS collaboration, *Studies on top-quark Monte Carlo modelling for Top*2016, ATL-PHYS-PUB-2016-020, CERN, Geneva, Switzerland (2016).

[31] T. Sjöstrand et al., *An introduction to PYTHIA* 8.2, *Comput. Phys. Commun.* **191** (2015) 159 [arXiv:1410.3012] [INSPIRE].

[32] ATLAS collaboration, *ATLAS Pythia* 8 *tunes to* 7 *TeV data*, ATL-PHYS-PUB-2014-021, CERN, Geneva, Switzerland (2014).

[33] R.D. Ball et al., *Parton distributions with LHC data*, *Nucl. Phys. B* **867** (2013) 244 [arXiv:1207.1303] [INSPIRE].

[34] D.J. Lange, *The EvtGen particle decay simulation package*, *Nucl. Instrum. Meth. A* **462** (2001) 152 [INSPIRE].

[35] ATLAS collaboration, *ATLAS data quality operations and performance for* 2015–2018 *data-taking*, 2020 *JINST* **15** P04003 [arXiv:1911.04632] [INSPIRE].

[36] ATLAS collaboration, *Luminosity determination in pp collisions at* $\sqrt{s} = 13$ *TeV using the ATLAS detector at the LHC*, ATLAS-CONF-2019-021, CERN, Geneva, Switzerland (2019).

[37] G. Avoni et al., *The new LUCID-*2 *detector for luminosity measurement and monitoring in ATLAS*, 2018 *JINST* **13** P07017 [INSPIRE].

[38] ATLAS collaboration, *Luminosity determination in pp collisions at* $\sqrt{s} = 13$ *TeV using the ATLAS detector at the LHC*, *Eur. Phys. J. C* **83** (2023) 982 [arXiv:2212.09379] [INSPIRE].

[39] ATLAS collaboration, *Performance of the ATLAS muon triggers in run* 2, 2020 *JINST* **15** P09015 [arXiv:2004.13447] [INSPIRE].

[40] ATLAS collaboration, *Muon reconstruction and identification efficiency in ATLAS using the full run 2 pp collision data set at* $\sqrt{s} = 13$ *TeV*, *Eur. Phys. J. C* **81** (2021) 578 [arXiv:2012.00578] [INSPIRE].

[41] ATLAS collaboration, *The ATLAS simulation infrastructure*, *Eur. Phys. J. C* **70** (2010) 823 [arXiv:1005.4568] [INSPIRE].

[42] GEANT4 collaboration, *GEANT4 — a simulation toolkit*, *Nucl. Instrum. Meth. A* **506** (2003) 250 [INSPIRE].

[43] ATLAS collaboration, *The Pythia 8 A3 tune description of ATLAS minimum bias and inelastic measurements incorporating the Donnachie-Landshoff diffractive model*, ATL-PHYS-PUB-2016-017, CERN, Geneva, Switzerland (2016).

[44] ATLAS collaboration, *Summary of ATLAS Pythia 8 tunes*, ATL-PHYS-PUB-2012-003, CERN, Geneva, Switzerland (2012).

[45] ATLAS collaboration, *Measurement of the inelastic proton-proton cross section at* $\sqrt{s} = 13$ *TeV with the ATLAS detector at the LHC*, *Phys. Rev. Lett.* **117** (2016) 182002 [arXiv:1606.02625] [INSPIRE].

[46] ATLAS collaboration, *Performance of the ATLAS track reconstruction algorithms in dense environments in LHC run 2*, *Eur. Phys. J. C* **77** (2017) 673 [arXiv:1704.07983] [INSPIRE].

[47] ATLAS collaboration, *Electron efficiency measurements with the ATLAS detector using the 2015 LHC proton-proton collision data*, ATLAS-CONF-2016-024, CERN, Geneva, Switzerland (2016).

[48] M. Cacciari, G.P. Salam and G. Soyez, *The anti-*k_t *jet clustering algorithm*, *JHEP* **04** (2008) 063 [arXiv:0802.1189] [INSPIRE].

[49] M. Cacciari, G.P. Salam and G. Soyez, *FastJet user manual*, *Eur. Phys. J. C* **72** (2012) 1896 [arXiv:1111.6097] [INSPIRE].

[50] PARTICLE DATA GROUP collaboration, *Review of particle physics*, *PTEP* **2020** (2020) 083C01 [INSPIRE].

[51] ATLAS collaboration, *Measurement of the differential cross-sections of prompt and non-prompt production of* J/ψ *and* $\psi(2S)$ *in pp collisions at* $\sqrt{s} = 7$ *and 8 TeV with the ATLAS detector*, *Eur. Phys. J. C* **76** (2016) 283 [arXiv:1512.03657] [INSPIRE].

[52] ATLAS collaboration, *Measurement of the differential cross-sections of inclusive, prompt and non-prompt* J/ψ *production in proton-proton collisions at* $\sqrt{s} = 7$ *TeV*, *Nucl. Phys. B* **850** (2011) 387 [arXiv:1104.3038] [INSPIRE].

[53] M. Schmelling, *Averaging correlated data*, *Phys. Scripta* **51** (1995) 676 [INSPIRE].

[54] H1 collaboration, *Measurement of the inclusive ep scattering cross section at low* Q^2 *and* x *at HERA*, *Eur. Phys. J. C* **63** (2009) 625 [arXiv:0904.0929] [INSPIRE].

[55] ATLAS collaboration, *Measurements of the Higgs boson inclusive and differential fiducial cross sections in the* 4ℓ *decay channel at* $\sqrt{s} = 13$ *TeV*, *Eur. Phys. J. C* **80** (2020) 942 [arXiv:2004.03969] [INSPIRE].

[56] ATLAS collaboration, *Electron reconstruction and identification efficiency measurements with the ATLAS detector using the 2011 LHC proton-proton collision data*, *Eur. Phys. J. C* **74** (2014) 2941 [arXiv:1404.2240] [INSPIRE].

[57] ATLAS collaboration, *Performance of pile-up mitigation techniques for jets in pp collisions at* $\sqrt{s} = 8$ *TeV using the ATLAS detector*, *Eur. Phys. J. C* **76** (2016) 581 [arXiv:1510.03823] [INSPIRE].

[58] ATLAS collaboration, *Identification and rejection of pile-up jets at high pseudorapidity with the ATLAS detector*, *Eur. Phys. J. C* **77** (2017) 580 [*Erratum ibid.* **77** (2017) 712] [arXiv:1705.02211] [INSPIRE].

[59] ATLAS collaboration, *Jet energy scale and resolution measured in proton-proton collisions at $\sqrt{s} = 13$ TeV with the ATLAS detector*, *Eur. Phys. J. C* **81** (2021) 689 [arXiv:2007.02645] [INSPIRE].

[60] M. Cacciari and G.P. Salam, *Pileup subtraction using jet areas*, *Phys. Lett. B* **659** (2008) 119 [arXiv:0707.1378] [INSPIRE].

[61] S.D. Ellis and D.E. Soper, *Successive combination jet algorithm for hadron collisions*, *Phys. Rev. D* **48** (1993) 3160 [hep-ph/9305266] [INSPIRE].

[62] J.H. Friedman, *SMART user's guide*, Laboratory for Computational Statistics, Stanford University Technical Report No. 1, U.S.A. (1984).

[63] R. Brun and F. Rademakers, *ROOT: an object oriented data analysis framework*, *Nucl. Instrum. Meth. A* **389** (1997) 81 [INSPIRE].

[64] ATLAS collaboration, *ATLAS computing acknowledgements*, ATL-SOFT-PUB-2023-001, CERN, Geneva, Switzerland (2023).

The ATLAS collaboration

G. Aad[102], B. Abbott[120], K. Abeling[55], N.J. Abicht[49], S.H. Abidi[29], A. Aboulhorma[35e], H. Abramowicz[151], H. Abreu[150], Y. Abulaiti[117], B.S. Acharya[69a,69b,m], C. Adam Bourdarios[4], L. Adamczyk[86a], L. Adamek[155], S.V. Addepalli[26], M.J. Addison[101], J. Adelman[115], A. Adiguzel[21c], T. Adye[134], A.A. Affolder[136], Y. Afik[36], M.N. Agaras[13], J. Agarwala[73a,73b], A. Aggarwal[100], C. Agheorghiesei[27c], A. Ahmad[36], F. Ahmadov[38,y], W.S. Ahmed[104], S. Ahuja[95], X. Ai[62a], G. Aielli[76a,76b], A. Aikot[163], M. Ait Tamlihat[35e], B. Aitbenchikh[35a], I. Aizenberg[169], M. Akbiyik[100], T.P.A. Åkesson[98], A.V. Akimov[37], D. Akiyama[168], N.N. Akolkar[24], K. Al Khoury[41], G.L. Alberghi[23b], J. Albert[165], P. Albicocco[53], G.L. Albouy[60], S. Alderweireldt[52], M. Aleksa[36], I.N. Aleksandrov[38], C. Alexa[27b], T. Alexopoulos[10], F. Alfonsi[23b], M. Algren[56], M. Alhroob[120], B. Ali[132], H.M.J. Ali[91], S. Ali[148], S.W. Alibocus[92], M. Aliev[145], G. Alimonti[71a], W. Alkakhi[55], C. Allaire[66], B.M.M. Allbrooke[146], J.F. Allen[52], C.A. Allendes Flores[137f], P.P. Allport[20], A. Aloisio[72a,72b], F. Alonso[90], C. Alpigiani[138], M. Alvarez Estevez[99], A. Alvarez Fernandez[100], M. Alves Cardoso[56], M.G. Alviggi[72a,72b], M. Aly[101], Y. Amaral Coutinho[83b], A. Ambler[104], C. Amelung[36], M. Amerl[101], C.G. Ames[109], D. Amidei[106], S.P. Amor Dos Santos[130a], K.R. Amos[163], V. Ananiev[125], C. Anastopoulos[139], T. Andeen[11], J.K. Anders[36], S.Y. Andrean[47a,47b], A. Andreazza[71a,71b], S. Angelidakis[9], A. Angerami[41,ab], A.V. Anisenkov[37], A. Annovi[74a], C. Antel[56], M.T. Anthony[139], E. Antipov[145], M. Antonelli[53], F. Anulli[75a], M. Aoki[84], T. Aoki[153], J.A. Aparisi Pozo[163], M.A. Aparo[146], L. Aperio Bella[48], C. Appelt[18], A. Apyan[26], N. Aranzabal[36], S.J. Arbiol Val[87], C. Arcangeletti[53], A.T.H. Arce[51], E. Arena[92], J-F. Arguin[108], S. Argyropoulos[54], J.-H. Arling[48], O. Arnaez[4], H. Arnold[114], G. Artoni[75a,75b], H. Asada[111], K. Asai[118], S. Asai[153], N.A. Asbah[61], K. Assamagan[29], R. Astalos[28a], S. Atashi[160], R.J. Atkin[33a], M. Atkinson[162], H. Atmani[35f], P.A. Atmasiddha[106], K. Augsten[132], S. Auricchio[72a,72b], A.D. Auriol[20], V.A. Austrup[101], G. Avolio[36], K. Axiotis[56], G. Azuelos[108,ag], D. Babal[28b], H. Bachacou[135], K. Bachas[152,p], A. Bachiu[34], F. Backman[47a,47b], A. Badea[61], P. Bagnaia[75a,75b], M. Bahmani[18], A.J. Bailey[163], V.R. Bailey[162], J.T. Baines[134], L. Baines[94], O.K. Baker[172], E. Bakos[15], D. Bakshi Gupta[8], V. Balakrishnan[120], R. Balasubramanian[114], E.M. Baldin[37], P. Balek[86a], E. Ballabene[23b,23a], F. Balli[135], L.M. Baltes[63a], W.K. Balunas[32], J. Balz[100], E. Banas[87], M. Bandieramonte[129], A. Bandyopadhyay[24], S. Bansal[24], L. Barak[151], M. Barakat[48], E.L. Barberio[105], D. Barberis[57b,57a], M. Barbero[102], M.Z. Barel[114], K.N. Barends[33a], T. Barillari[110], M-S. Barisits[36], T. Barklow[143], P. Baron[122], D.A. Baron Moreno[101], A. Baroncelli[62a], G. Barone[29], A.J. Barr[126], J.D. Barr[96], L. Barranco Navarro[47a,47b], F. Barreiro[99], J. Barreiro Guimarães da Costa[14a], U. Barron[151], M.G. Barros Teixeira[130a], S. Barsov[37], F. Bartels[63a], R. Bartoldus[143], A.E. Barton[91], P. Bartos[28a], A. Basan[100], M. Baselga[49], A. Bassalat[66,b], M.J. Basso[156a], C.R. Basson[101], R.L. Bates[59], S. Batlamous[35e], J.R. Batley[32], B. Batool[141], M. Battaglia[136], D. Battulga[18], M. Bauce[75a,75b], M. Bauer[36], P. Bauer[24], L.T. Bazzano Hurrell[30], J.B. Beacham[51], T. Beau[127], J.Y. Beaucamp[90], P.H. Beauchemin[158], F. Becherer[54], P. Bechtle[24], H.P. Beck[19,o], K. Becker[167], C. Becot[48], A.J. Beddall[82], V.A. Bednyakov[38], C.P. Bee[145], L.J. Beemster[15],

JHEP05(2024)162

T.A. Beermann[36], M. Begalli[83d], M. Begel[29], A. Behera[145], J.K. Behr[48], J.F. Beirer[55], F. Beisiegel[24], M. Belfkir[159], G. Bella[151], L. Bellagamba[23b], A. Bellerive[34], P. Bellos[20], K. Beloborodov[37], D. Benchekroun[35a], F. Bendebba[35a], Y. Benhammou[151], M. Benoit[29], J.R. Bensinger[26], S. Bentvelsen[114], L. Beresford[48], M. Beretta[53], E. Bergeaas Kuutmann[161], N. Berger[4], B. Bergmann[132], J. Beringer[17a], G. Bernardi[5], C. Bernius[143], F.U. Bernlochner[24], F. Bernon[36,102], T. Berry[95], P. Berta[133], A. Berthold[50], I.A. Bertram[91], S. Bethke[110], A. Betti[75a,75b], A.J. Bevan[94], N.K. Bhalla[54], M. Bhamjee[33c], S. Bhatta[145], D.S. Bhattacharya[166], P. Bhattarai[143], V.S. Bhopatkar[121], R. Bi[29,aj], R.M. Bianchi[129], G. Bianco[23b,23a], O. Biebel[109], R. Bielski[123], M. Biglietti[77a], M. Bindi[55], A. Bingul[21b], C. Bini[75a,75b], A. Biondini[92], C.J. Birch-sykes[101], G.A. Bird[20,134], M. Birman[169], M. Biros[133], S. Biryukov[146], T. Bisanz[49], E. Bisceglie[43b,43a], J.P. Biswal[134], D. Biswas[141], A. Bitadze[101], K. Bjørke[125], I. Bloch[48], C. Blocker[26], A. Blue[59], U. Blumenschein[94], J. Blumenthal[100], G.J. Bobbink[114], V.S. Bobrovnikov[37], M. Boehler[54], B. Boehm[166], D. Bogavac[36], A.G. Bogdanchikov[37], C. Bohm[47a], V. Boisvert[95], P. Bokan[48], T. Bold[86a], M. Bomben[5], M. Bona[94], M. Boonekamp[135], C.D. Booth[95], A.G. Borbély[59], I.S. Bordulev[37], H.M. Borecka-Bielska[108], G. Borissov[91], D. Bortoletto[126], D. Boscherini[23b], M. Bosman[13], J.D. Bossio Sola[36], K. Bouaouda[35a], N. Bouchhar[163], J. Boudreau[129], E.V. Bouhova-Thacker[91], D. Boumediene[40], R. Bouquet[165], A. Boveia[119], J. Boyd[36], D. Boye[29], I.R. Boyko[38], J. Bracinik[20], N. Brahimi[62d], G. Brandt[171], O. Brandt[32], F. Braren[48], B. Brau[103], J.E. Brau[123], R. Brener[169], L. Brenner[114], R. Brenner[161], S. Bressler[169], D. Britton[59], D. Britzger[110], I. Brock[24], G. Brooijmans[41], W.K. Brooks[137f], E. Brost[29], L.M. Brown[165], L.E. Bruce[61], T.L. Bruckler[126], P.A. Bruckman de Renstrom[87], B. Brüers[48], A. Bruni[23b], G. Bruni[23b], M. Bruschi[23b], N. Bruscino[75a,75b], T. Buanes[16], Q. Buat[138], D. Buchin[110], A.G. Buckley[59], O. Bulekov[37], B.A. Bullard[143], S. Burdin[92], C.D. Burgard[49], A.M. Burger[40], B. Burghgrave[8], O. Burlayenko[54], J.T.P. Burr[32], C.D. Burton[11], J.C. Burzynski[142], E.L. Busch[41], V. Büscher[100], P.J. Bussey[59], J.M. Butler[25], C.M. Buttar[59], J.M. Butterworth[96], W. Buttinger[134], C.J. Buxo Vazquez[107], A.R. Buzykaev[37], S. Cabrera Urbán[163], L. Cadamuro[66], D. Caforio[58], H. Cai[129], Y. Cai[14a,14e], Y. Cai[14c], V.M.M. Cairo[36], O. Cakir[3a], N. Calace[36], P. Calafiura[17a], G. Calderini[127], P. Calfayan[68], G. Callea[59], L.P. Caloba[83b], D. Calvet[40], S. Calvet[40], T.P. Calvet[102], M. Calvetti[74a,74b], R. Camacho Toro[127], S. Camarda[36], D. Camarero Munoz[26], P. Camarri[76a,76b], M.T. Camerlingo[72a,72b], D. Cameron[36], C. Camincher[165], M. Campanelli[96], A. Camplani[42], V. Canale[72a,72b], A. Canesse[104], J. Cantero[163], Y. Cao[162], F. Capocasa[26], M. Capua[43b,43a], A. Carbone[71a,71b], R. Cardarelli[76a], J.C.J. Cardenas[8], F. Cardillo[163], G. Carducci[43b,43a], T. Carli[36], G. Carlino[72a], J.I. Carlotto[13], B.T. Carlson[129,q], E.M. Carlson[165,156a], L. Carminati[71a,71b], A. Carnelli[135], M. Carnesale[75a,75b], S. Caron[113], E. Carquin[137f], S. Carrá[71a], G. Carratta[23b,23a], F. Carrio Argos[33g], J.W.S. Carter[155], T.M. Carter[52], M.P. Casado[13,i], M. Caspar[48], E.G. Castiglia[172], F.L. Castillo[4], L. Castillo Garcia[13], V. Castillo Gimenez[163], N.F. Castro[130a,130e], A. Catinaccio[36], J.R. Catmore[125], V. Cavaliere[29], N. Cavalli[23b,23a], V. Cavasinni[74a,74b], Y.C. Cekmecelioglu[48], E. Celebi[21a], F. Celli[126], M.S. Centonze[70a,70b],

JHEP05(2024)162

V. Cepaitis[56], K. Cerny[122], A.S. Cerqueira[83a], A. Cerri[146], L. Cerrito[76a,76b], F. Cerutti[17a], B. Cervato[141], A. Cervelli[23b], G. Cesarini[53], S.A. Cetin[82], Z. Chadi[35a], D. Chakraborty[115], J. Chan[170], W.Y. Chan[153], J.D. Chapman[32], E. Chapon[135], B. Chargeishvili[149b], D.G. Charlton[20], T.P. Charman[94], M. Chatterjee[19], C. Chauhan[133], S. Chekanov[6], S.V. Chekulaev[156a], G.A. Chelkov[38,a], A. Chen[106], B. Chen[151], B. Chen[165], H. Chen[14c], H. Chen[29], J. Chen[62c], J. Chen[142], M. Chen[126], S. Chen[153], S.J. Chen[14c], X. Chen[62c,135], X. Chen[14b,af], Y. Chen[62a], C.L. Cheng[170], H.C. Cheng[64a], S. Cheong[143], A. Cheplakov[38], E. Cheremushkina[48], E. Cherepanova[114], R. Cherkaoui El Moursli[35e], E. Cheu[7], K. Cheung[65], L. Chevalier[135], V. Chiarella[53], G. Chiarelli[74a], N. Chiedde[102], G. Chiodini[70a], A.S. Chisholm[20], A. Chitan[27b], M. Chitishvili[163], M.V. Chizhov[38], K. Choi[11], A.R. Chomont[75a,75b], Y. Chou[103], E.Y.S. Chow[113], T. Chowdhury[33g], K.L. Chu[169], M.C. Chu[64a], X. Chu[14a,14e], J. Chudoba[131], J.J. Chwastowski[87], D. Cieri[110], K.M. Ciesla[86a], V. Cindro[93], A. Ciocio[17a], F. Cirotto[72a,72b], Z.H. Citron[169,k], M. Citterio[71a], D.A. Ciubotaru[27b], B.M. Ciungu[155], A. Clark[56], P.J. Clark[52], J.M. Clavijo Columbie[48], S.E. Clawson[48], C. Clement[47a,47b], J. Clercx[48], Y. Coadou[102], M. Cobal[69a,69c], A. Coccaro[57b], R.F. Coelho Barrue[130a], R. Coelho Lopes De Sa[103], S. Coelli[71a], H. Cohen[151], A.E.C. Coimbra[71a,71b], B. Cole[41], J. Collot[60], P. Conde Muiño[130a,130g], M.P. Connell[33c], S.H. Connell[33c], I.A. Connelly[59], E.I. Conroy[126], F. Conventi[72a,ah], H.G. Cooke[20], A.M. Cooper-Sarkar[126], A. Cordeiro Oudot Choi[127], L.D. Corpe[40], M. Corradi[75a,75b], F. Corriveau[104,w], A. Cortes-Gonzalez[18], M.J. Costa[163], F. Costanza[4], D. Costanzo[139], B.M. Cote[119], G. Cowan[95], K. Cranmer[170], D. Cremonini[23b,23a], S. Crépé-Renaudin[60], F. Crescioli[127], M. Cristinziani[141], M. Cristoforetti[78a,78b], V. Croft[114], J.E. Crosby[121], G. Crosetti[43b,43a], A. Cueto[99], T. Cuhadar Donszelmann[160], H. Cui[14a,14e], Z. Cui[7], W.R. Cunningham[59], F. Curcio[43b,43a], P. Czodrowski[36], M.M. Czurylo[63b], M.J. Da Cunha Sargedas De Sousa[57b,57a], J.V. Da Fonseca Pinto[83b], C. Da Via[101], W. Dabrowski[86a], T. Dado[49], S. Dahbi[33g], T. Dai[106], D. Dal Santo[19], C. Dallapiccola[103], M. Dam[42], G. D'amen[29], V. D'Amico[109], J. Damp[100], J.R. Dandoy[128], M.F. Daneri[30], M. Danninger[142], V. Dao[36], G. Darbo[57b], S. Darmora[6], S.J. Das[29,aj], S. D'Auria[71a,71b], C. David[156b], T. Davidek[133], B. Davis-Purcell[34], I. Dawson[94], H.A. Day-hall[132], K. De[8], R. De Asmundis[72a], N. De Biase[48], S. De Castro[23b,23a], N. De Groot[113], P. de Jong[114], H. De la Torre[115], A. De Maria[14c], A. De Salvo[75a], U. De Sanctis[76a,76b], A. De Santo[146], J.B. De Vivie De Regie[60], D.V. Dedovich[38], J. Degens[114], A.M. Deiana[44], F. Del Corso[23b,23a], J. Del Peso[99], F. Del Rio[63a], F. Deliot[135], C.M. Delitzsch[49], M. Della Pietra[72a,72b], D. Della Volpe[56], A. Dell'Acqua[36], L. Dell'Asta[71a,71b], M. Delmastro[4], P.A. Delsart[60], S. Demers[172], M. Demichev[38], S.P. Denisov[37], L. D'Eramo[40], D. Derendarz[87], F. Derue[127], P. Dervan[92], K. Desch[24], C. Deutsch[24], F.A. Di Bello[57b,57a], A. Di Ciaccio[76a,76b], L. Di Ciaccio[4], A. Di Domenico[75a,75b], C. Di Donato[72a,72b], A. Di Girolamo[36], G. Di Gregorio[36], A. Di Luca[78a,78b], B. Di Micco[77a,77b], R. Di Nardo[77a,77b], C. Diaconu[102], M. Diamantopoulou[34], F.A. Dias[114], T. Dias Do Vale[142], M.A. Diaz[137a,137b], F.G. Diaz Capriles[24], M. Didenko[163], E.B. Diehl[106], L. Diehl[54], S. Díez Cornell[48], C. Diez Pardos[141], C. Dimitriadi[161,24,161], A. Dimitrievska[17a], J. Dingfelder[24], I-M. Dinu[27b], S.J. Dittmeier[63b], F. Dittus[36],

F. Djama[102], T. Djobava[149b], J.I. Djuvsland[16], C. Doglioni[101,98], A. Dohnalova[28a], J. Dolejsi[133], Z. Dolezal[133], K.M. Dona[39], M. Donadelli[83c], B. Dong[107], J. Donini[40], A. D'Onofrio[77a,77b], M. D'Onofrio[92], J. Dopke[134], A. Doria[72a], N. Dos Santos Fernandes[130a], P. Dougan[101], M.T. Dova[90], A.T. Doyle[59], M.A. Draguet[126], E. Dreyer[169], I. Drivas-koulouris[10], M. Drnevich[117], A.S. Drobac[158], M. Drozdova[56], D. Du[62a], T.A. du Pree[114], F. Dubinin[37], M. Dubovsky[28a], E. Duchovni[169], G. Duckeck[109], O.A. Ducu[27b], D. Duda[52], A. Dudarev[36], E.R. Duden[26], M. D'uffizi[101], L. Duflot[66], M. Dührssen[36], C. Dülsen[171], A.E. Dumitriu[27b], M. Dunford[63a], S. Dungs[49], K. Dunne[47a,47b], A. Duperrin[102], H. Duran Yildiz[3a], M. Düren[58], A. Durglishvili[149b], B.L. Dwyer[115], G.I. Dyckes[17a], M. Dyndal[86a], B.S. Dziedzic[87], Z.O. Earnshaw[146], G.H. Eberwein[126], B. Eckerova[28a], S. Eggebrecht[55], E. Egidio Purcino De Souza[127], L.F. Ehrke[56], G. Eigen[16], K. Einsweiler[17a], T. Ekelof[161], P.A. Ekman[98], S. El Farkh[35b], Y. El Ghazali[35b], H. El Jarrari[35e,148], A. El Moussaouy[108], V. Ellajosyula[161], M. Ellert[161], F. Ellinghaus[171], N. Ellis[36], J. Elmsheuser[29], M. Elsing[36], D. Emeliyanov[134], Y. Enari[153], I. Ene[17a], S. Epari[13], J. Erdmann[49], P.A. Erland[87], M. Errenst[171], M. Escalier[66], C. Escobar[163], E. Etzion[151], G. Evans[130a], H. Evans[68], L.S. Evans[95], M.O. Evans[146], A. Ezhilov[37], S. Ezzarqtouni[35a], F. Fabbri[59], L. Fabbri[23b,23a], G. Facini[96], V. Fadeyev[136], R.M. Fakhrutdinov[37], S. Falciano[75a], L.F. Falda Ulhoa Coelho[36], P.J. Falke[24], J. Faltova[133], C. Fan[162], Y. Fan[14a], Y. Fang[14a,14e], M. Fanti[71a,71b], M. Faraj[69a,69b], Z. Farazpay[97], A. Farbin[8], A. Farilla[77a], T. Farooque[107], S.M. Farrington[52], F. Fassi[35e], D. Fassouliotis[9], M. Faucci Giannelli[76a,76b], W.J. Fawcett[32], L. Fayard[66], P. Federic[133], P. Federicova[131], O.L. Fedin[37,a], G. Fedotov[37], M. Feickert[170], L. Feligioni[102], D.E. Fellers[123], C. Feng[62b], M. Feng[14b], Z. Feng[114], M.J. Fenton[160], A.B. Fenyuk[37], L. Ferencz[48], R.A.M. Ferguson[91], S.I. Fernandez Luengo[137f], P. Fernandez Martinez[13], M.J.V. Fernoux[102], J. Ferrando[48], A. Ferrari[161], P. Ferrari[114,113], R. Ferrari[73a], D. Ferrere[56], C. Ferretti[106], F. Fiedler[100], P. Fiedler[132], A. Filipčič[93], E.K. Filmer[1], F. Filthaut[113], M.C.N. Fiolhais[130a,130c,c], L. Fiorini[163], W.C. Fisher[107], T. Fitschen[101], P.M. Fitzhugh[135], I. Fleck[141], P. Fleischmann[106], T. Flick[171], M. Flores[33d,ac], L.R. Flores Castillo[64a], L. Flores Sanz De Acedo[36], F.M. Follega[78a,78b], N. Fomin[16], J.H. Foo[155], B.C. Forland[68], A. Formica[135], A.C. Forti[101], E. Fortin[36], A.W. Fortman[61], M.G. Foti[17a], L. Fountas[9,j], D. Fournier[66], H. Fox[91], P. Francavilla[74a,74b], S. Francescato[61], S. Franchellucci[56], M. Franchini[23b,23a], S. Franchino[63a], D. Francis[36], L. Franco[113], V. Franco Lima[36], L. Franconi[48], M. Franklin[61], G. Frattari[26], A.C. Freegard[94], W.S. Freund[83b], Y.Y. Frid[151], J. Friend[59], N. Fritzsche[50], A. Froch[54], D. Froidevaux[36], J.A. Frost[126], Y. Fu[62a], M. Fujimoto[118,ad], E. Fullana Torregrosa[163,*], K.Y. Fung[64a], E. Furtado De Simas Filho[83b], M. Furukawa[153], J. Fuster[163], A. Gabrielli[23b,23a], A. Gabrielli[155], P. Gadow[36], G. Gagliardi[57b,57a], L.G. Gagnon[17a], E.J. Gallas[126], B.J. Gallop[134], K.K. Gan[119], S. Ganguly[153], Y. Gao[52], F.M. Garay Walls[137a,137b], B. Garcia[29], C. García[163], A. Garcia Alonso[114], A.G. Garcia Caffaro[172], J.E. García Navarro[163], M. Garcia-Sciveres[17a], G.L. Gardner[128], R.W. Gardner[39], N. Garelli[158], D. Garg[80], R.B. Garg[143,n], J.M. Gargan[52], C.A. Garner[155], C.M. Garvey[33a], P. Gaspar[83b], V.K. Gassmann[158], G. Gaudio[73a], V. Gautam[13], P. Gauzzi[75a,75b], I.L. Gavrilenko[37], A. Gavrilyuk[37], C. Gay[164], G. Gaycken[48],

JHEP05(2024)162

E.N. Gazis[10], A.A. Geanta[27b], C.M. Gee[136], C. Gemme[57b], M.H. Genest[60], S. Gentile[75a,75b], A.D. Gentry[112], S. George[95], W.F. George[20], T. Geralis[46], P. Gessinger-Befurt[36], M.E. Geyik[171], M. Ghani[167], M. Ghneimat[141], K. Ghorbanian[94], A. Ghosal[141], A. Ghosh[160], A. Ghosh[7], B. Giacobbe[23b], S. Giagu[75a,75b], T. Giani[114], P. Giannetti[74a], A. Giannini[62a], S.M. Gibson[95], M. Gignac[136], D.T. Gil[86b], A.K. Gilbert[86a], B.J. Gilbert[41], D. Gillberg[34], G. Gilles[114], N.E.K. Gillwald[48], L. Ginabat[127], D.M. Gingrich[2,ag], M.P. Giordani[69a,69c], P.F. Giraud[135], G. Giugliarelli[69a,69c], D. Giugni[71a], F. Giuli[36], I. Gkialas[9,j], L.K. Gladilin[37], C. Glasman[99], G.R. Gledhill[123], G. Glemža[48], M. Glisic[123], I. Gnesi[43b,f], Y. Go[29,aj], M. Goblirsch-Kolb[36], B. Gocke[49], D. Godin[108], B. Gokturk[21a], S. Goldfarb[105], T. Golling[56], M.G.D. Gololo[33g], D. Golubkov[37], J.P. Gombas[107], A. Gomes[130a,130b], G. Gomes Da Silva[141], A.J. Gomez Delegido[163], R. Gonçalo[130a,130c], G. Gonella[123], L. Gonella[20], A. Gongadze[149c], F. Gonnella[20], J.L. Gonski[41], R.Y. González Andana[52], S. González de la Hoz[163], S. Gonzalez Fernandez[13], R. Gonzalez Lopez[92], C. Gonzalez Renteria[17a], M.V. Gonzalez Rodrigues[48], R. Gonzalez Suarez[161], S. Gonzalez-Sevilla[56], G.R. Gonzalvo Rodriguez[163], L. Goossens[36], B. Gorini[36], E. Gorini[70a,70b], A. Gorišek[93], T.C. Gosart[128], A.T. Goshaw[51], M.I. Gostkin[38], S. Goswami[121], C.A. Gottardo[36], S.A. Gotz[109], M. Gouighri[35b], V. Goumarre[48], A.G. Goussiou[138], N. Govender[33c], I. Grabowska-Bold[86a], K. Graham[34], E. Gramstad[125], S. Grancagnolo[70a,70b], M. Grandi[146], C.M. Grant[1,135], P.M. Gravila[27f], F.G. Gravili[70a,70b], H.M. Gray[17a], M. Greco[70a,70b], C. Grefe[24], I.M. Gregor[48], P. Grenier[143], S.G. Grewe[110], C. Grieco[13], A.A. Grillo[136], K. Grimm[31], S. Grinstein[13,s], J.-F. Grivaz[66], E. Gross[169], J. Grosse-Knetter[55], C. Grud[106], J.C. Grundy[126], L. Guan[106], W. Guan[29], C. Gubbels[164], J.G.R. Guerrero Rojas[163], G. Guerrieri[69a,69c], F. Guescini[110], R. Gugel[100], J.A.M. Guhit[106], A. Guida[18], T. Guillemin[4], E. Guilloton[167,134], S. Guindon[36], F. Guo[14a,14e], J. Guo[62c], L. Guo[48], Y. Guo[106], R. Gupta[48], S. Gurbuz[24], S.S. Gurdasani[54], G. Gustavino[36], M. Guth[56], P. Gutierrez[120], L.F. Gutierrez Zagazeta[128], C. Gutschow[96], C. Gwenlan[126], C.B. Gwilliam[92], E.S. Haaland[125], A. Haas[117], M. Habedank[48], C. Haber[17a], H.K. Hadavand[8], A. Hadef[100], S. Hadzic[110], A.I. Hagan[91], J.J. Hahn[141], E.H. Haines[96], M. Haleem[166], J. Haley[121], J.J. Hall[139], G.D. Hallewell[102], L. Halser[19], K. Hamano[165], M. Hamer[24], G.N. Hamity[52], E.J. Hampshire[95], J. Han[62b], K. Han[62a], L. Han[14c], L. Han[62a], S. Han[17a], Y.F. Han[155], K. Hanagaki[84], M. Hance[136], D.A. Hangal[41,ab], H. Hanif[142], M.D. Hank[128], R. Hankache[101], J.B. Hansen[42], J.D. Hansen[42], P.H. Hansen[42], K. Hara[157], D. Harada[56], T. Harenberg[171], S. Harkusha[37], M.L. Harris[103], Y.T. Harris[126], J. Harrison[13], N.M. Harrison[119], P.F. Harrison[167], N.M. Hartman[110], N.M. Hartmann[109], Y. Hasegawa[140], R. Hauser[107], C.M. Hawkes[20], R.J. Hawkings[36], Y. Hayashi[153], S. Hayashida[111], D. Hayden[107], C. Hayes[106], R.L. Hayes[114], C.P. Hays[126], J.M. Hays[94], H.S. Hayward[92], F. He[62a], M. He[14a,14e], Y. He[154], Y. He[48], N.B. Heatley[94], V. Hedberg[98], A.L. Heggelund[125], N.D. Hehir[94,*], C. Heidegger[54], K.K. Heidegger[54], W.D. Heidorn[81], J. Heilman[34], S. Heim[48], T. Heim[17a], J.G. Heinlein[128], J.J. Heinrich[123], L. Heinrich[110,ae], J. Hejbal[131], L. Helary[48], A. Held[170], S. Hellesund[16], C.M. Helling[164], S. Hellman[47a,47b], R.C.W. Henderson[91], L. Henkelmann[32], A.M. Henriques Correia[36],

H. Herde[98], Y. Hernández Jiménez[145], L.M. Herrmann[24], T. Herrmann[50], G. Herten[54], R. Hertenberger[109], L. Hervas[36], M.E. Hesping[100], N.P. Hessey[156a], H. Hibi[85], E. Hill[155], S.J. Hillier[20], J.R. Hinds[107], F. Hinterkeuser[24], M. Hirose[124], S. Hirose[157], D. Hirschbuehl[171], T.G. Hitchings[101], B. Hiti[93], J. Hobbs[145], R. Hobincu[27e], N. Hod[169], M.C. Hodgkinson[139], B.H. Hodkinson[32], A. Hoecker[36], J. Hofer[48], T. Holm[24], M. Holzbock[110], L.B.A.H. Hommels[32], B.P. Honan[101], J. Hong[62c], T.M. Hong[129], B.H. Hooberman[162], W.H. Hopkins[6], Y. Horii[111], S. Hou[148], A.S. Howard[93], J. Howarth[59], J. Hoya[6], M. Hrabovsky[122], A. Hrynevich[48], T. Hryn'ova[4], P.J. Hsu[65], S.-C. Hsu[138], Q. Hu[62a], Y.F. Hu[14a,14e], S. Huang[64b], X. Huang[14c], X. Huang[14a,14e], Y. Huang[139], Y. Huang[14a], Z. Huang[101], Z. Hubacek[132], M. Huebner[24], F. Huegging[24], T.B. Huffman[126], C.A. Hugli[48], M. Huhtinen[36], S.K. Huiberts[16], R. Hulsken[104], N. Huseynov[12], J. Huston[107], J. Huth[61], R. Hyneman[143], G. Iacobucci[56], G. Iakovidis[29], I. Ibragimov[141], L. Iconomidou-Fayard[66], P. Iengo[72a,72b], R. Iguchi[153], T. Iizawa[126], Y. Ikegami[84], N. Ilic[155], H. Imam[35a], M. Ince Lezki[56], T. Ingebretsen Carlson[47a,47b], G. Introzzi[73a,73b], M. Iodice[77a], V. Ippolito[75a,75b], R.K. Irwin[92], M. Ishino[153], W. Islam[170], C. Issever[18,48], S. Istin[21a,al], H. Ito[168], J.M. Iturbe Ponce[64a], R. Iuppa[78a,78b], A. Ivina[169], J.M. Izen[45], V. Izzo[72a], P. Jacka[131,132], P. Jackson[1], R.M. Jacobs[48], B.P. Jaeger[142], C.S. Jagfeld[109], G. Jain[156a], P. Jain[54], K. Jakobs[54], T. Jakoubek[169], J. Jamieson[59], K.W. Janas[86a], M. Javurkova[103], F. Jeanneau[135], L. Jeanty[123], J. Jejelava[149a,z], P. Jenni[54,g], C.E. Jessiman[34], S. Jézéquel[4], C. Jia[62b], J. Jia[145], X. Jia[61], X. Jia[14a,14e], Z. Jia[14c], S. Jiggins[48], J. Jimenez Pena[13], S. Jin[14c], A. Jinaru[27b], O. Jinnouchi[154], P. Johansson[139], K.A. Johns[7], J.W. Johnson[136], D.M. Jones[32], E. Jones[48], P. Jones[32], R.W.L. Jones[91], T.J. Jones[92], H.L. Joos[55,36], R. Joshi[119], J. Jovicevic[15], X. Ju[17a], J.J. Junggeburth[103], T. Junkermann[63a], A. Juste Rozas[13,s], M.K. Juzek[87], S. Kabana[137e], A. Kaczmarska[87], M. Kado[110], H. Kagan[119], M. Kagan[143], A. Kahn[41], A. Kahn[128], C. Kahra[100], T. Kaji[153], E. Kajomovitz[150], N. Kakati[169], I. Kalaitzidou[54], C.W. Kalderon[29], A. Kamenshchikov[155], N.J. Kang[136], D. Kar[33g], K. Karava[126], M.J. Kareem[156b], E. Karentzos[54], I. Karkanias[152], O. Karkout[114], S.N. Karpov[38], Z.M. Karpova[38], V. Kartvelishvili[91], A.N. Karyukhin[37], E. Kasimi[152], J. Katzy[48], S. Kaur[34], K. Kawade[140], M.P. Kawale[120], C. Kawamoto[88], T. Kawamoto[135], E.F. Kay[36], F.I. Kaya[158], S. Kazakos[107], V.F. Kazanin[37], Y. Ke[145], J.M. Keaveney[33a], R. Keeler[165], G.V. Kehris[61], J.S. Keller[34], A.S. Kelly[96], J.J. Kempster[146], K.E. Kennedy[41], P.D. Kennedy[100], O. Kepka[131], B.P. Kerridge[167], S. Kersten[171], B.P. Kerševan[93], S. Keshri[66], L. Keszeghova[28a], S. Ketabchi Haghighat[155], M. Khandoga[127], A. Khanov[121], A.G. Kharlamov[37], T. Kharlamova[37], E.E. Khoda[138], M. Kholodenko[37], T.J. Khoo[18], G. Khoriauli[166], J. Khubua[149b], Y.A.R. Khwaira[66], A. Kilgallon[123], D.W. Kim[47a,47b], Y.K. Kim[39], N. Kimura[96], M.K. Kingston[55], A. Kirchhoff[55], C. Kirfel[24], F. Kirfel[24], J. Kirk[134], A.E. Kiryunin[110], C. Kitsaki[10], O. Kivernyk[24], M. Klassen[63a], C. Klein[34], L. Klein[166], M.H. Klein[106], M. Klein[92], S.B. Klein[56], U. Klein[92], P. Klimek[36], A. Klimentov[29], T. Klioutchnikova[36], P. Kluit[114], S. Kluth[110], E. Kneringer[79], T.M. Knight[155], A. Knue[49], R. Kobayashi[88], D. Kobylianskii[169], S.F. Koch[126], M. Kocian[143], P. Kodyš[133], D.M. Koeck[123], P.T. Koenig[24], T. Koffas[34], M. Kolb[135], I. Koletsou[4], T. Komarek[122],

K. Köneke[54], A.X.Y. Kong[1], T. Kono[118], N. Konstantinidis[96], P. Kontaxakis[56], B. Konya[98], R. Kopeliansky[68], S. Koperny[86a], K. Korcyl[87], K. Kordas[152,e], G. Koren[151], A. Korn[96], S. Korn[55], I. Korolkov[13], N. Korotkova[37], B. Kortman[114], O. Kortner[110], S. Kortner[110], W.H. Kostecka[115], V.V. Kostyukhin[141], A. Kotsokechagia[135], A. Kotwal[51], A. Koulouris[36], A. Kourkoumeli-Charalampidi[73a,73b], C. Kourkoumelis[9], E. Kourlitis[110,ae], O. Kovanda[146], R. Kowalewski[165], W. Kozanecki[135], A.S. Kozhin[37], V.A. Kramarenko[37], G. Kramberger[93], P. Kramer[100], M.W. Krasny[127], A. Krasznahorkay[36], J.W. Kraus[171], J.A. Kremer[48], T. Kresse[50], J. Kretzschmar[92], K. Kreul[18], P. Krieger[155], S. Krishnamurthy[103], M. Krivos[133], K. Krizka[20], K. Kroeninger[49], H. Kroha[110], J. Kroll[131], J. Kroll[128], K.S. Krowpman[107], U. Kruchonak[38], H. Krüger[24], N. Krumnack[81], M.C. Kruse[51], J.A. Krzysiak[87], O. Kuchinskaia[37], S. Kuday[3a], S. Kuehn[36], R. Kuesters[54], T. Kuhl[48], V. Kukhtin[38], Y. Kulchitsky[37,a], S. Kuleshov[137d,137b], M. Kumar[33g], N. Kumari[48], A. Kupco[131], T. Kupfer[49], A. Kupich[37], O. Kuprash[54], H. Kurashige[85], L.L. Kurchaninov[156a], O. Kurdysh[66], Y.A. Kurochkin[37], A. Kurova[37], M. Kuze[154], A.K. Kvam[103], J. Kvita[122], T. Kwan[104], N.G. Kyriacou[106], L.A.O. Laatu[102], C. Lacasta[163], F. Lacava[75a,75b], H. Lacker[18], D. Lacour[127], N.N. Lad[96], E. Ladygin[38], B. Laforge[127], T. Lagouri[137e], F.Z. Lahbabi[35a], S. Lai[55], I.K. Lakomiec[86a], N. Lalloue[60], J.E. Lambert[165], S. Lammers[68], W. Lampl[7], C. Lampoudis[152,e], A.N. Lancaster[115], E. Lançon[29], U. Landgraf[54], M.P.J. Landon[94], V.S. Lang[54], R.J. Langenberg[103], O.K.B. Langrekken[125], A.J. Lankford[160], F. Lanni[36], K. Lantzsch[24], A. Lanza[73a], A. Lapertosa[57b,57a], J.F. Laporte[135], T. Lari[71a], F. Lasagni Manghi[23b], M. Lassnig[36], V. Latonova[131], A. Laudrain[100], A. Laurier[150], S.D. Lawlor[139], Z. Lawrence[101], M. Lazzaroni[71a,71b], B. Le[101], E.M. Le Boulicaut[51], B. Leban[93], A. Lebedev[81], M. LeBlanc[101], F. Ledroit-Guillon[60], A.C.A. Lee[96], S.C. Lee[148], S. Lee[47a,47b], T.F. Lee[92], L.L. Leeuw[33c], H.P. Lefebvre[95], M. Lefebvre[165], C. Leggett[17a], G. Lehmann Miotto[36], M. Leigh[56], W.A. Leight[103], W. Leinonen[113], A. Leisos[152,r], M.A.L. Leite[83c], C.E. Leitgeb[48], R. Leitner[133], K.J.C. Leney[44], T. Lenz[24], S. Leone[74a], C. Leonidopoulos[52], A. Leopold[144], C. Leroy[108], R. Les[107], C.G. Lester[32], M. Levchenko[37], J. Levêque[4], D. Levin[106], L.J. Levinson[169], M.P. Lewicki[87], D.J. Lewis[4], A. Li[5], B. Li[62b], C. Li[62a], C-Q. Li[62c], H. Li[62a], H. Li[62b], H. Li[14c], H. Li[14b], H. Li[62b], K. Li[138], L. Li[62c], M. Li[14a,14e], Q.Y. Li[62a], S. Li[14a,14e], S. Li[62d,62c,d], T. Li[5], X. Li[104], Z. Li[126], Z. Li[104], Z. Li[92], Z. Li[14a,14e], S. Liang[14a,14e], Z. Liang[14a], M. Liberatore[135], B. Liberti[76a], K. Lie[64c], J. Lieber Marin[83b], H. Lien[68], K. Lin[107], R.E. Lindley[7], J.H. Lindon[2], E. Lipeles[128], A. Lipniacka[16], A. Lister[164], J.D. Little[4], B. Liu[14a], B.X. Liu[142], D. Liu[62d,62c], J.B. Liu[62a], J.K.K. Liu[32], K. Liu[62d,62c], M. Liu[62a], M.Y. Liu[62a], P. Liu[14a], Q. Liu[62d,138,62c], X. Liu[62a], Y. Liu[14d,14e], Y.L. Liu[62b], Y.W. Liu[62a], J. Llorente Merino[142], S.L. Lloyd[94], E.M. Lobodzinska[48], P. Loch[7], S. Loffredo[76a,76b], T. Lohse[18], K. Lohwasser[139], E. Loiacono[48], M. Lokajicek[131,*], J.D. Lomas[20], J.D. Long[162], I. Longarini[160], L. Longo[70a,70b], R. Longo[162], I. Lopez Paz[67], A. Lopez Solis[48], J. Lorenz[109], N. Lorenzo Martinez[4], A.M. Lory[109], G. Löschcke Centeno[146], O. Loseva[37], X. Lou[47a,47b], X. Lou[14a,14e], A. Lounis[66], J. Love[6], P.A. Love[91], G. Lu[14a,14e], M. Lu[80], S. Lu[128], Y.J. Lu[65], H.J. Lubatti[138], C. Luci[75a,75b], F.L. Lucio Alves[14c], A. Lucotte[60],

F. Luehring[68], I. Luise[145], O. Lukianchuk[66], O. Lundberg[144], B. Lund-Jensen[144], N.A. Luongo[123], M.S. Lutz[151], A.B. Lux[25], D. Lynn[29], H. Lyons[92], R. Lysak[131], E. Lytken[98], V. Lyubushkin[38], T. Lyubushkina[38], M.M. Lyukova[145], H. Ma[29], K. Ma[62a], L.L. Ma[62b], Y. Ma[121], D.M. Mac Donell[165], G. Maccarrone[53], J.C. MacDonald[100], P.C. Machado De Abreu Farias[83b], R. Madar[40], W.F. Mader[50], T. Madula[96], J. Maeda[85], T. Maeno[29], H. Maguire[139], V. Maiboroda[135], A. Maio[130a,130b,130d], K. Maj[86a], O. Majersky[48], S. Majewski[123], N. Makovec[66], V. Maksimovic[15], B. Malaescu[127], Pa. Malecki[87], V.P. Maleev[37], F. Malek[60], M. Mali[93], D. Malito[95], U. Mallik[80], S. Maltezos[10], S. Malyukov[38], J. Mamuzic[13], G. Mancini[53], G. Manco[73a,73b], J.P. Mandalia[94], I. Mandić[93], L. Manhaes de Andrade Filho[83a], I.M. Maniatis[169], J. Manjarres Ramos[102,aa], D.C. Mankad[169], A. Mann[109], B. Mansoulie[135], S. Manzoni[36], X. Mapekula[33c], A. Marantis[152,r], G. Marchiori[5], M. Marcisovsky[131], C. Marcon[71a], M. Marinescu[20], M. Marjanovic[120], E.J. Marshall[91], Z. Marshall[17a], S. Marti-Garcia[163], T.A. Martin[167], V.J. Martin[52], B. Martin dit Latour[16], L. Martinelli[75a,75b], M. Martinez[13,s], P. Martinez Agullo[163], V.I. Martinez Outschoorn[103], P. Martinez Suarez[13], S. Martin-Haugh[134], V.S. Martoiu[27b], A.C. Martyniuk[96], A. Marzin[36], D. Mascione[78a,78b], L. Masetti[100], T. Mashimo[153], J. Masik[101], A.L. Maslennikov[37], L. Massa[23b], P. Massarotti[72a,72b], P. Mastrandrea[74a,74b], A. Mastroberardino[43b,43a], T. Masubuchi[153], T. Mathisen[161], J. Matousek[133], N. Matsuzawa[153], J. Maurer[27b], B. Maček[93], D.A. Maximov[37], R. Mazini[148], I. Maznas[152], M. Mazza[107], S.M. Mazza[136], E. Mazzeo[71a,71b], C. Mc Ginn[29], J.P. Mc Gowan[104], S.P. Mc Kee[106], E.F. McDonald[105], A.E. McDougall[114], J.A. Mcfayden[146], R.P. McGovern[128], G. Mchedlidze[149b], R.P. Mckenzie[33g], T.C. Mclachlan[48], D.J. Mclaughlin[96], S.J. McMahon[134], C.M. Mcpartland[92], R.A. McPherson[165,w], S. Mehlhase[109], A. Mehta[92], D. Melini[150], B.R. Mellado Garcia[33g], A.H. Melo[55], F. Meloni[48], A.M. Mendes Jacques Da Costa[101], H.Y. Meng[155], L. Meng[91], S. Menke[110], M. Mentink[36], E. Meoni[43b,43a], C. Merlassino[126], L. Merola[72a,72b], C. Meroni[71a,71b], G. Merz[106], O. Meshkov[37], J. Metcalfe[6], A.S. Mete[6], C. Meyer[68], J-P. Meyer[135], R.P. Middleton[134], L. Mijović[52], G. Mikenberg[169], M. Mikestikova[131], M. Mikuž[93], H. Mildner[100], A. Milic[36], C.D. Milke[44], D.W. Miller[39], L.S. Miller[34], A. Milov[169], D.A. Milstead[47a,47b], T. Min[14c], A.A. Minaenko[37], I.A. Minashvili[149b], L. Mince[59], A.I. Mincer[117], B. Mindur[86a], M. Mineev[38], Y. Mino[88], L.M. Mir[13], M. Miralles Lopez[163], M. Mironova[17a], A. Mishima[153], M.C. Missio[113], A. Mitra[167], V.A. Mitsou[163], Y. Mitsumori[111], O. Miu[155], P.S. Miyagawa[94], T. Mkrtchyan[63a], M. Mlinarevic[96], T. Mlinarevic[96], M. Mlynarikova[36], S. Mobius[19], P. Moder[48], P. Mogg[109], A.F. Mohammed[14a,14e], S. Mohapatra[41], G. Mokgatitswane[33g], L. Moleri[169], B. Mondal[141], S. Mondal[132], K. Mönig[48], E. Monnier[102], L. Monsonis Romero[163], J. Montejo Berlingen[13], M. Montella[119], F. Montereali[77a,77b], F. Monticelli[90], S. Monzani[69a,69c], N. Morange[66], A.L. Moreira De Carvalho[130a], M. Moreno Llácer[163], C. Moreno Martinez[56], P. Morettini[57b], S. Morgenstern[36], M. Morii[61], M. Morinaga[153], A.K. Morley[36], F. Morodei[75a,75b], L. Morvaj[36], P. Moschovakos[36], B. Moser[36], M. Mosidze[149b], T. Moskalets[54], P. Moskvitina[113], J. Moss[31,l], E.J.W. Moyse[103], O. Mtintsilana[33g], S. Muanza[102], J. Mueller[129], D. Muenstermann[91], R. Müller[19], G.A. Mullier[161], A.J. Mullin[32],

JHEP05(2024)162

J.J. Mullin[128], D.P. Mungo[155], D. Munoz Perez[163], F.J. Munoz Sanchez[101], M. Murin[101], W.J. Murray[167,134], A. Murrone[71a,71b], M. Muškinja[17a], C. Mwewa[29], A.G. Myagkov[37,a], A.J. Myers[8], G. Myers[68], M. Myska[132], B.P. Nachman[17a], O. Nackenhorst[49], A. Nag[50], K. Nagai[126], K. Nagano[84], J.L. Nagle[29,aj], E. Nagy[102], A.M. Nairz[36], Y. Nakahama[84], K. Nakamura[84], K. Nakkalil[5], H. Nanjo[124], R. Narayan[44], E.A. Narayanan[112], I. Naryshkin[37], M. Naseri[34], S. Nasri[159], C. Nass[24], G. Navarro[22a], J. Navarro-Gonzalez[163], R. Nayak[151], A. Nayaz[18], P.Y. Nechaeva[37], F. Nechansky[48], L. Nedic[126], T.J. Neep[20], A. Negri[73a,73b], M. Negrini[23b], C. Nellist[114], C. Nelson[104], K. Nelson[106], S. Nemecek[131], M. Nessi[36,h], M.S. Neubauer[162], F. Neuhaus[100], J. Neundorf[48], R. Newhouse[164], P.R. Newman[20], C.W. Ng[129], Y.W.Y. Ng[48], B. Ngair[35e], H.D.N. Nguyen[108], R.B. Nickerson[126], R. Nicolaidou[135], J. Nielsen[136], M. Niemeyer[55], J. Niermann[55,36], N. Nikiforou[36], V. Nikolaenko[37,a], I. Nikolic-Audit[127], K. Nikolopoulos[20], P. Nilsson[29], I. Ninca[48], H.R. Nindhito[56], G. Ninio[151], A. Nisati[75a], N. Nishu[2], R. Nisius[110], J-E. Nitschke[50], E.K. Nkadimeng[33g], T. Nobe[153], D.L. Noel[32], T. Nommensen[147], M.B. Norfolk[139], R.R.B. Norisam[96], B.J. Norman[34], J. Novak[93], T. Novak[48], L. Novotny[132], R. Novotny[112], L. Nozka[122], K. Ntekas[160], N.M.J. Nunes De Moura Junior[83b], E. Nurse[96], J. Ocariz[127], A. Ochi[85], I. Ochoa[130a], S. Oerdek[48,t], J.T. Offermann[39], A. Ogrodnik[133], A. Oh[101], C.C. Ohm[144], H. Oide[84], R. Oishi[153], M.L. Ojeda[48], M.W. O'Keefe[92], Y. Okumura[153], L.F. Oleiro Seabra[130a], S.A. Olivares Pino[137d], D. Oliveira Damazio[29], D. Oliveira Goncalves[83a], J.L. Oliver[160], Ö.O. Öncel[54], A.P. O'Neill[19], A. Onofre[130a,130e], P.U.E. Onyisi[11], M.J. Oreglia[39], G.E. Orellana[90], D. Orestano[77a,77b], N. Orlando[13], R.S. Orr[155], V. O'Shea[59], L.M. Osojnak[128], R. Ospanov[62a], G. Otero y Garzon[30], H. Otono[89], P.S. Ott[63a], G.J. Ottino[17a], M. Ouchrif[35d], J. Ouellette[29], F. Ould-Saada[125], M. Owen[59], R.E. Owen[134], K.Y. Oyulmaz[21a], V.E. Ozcan[21a], F. Ozturk[87], N. Ozturk[8], S. Ozturk[82], H.A. Pacey[126], A. Pacheco Pages[13], C. Padilla Aranda[13], G. Padovano[75a,75b], S. Pagan Griso[17a], G. Palacino[68], A. Palazzo[70a,70b], S. Palestini[36], J. Pan[172], T. Pan[64a], D.K. Panchal[11], C.E. Pandini[114], J.G. Panduro Vazquez[95], H.D. Pandya[1], H. Pang[14b], P. Pani[48], G. Panizzo[69a,69c], L. Paolozzi[56], C. Papadatos[108], S. Parajuli[44], A. Paramonov[6], C. Paraskevopoulos[10], D. Paredes Hernandez[64b], K.R. Park[41], T.H. Park[155], M.A. Parker[32], F. Parodi[57b,57a], E.W. Parrish[115], V.A. Parrish[52], J.A. Parsons[41], U. Parzefall[54], B. Pascual Dias[108], L. Pascual Dominguez[151], E. Pasqualucci[75a], S. Passaggio[57b], F. Pastore[95], P. Pasuwan[47a,47b], P. Patel[87], U.M. Patel[51], J.R. Pater[101], T. Pauly[36], J. Pearkes[143], M. Pedersen[125], R. Pedro[130a], S.V. Peleganchuk[37], O. Penc[36], E.A. Pender[52], K.E. Penski[109], M. Penzin[37], B.S. Peralva[83d], A.P. Pereira Peixoto[60], L. Pereira Sanchez[47a,47b], D.V. Perepelitsa[29,aj], E. Perez Codina[156a], M. Perganti[10], L. Perini[71a,71b,*], H. Pernegger[36], O. Perrin[40], K. Peters[48], R.F.Y. Peters[101], B.A. Petersen[36], T.C. Petersen[42], E. Petit[102], V. Petousis[132], C. Petridou[152,e], A. Petrukhin[141], M. Pettee[17a], N.E. Pettersson[36], A. Petukhov[37], K. Petukhova[133], R. Pezoa[137f], L. Pezzotti[36], G. Pezzullo[172], T.M. Pham[170], T. Pham[105], P.W. Phillips[134], G. Piacquadio[145], E. Pianori[17a], F. Piazza[123], R. Piegaia[30], D. Pietreanu[27b], A.D. Pilkington[101], M. Pinamonti[69a,69c], J.L. Pinfold[2], B.C. Pinheiro Pereira[130a], A.E. Pinto Pinoargote[100,135], L. Pintucci[69a,69c],

JHEP05(2024)162

K.M. Piper[146], A. Pirttikoski[56], D.A. Pizzi[34], L. Pizzimento[64b], A. Pizzini[114], M.-A. Pleier[29], V. Plesanovs[54], V. Pleskot[133], E. Plotnikova[38], G. Poddar[4], R. Poettgen[98], L. Poggioli[127], I. Pokharel[55], S. Polacek[133], G. Polesello[73a], A. Poley[142,156a], R. Polifka[132], A. Polini[23b], C.S. Pollard[167], Z.B. Pollock[119], V. Polychronakos[29], E. Pompa Pacchi[75a,75b], D. Ponomarenko[113], L. Pontecorvo[36], S. Popa[27a], G.A. Popeneciu[27d], A. Poreba[36], D.M. Portillo Quintero[156a], S. Pospisil[132], M.A. Postill[139], P. Postolache[27c], K. Potamianos[167], P.A. Potepa[86a], I.N. Potrap[38], C.J. Potter[32], H. Potti[1], T. Poulsen[48], J. Poveda[163], M.E. Pozo Astigarraga[36], A. Prades Ibanez[163], J. Pretel[54], D. Price[101], M. Primavera[70a], M.A. Principe Martin[99], R. Privara[122], T. Procter[59], M.L. Proffitt[138], N. Proklova[128], K. Prokofiev[64c], G. Proto[110], S. Protopopescu[29], J. Proudfoot[6], M. Przybycien[86a], W.W. Przygoda[86b], J.E. Puddefoot[139], D. Pudzha[37], D. Pyatiizbyantseva[37], J. Qian[106], D. Qichen[101], Y. Qin[101], T. Qiu[52], A. Quadt[55], M. Queitsch-Maitland[101], G. Quetant[56], R.P. Quinn[164], G. Rabanal Bolanos[61], D. Rafanoharana[54], F. Ragusa[71a,71b], J.L. Rainbolt[39], J.A. Raine[56], S. Rajagopalan[29], E. Ramakoti[37], K. Ran[48,14e], N.P. Rapheeha[33g], H. Rasheed[27b], V. Raskina[127], D.F. Rassloff[63a], S. Rave[100], B. Ravina[55], I. Ravinovich[169], M. Raymond[36], A.L. Read[125], N.P. Readioff[139], D.M. Rebuzzi[73a,73b], G. Redlinger[29], A.S. Reed[110], K. Reeves[26], J.A. Reidelsturz[171], D. Reikher[151], A. Rej[49], C. Rembser[36], A. Renardi[48], M. Renda[27b], M.B. Rendel[110], F. Renner[48], A.G. Rennie[160], A.L. Rescia[48], S. Resconi[71a], M. Ressegotti[57b,57a], S. Rettie[36], J.G. Reyes Rivera[107], E. Reynolds[17a], O.L. Rezanova[37], P. Reznicek[133], N. Ribaric[91], E. Ricci[78a,78b], R. Richter[110], S. Richter[47a,47b], E. Richter-Was[86b], M. Ridel[127], S. Ridouani[35d], P. Rieck[117], P. Riedler[36], E.M. Riefel[47a,47b], J.O. Rieger[114], M. Rijssenbeek[145], A. Rimoldi[73a,73b], M. Rimoldi[36], L. Rinaldi[23b,23a], T.T. Rinn[29], M.P. Rinnagel[109], G. Ripellino[161], I. Riu[13], P. Rivadeneira[48], J.C. Rivera Vergara[165], F. Rizatdinova[121], E. Rizvi[94], B.A. Roberts[167], B.R. Roberts[17a], S.H. Robertson[104,w], D. Robinson[32], C.M. Robles Gajardo[137f], M. Robles Manzano[100], A. Robson[59], A. Rocchi[76a,76b], C. Roda[74a,74b], S. Rodriguez Bosca[63a], Y. Rodriguez Garcia[22a], A. Rodriguez Rodriguez[54], A.M. Rodríguez Vera[156b], S. Roe[36], J.T. Roemer[160], A.R. Roepe-Gier[136], J. Roggel[171], O. Røhne[125], R.A. Rojas[103], C.P.A. Roland[127], J. Roloff[29], A. Romaniouk[37], E. Romano[73a,73b], M. Romano[23b], A.C. Romero Hernandez[162], N. Rompotis[92], L. Roos[127], S. Rosati[75a], B.J. Rosser[39], E. Rossi[126], E. Rossi[72a,72b], L.P. Rossi[57b], L. Rossini[54], R. Rosten[119], M. Rotaru[27b], B. Rottler[54], C. Rougier[102,aa], D. Rousseau[66], D. Rousso[32], A. Roy[162], S. Roy-Garand[155], A. Rozanov[102], Y. Rozen[150], X. Ruan[33g], A. Rubio Jimenez[163], A.J. Ruby[92], V.H. Ruelas Rivera[18], T.A. Ruggeri[1], A. Ruggiero[126], A. Ruiz-Martinez[163], A. Rummler[36], Z. Rurikova[54], N.A. Rusakovich[38], H.L. Russell[165], G. Russo[75a,75b], J.P. Rutherfoord[7], S. Rutherford Colmenares[32], E.M. Rüttinger[139], K. Rybacki[91], M. Rybar[133], E.B. Rye[125], A. Ryzhov[44], J.A. Sabater Iglesias[56], P. Sabatini[163], L. Sabetta[75a,75b], H.F-W. Sadrozinski[136], F. Safai Tehrani[75a], B. Safarzadeh Samani[134], M. Safdari[143], S. Saha[165], M. Sahinsoy[110], M. Saimpert[135], M. Saito[153], T. Saito[153], D. Salamani[36], A. Salnikov[143], J. Salt[163], A. Salvador Salas[151], D. Salvatore[43b,43a], F. Salvatore[146], A. Salzburger[36], D. Sammel[54], D. Sampsonidis[152,e], D. Sampsonidou[123], J. Sánchez[163], A. Sanchez Pineda[4], V. Sanchez Sebastian[163],

JHEP05(2024)162

H. Sandaker[125], C.O. Sander[48], J.A. Sandesara[103], M. Sandhoff[171], C. Sandoval[22b], D.P.C. Sankey[134], T. Sano[88], A. Sansoni[53], L. Santi[75a,75b], C. Santoni[40], H. Santos[130a,130b], S.N. Santpur[17a], A. Santra[169], K.A. Saoucha[116b], J.G. Saraiva[130a,130d], J. Sardain[7], O. Sasaki[84], K. Sato[157], C. Sauer[63b], F. Sauerburger[54], E. Sauvan[4], P. Savard[155,ag], R. Sawada[153], C. Sawyer[134], L. Sawyer[97], I. Sayago Galvan[163], C. Sbarra[23b], A. Sbrizzi[23b,23a], T. Scanlon[96], J. Schaarschmidt[138], P. Schacht[110], U. Schäfer[100], A.C. Schaffer[66,44], D. Schaile[109], R.D. Schamberger[145], C. Scharf[18], M.M. Schefer[19], V.A. Schegelsky[37], D. Scheirich[133], F. Schenck[18], M. Schernau[160], C. Scheulen[55], C. Schiavi[57b,57a], E.J. Schioppa[70a,70b], M. Schioppa[43b,43a], B. Schlag[143,n], K.E. Schleicher[54], S. Schlenker[36], J. Schmeing[171], M.A. Schmidt[171], K. Schmieden[100], C. Schmitt[100], S. Schmitt[48], L. Schoeffel[135], A. Schoening[63b], P.G. Scholer[54], E. Schopf[126], M. Schott[100], J. Schovancova[36], S. Schramm[56], F. Schroeder[171], T. Schroer[56], H-C. Schultz-Coulon[63a], M. Schumacher[54], B.A. Schumm[136], Ph. Schune[135], A.J. Schuy[138], H.R. Schwartz[136], A. Schwartzman[143], T.A. Schwarz[106], Ph. Schwemling[135], R. Schwienhorst[107], A. Sciandra[136], G. Sciolla[26], F. Scuri[74a], C.D. Sebastiani[92], K. Sedlaczek[115], P. Seema[18], S.C. Seidel[112], A. Seiden[136], B.D. Seidlitz[41], C. Seitz[48], J.M. Seixas[83b], G. Sekhniaidze[72a], S.J. Sekula[44], L. Selem[60], N. Semprini-Cesari[23b,23a], D. Sengupta[56], V. Senthilkumar[163], L. Serin[66], L. Serkin[69a,69b], M. Sessa[76a,76b], H. Severini[120], F. Sforza[57b,57a], A. Sfyrla[56], E. Shabalina[55], R. Shaheen[144], J.D. Shahinian[128], D. Shaked Renous[169], L.Y. Shan[14a], M. Shapiro[17a], A. Sharma[36], A.S. Sharma[164], P. Sharma[80], S. Sharma[48], P.B. Shatalov[37], K. Shaw[146], S.M. Shaw[101], A. Shcherbakova[37], Q. Shen[62c,5], P. Sherwood[96], L. Shi[96], X. Shi[14a], C.O. Shimmin[172], J.D. Shinner[95], I.P.J. Shipsey[126], S. Shirabe[56,h], M. Shiyakova[38,u], J. Shlomi[169], M.J. Shochet[39], J. Shojaii[105], D.R. Shope[125], B. Shrestha[120], S. Shrestha[119,ak], E.M. Shrif[33g], M.J. Shroff[165], P. Sicho[131], A.M. Sickles[162], E. Sideras Haddad[33g], A. Sidoti[23b], F. Siegert[50], Dj. Sijacki[15], R. Sikora[86a], F. Sili[90], J.M. Silva[20], M.V. Silva Oliveira[29], S.B. Silverstein[47a], S. Simion[66], R. Simoniello[36], E.L. Simpson[59], H. Simpson[146], L.R. Simpson[106], N.D. Simpson[98], S. Simsek[82], S. Sindhu[55], P. Sinervo[155], S. Singh[155], S. Sinha[48], S. Sinha[101], M. Sioli[23b,23a], I. Siral[36], E. Sitnikova[48], S.Yu. Sivoklokov[37,*], J. Sjölin[47a,47b], A. Skaf[55], E. Skorda[20], P. Skubic[120], M. Slawinska[87], V. Smakhtin[169], B.H. Smart[134], J. Smiesko[36], S.Yu. Smirnov[37], Y. Smirnov[37], L.N. Smirnova[37,a], O. Smirnova[98], A.C. Smith[41], E.A. Smith[39], H.A. Smith[126], J.L. Smith[92], R. Smith[143], M. Smizanska[91], K. Smolek[132], A.A. Snesarev[37], S.R. Snider[155], H.L. Snoek[114], S. Snyder[29], R. Sobie[165,w], A. Soffer[151], C.A. Solans Sanchez[36], E.Yu. Soldatov[37], U. Soldevila[163], A.A. Solodkov[37], S. Solomon[26], A. Soloshenko[38], K. Solovieva[54], O.V. Solovyanov[40], V. Solovyev[37], P. Sommer[36], A. Sonay[13], W.Y. Song[156b], J.M. Sonneveld[114], A. Sopczak[132], A.L. Sopio[96], F. Sopkova[28b], I.R. Sotarriva Alvarez[154], V. Sothilingam[63a], S. Sottocornola[68], R. Soualah[116b], Z. Soumaimi[35e], D. South[48], N. Soybelman[169], S. Spagnolo[70a,70b], M. Spalla[110], D. Sperlich[54], G. Spigo[36], S. Spinali[91], D.P. Spiteri[59], M. Spousta[133], E.J. Staats[34], A. Stabile[71a,71b], R. Stamen[63a], A. Stampekis[20], M. Standke[24], E. Stanecka[87], M.V. Stange[50], B. Stanislaus[17a], M.M. Stanitzki[48], B. Stapf[48], E.A. Starchenko[37], G.H. Stark[136], J. Stark[102,aa], D.M. Starko[156b], P. Staroba[131],

P. Starovoitov[63a], S. Stärz[104], R. Staszewski[87], G. Stavropoulos[46], J. Steentoft[161], P. Steinberg[29], B. Stelzer[142,156a], H.J. Stelzer[129], O. Stelzer-Chilton[156a], H. Stenzel[58], T.J. Stevenson[146], G.A. Stewart[36], J.R. Stewart[121], M.C. Stockton[36], G. Stoicea[27b], M. Stolarski[130a], S. Stonjek[110], A. Straessner[50], J. Strandberg[144], S. Strandberg[47a,47b], M. Stratmann[171], M. Strauss[120], T. Strebler[102], P. Strizenec[28b], R. Ströhmer[166], D.M. Strom[123], L.R. Strom[48], R. Stroynowski[44], A. Strubig[47a,47b], S.A. Stucci[29], B. Stugu[16], J. Stupak[120], N.A. Styles[48], D. Su[143], S. Su[62a], W. Su[62d], X. Su[62a,66], K. Sugizaki[153], V.V. Sulin[37], M.J. Sullivan[92], D.M.S. Sultan[78a,78b], L. Sultanaliyeva[37], S. Sultansoy[3b], T. Sumida[88], S. Sun[106], S. Sun[170], O. Sunneborn Gudnadottir[161], N. Sur[102], M.R. Sutton[146], H. Suzuki[157], M. Svatos[131], M. Swiatlowski[156a], T. Swirski[166], I. Sykora[28a], M. Sykora[133], T. Sykora[133], D. Ta[100], K. Tackmann[48,t], A. Taffard[160], R. Tafirout[156a], J.S. Tafoya Vargas[66], E.P. Takeva[52], Y. Takubo[84], M. Talby[102], A.A. Talyshev[37], K.C. Tam[64b], N.M. Tamir[151], A. Tanaka[153], J. Tanaka[153], R. Tanaka[66], M. Tanasini[57b,57a], Z. Tao[164], S. Tapia Araya[137f], S. Tapprogge[100], A. Tarek Abouelfadl Mohamed[107], S. Tarem[150], K. Tariq[14a], G. Tarna[102,27b], G.F. Tartarelli[71a], P. Tas[133], M. Tasevsky[131], E. Tassi[43b,43a], A.C. Tate[162], G. Tateno[153], Y. Tayalati[35e,v], G.N. Taylor[105], W. Taylor[156b], H. Teagle[92], A.S. Tee[170], R. Teixeira De Lima[143], P. Teixeira-Dias[95], J.J. Teoh[155], K. Terashi[153], J. Terron[99], S. Terzo[13], M. Testa[53], R.J. Teuscher[155,w], A. Thaler[79], O. Theiner[56], N. Themistokleous[52], T. Theveneaux-Pelzer[102], O. Thielmann[171], D.W. Thomas[95], J.P. Thomas[20], E.A. Thompson[17a], P.D. Thompson[20], E. Thomson[128], Y. Tian[55], V. Tikhomirov[37,a], Yu.A. Tikhonov[37], S. Timoshenko[37], D. Timoshyn[133], E.X.L. Ting[1], P. Tipton[172], S.H. Tlou[33g], A. Tnourji[40], K. Todome[154], S. Todorova-Nova[133], S. Todt[50], M. Togawa[84], J. Tojo[89], S. Tokár[28a], K. Tokushuku[84], O. Toldaiev[68], R. Tombs[32], M. Tomoto[84,111], L. Tompkins[143,n], K.W. Topolnicki[86b], E. Torrence[123], H. Torres[102,aa], E. Torró Pastor[163], M. Toscani[30], C. Tosciri[39], M. Tost[11], D.R. Tovey[139], A. Traeet[16], I.S. Trandafir[27b], T. Trefzger[166], A. Tricoli[29], I.M. Trigger[156a], S. Trincaz-Duvoid[127], D.A. Trischuk[26], B. Trocmé[60], C. Troncon[71a], L. Truong[33c], M. Trzebinski[87], A. Trzupek[87], F. Tsai[145], M. Tsai[106], A. Tsiamis[152,e], P.V. Tsiareshka[37], S. Tsigaridas[156a], A. Tsirigotis[152,r], V. Tsiskaridze[155], E.G. Tskhadadze[149a], M. Tsopoulou[152,e], Y. Tsujikawa[88], I.I. Tsukerman[37], V. Tsulaia[17a], S. Tsuno[84], O. Tsur[150], K. Tsuri[118], D. Tsybychev[145], Y. Tu[64b], A. Tudorache[27b], V. Tudorache[27b], A.N. Tuna[36], S. Turchikhin[57b,57a], I. Turk Cakir[3a], R. Turra[71a], T. Turtuvshin[38,x], P.M. Tuts[41], S. Tzamarias[152,e], P. Tzanis[10], E. Tzovara[100], F. Ukegawa[157], P.A. Ulloa Poblete[137c,137b], E.N. Umaka[29], G. Unal[36], M. Unal[11], A. Undrus[29], G. Unel[160], J. Urban[28b], P. Urquijo[105], P. Urrejola[137a], G. Usai[8], R. Ushioda[154], M. Usman[108], Z. Uysal[21b], V. Vacek[132], B. Vachon[104], K.O.H. Vadla[125], T. Vafeiadis[36], A. Vaitkus[96], C. Valderanis[109], E. Valdes Santurio[47a,47b], M. Valente[156a], S. Valentinetti[23b,23a], A. Valero[163], E. Valiente Moreno[163], A. Vallier[102,aa], J.A. Valls Ferrer[163], D.R. Van Arneman[114], T.R. Van Daalen[138], A. Van Der Graaf[49], P. Van Gemmeren[6], M. Van Rijnbach[125,36], S. Van Stroud[96], I. Van Vulpen[114], M. Vanadia[76a,76b], W. Vandelli[36], M. Vandenbroucke[135], E.R. Vandewall[121], D. Vannicola[151], L. Vannoli[57b,57a], R. Vari[75a], E.W. Varnes[7], C. Varni[17b], T. Varol[148], D. Varouchas[66],

L. Varriale[163], K.E. Varvell[147], M.E. Vasile[27b], L. Vaslin[84], G.A. Vasquez[165], A. Vasyukov[38], F. Vazeille[40], T. Vazquez Schroeder[36], J. Veatch[31], V. Vecchio[101], M.J. Veen[103], I. Veliscek[126], L.M. Veloce[155], F. Veloso[130a,130c], S. Veneziano[75a], A. Ventura[70a,70b], S. Ventura Gonzalez[135], A. Verbytskyi[110], M. Verducci[74a,74b], C. Vergis[24], M. Verissimo De Araujo[83b], W. Verkerke[114], J.C. Vermeulen[114], C. Vernieri[143], M. Vessella[103], M.C. Vetterli[142,ag], A. Vgenopoulos[152,e], N. Viaux Maira[137f], T. Vickey[139], O.E. Vickey Boeriu[139], G.H.A. Viehhauser[126], L. Vigani[63b], M. Villa[23b,23a], M. Villaplana Perez[163], E.M. Villhauer[52], E. Vilucchi[53], M.G. Vincter[34], G.S. Virdee[20], A. Vishwakarma[52], A. Visibile[114], C. Vittori[36], I. Vivarelli[146], E. Voevodina[110], F. Vogel[109], J.C. Voigt[50], P. Vokac[132], Yu. Volkotrub[86a], J. Von Ahnen[48], E. Von Toerne[24], B. Vormwald[36], V. Vorobel[133], K. Vorobev[37], M. Vos[163], K. Voss[141], J.H. Vossebeld[92], M. Vozak[114], L. Vozdecky[94], N. Vranjes[15], M. Vranjes Milosavljevic[15], M. Vreeswijk[114], R. Vuillermet[36], O. Vujinovic[100], I. Vukotic[39], S. Wada[157], C. Wagner[103], J.M. Wagner[17a], W. Wagner[171], S. Wahdan[171], H. Wahlberg[90], M. Wakida[111], J. Walder[134], R. Walker[109], W. Walkowiak[141], A. Wall[128], T. Wamorkar[6], A.Z. Wang[136], C. Wang[100], C. Wang[62c], H. Wang[17a], J. Wang[64a], R.-J. Wang[100], R. Wang[61], R. Wang[6], S.M. Wang[148], S. Wang[62b], T. Wang[62a], W.T. Wang[80], W. Wang[14a], X. Wang[14c], X. Wang[162], X. Wang[62c], Y. Wang[62d], Y. Wang[14c], Z. Wang[106], Z. Wang[62d,51,62c], Z. Wang[106], A. Warburton[104], R.J. Ward[20], N. Warrack[59], A.T. Watson[20], H. Watson[59], M.F. Watson[20], E. Watton[59,134], G. Watts[138], B.M. Waugh[96], C. Weber[29], H.A. Weber[18], M.S. Weber[19], S.M. Weber[63a], C. Wei[62a], Y. Wei[126], A.R. Weidberg[126], E.J. Weik[117], J. Weingarten[49], M. Weirich[100], C. Weiser[54], C.J. Wells[48], T. Wenaus[29], B. Wendland[49], T. Wengler[36], N.S. Wenke[110], N. Wermes[24], M. Wessels[63a], A.M. Wharton[91], A.S. White[61], A. White[8], M.J. White[1], D. Whiteson[160], L. Wickremasinghe[124], W. Wiedenmann[170], C. Wiel[50], M. Wielers[134], C. Wiglesworth[42], D.J. Wilbern[120], H.G. Wilkens[36], D.M. Williams[41], H.H. Williams[128], S. Williams[32], S. Willocq[103], B.J. Wilson[101], P.J. Windischhofer[39], F.I. Winkel[30], F. Winklmeier[123], B.T. Winter[54], J.K. Winter[101], M. Wittgen[143], M. Wobisch[97], Z. Wolffs[114], J. Wollrath[160], M.W. Wolter[87], H. Wolters[130a,130c], A.F. Wongel[48], E.L. Woodward[41], S.D. Worm[48], B.K. Wosiek[87], K.W. Woźniak[87], S. Wozniewski[55], K. Wraight[59], C. Wu[20], J. Wu[14a,14e], M. Wu[64a], M. Wu[113], S.L. Wu[170], X. Wu[56], Y. Wu[62a], Z. Wu[135], J. Wuerzinger[110,ae], T.R. Wyatt[101], B.M. Wynne[52], S. Xella[42], L. Xia[14c], M. Xia[14b], J. Xiang[64c], M. Xie[62a], X. Xie[62a], S. Xin[14a,14e], A. Xiong[123], J. Xiong[17a], D. Xu[14a], H. Xu[62a], L. Xu[62a], R. Xu[128], T. Xu[106], Y. Xu[14b], Z. Xu[52], Z. Xu[14a], Z. Xu[14c], B. Yabsley[147], S. Yacoob[33a], Y. Yamaguchi[154], E. Yamashita[153], H. Yamauchi[157], T. Yamazaki[17a], Y. Yamazaki[85], J. Yan[62c], S. Yan[126], Z. Yan[25], H.J. Yang[62c,62d], H.T. Yang[62a], S. Yang[62a], T. Yang[64c], X. Yang[36], X. Yang[14a], Y. Yang[44], Y. Yang[62a], Z. Yang[62a], W-M. Yao[17a], Y.C. Yap[48], H. Ye[14c], H. Ye[55], J. Ye[14a], S. Ye[29], X. Ye[62a], Y. Yeh[96], I. Yeletskikh[38], B.K. Yeo[17b], M.R. Yexley[96], P. Yin[41], K. Yorita[168], S. Younas[27b], C.J.S. Young[36], C. Young[143], C. Yu[14a,14e,ai], Y. Yu[62a], M. Yuan[106], R. Yuan[62b], L. Yue[96], M. Zaazoua[62a], B. Zabinski[87], E. Zaid[52], T. Zakareishvili[149b], N. Zakharchuk[34], S. Zambito[56], J.A. Zamora Saa[137d,137b], J. Zang[153], D. Zanzi[54], O. Zaplatilek[132], C. Zeitnitz[171], H. Zeng[14a], J.C. Zeng[162], D.T. Zenger Jr[26], O. Zenin[37], T. Ženiš[28a],

JHEP05(2024)162

S. Zenz[94], S. Zerradi[35a], D. Zerwas[66], M. Zhai[14a,14e], B. Zhang[14c], D.F. Zhang[139], J. Zhang[62b], J. Zhang[6], K. Zhang[14a,14e], L. Zhang[14c], P. Zhang[14a,14e], R. Zhang[170], S. Zhang[106], S. Zhang[44], T. Zhang[153], X. Zhang[62c], X. Zhang[62b], Y. Zhang[62c,5], Y. Zhang[96], Y. Zhang[14c], Z. Zhang[17a], Z. Zhang[66], H. Zhao[138], P. Zhao[51], T. Zhao[62b], Y. Zhao[136], Z. Zhao[62a], A. Zhemchugov[38], J. Zheng[14c], K. Zheng[162], X. Zheng[62a], Z. Zheng[143], D. Zhong[162], B. Zhou[106], H. Zhou[7], N. Zhou[62c], Y. Zhou[7], C.G. Zhu[62b], J. Zhu[106], Y. Zhu[62c], Y. Zhu[62a], X. Zhuang[14a], K. Zhukov[37], V. Zhulanov[37], N.I. Zimine[38], J. Zinsser[63b], M. Ziolkowski[141], L. Živković[15], A. Zoccoli[23b,23a], K. Zoch[61], T.G. Zorbas[139], O. Zormpa[46], W. Zou[41], L. Zwalinski[36]

[1] *Department of Physics, University of Adelaide, Adelaide; Australia*
[2] *Department of Physics, University of Alberta, Edmonton AB; Canada*
[3] [(a)] *Department of Physics, Ankara University, Ankara;*[(b)] *Division of Physics, TOBB University of Economics and Technology, Ankara; Türkiye*
[4] *LAPP, Université Savoie Mont Blanc, CNRS/IN2P3, Annecy; France*
[5] *APC, Université Paris Cité, CNRS/IN2P3, Paris; France*
[6] *High Energy Physics Division, Argonne National Laboratory, Argonne IL; United States of America*
[7] *Department of Physics, University of Arizona, Tucson AZ; United States of America*
[8] *Department of Physics, University of Texas at Arlington, Arlington TX; United States of America*
[9] *Physics Department, National and Kapodistrian University of Athens, Athens; Greece*
[10] *Physics Department, National Technical University of Athens, Zografou; Greece*
[11] *Department of Physics, University of Texas at Austin, Austin TX; United States of America*
[12] *Institute of Physics, Azerbaijan Academy of Sciences, Baku; Azerbaijan*
[13] *Institut de Física d'Altes Energies (IFAE), Barcelona Institute of Science and Technology, Barcelona; Spain*
[14] [(a)] *Institute of High Energy Physics, Chinese Academy of Sciences, Beijing;*[(b)] *Physics Department, Tsinghua University, Beijing;*[(c)] *Department of Physics, Nanjing University, Nanjing;*[(d)] *School of Science, Shenzhen Campus of Sun Yat-sen University;*[(e)] *University of Chinese Academy of Science (UCAS), Beijing; China*
[15] *Institute of Physics, University of Belgrade, Belgrade; Serbia*
[16] *Department for Physics and Technology, University of Bergen, Bergen; Norway*
[17] [(a)] *Physics Division, Lawrence Berkeley National Laboratory, Berkeley CA;*[(b)] *University of California, Berkeley CA; United States of America*
[18] *Institut für Physik, Humboldt Universität zu Berlin, Berlin; Germany*
[19] *Albert Einstein Center for Fundamental Physics and Laboratory for High Energy Physics, University of Bern, Bern; Switzerland*
[20] *School of Physics and Astronomy, University of Birmingham, Birmingham; United Kingdom*
[21] [(a)] *Department of Physics, Bogazici University, Istanbul;*[(b)] *Department of Physics Engineering, Gaziantep University, Gaziantep;*[(c)] *Department of Physics, Istanbul University, Istanbul; Türkiye*
[22] [(a)] *Facultad de Ciencias y Centro de Investigaciónes, Universidad Antonio Nariño, Bogotá;*[(b)] *Departamento de Física, Universidad Nacional de Colombia, Bogotá; Colombia*
[23] [(a)] *Dipartimento di Fisica e Astronomia A. Righi, Università di Bologna, Bologna;*[(b)] *INFN Sezione di Bologna; Italy*
[24] *Physikalisches Institut, Universität Bonn, Bonn; Germany*
[25] *Department of Physics, Boston University, Boston MA; United States of America*
[26] *Department of Physics, Brandeis University, Waltham MA; United States of America*
[27] [(a)] *Transilvania University of Brasov, Brasov;*[(b)] *Horia Hulubei National Institute of Physics and Nuclear Engineering, Bucharest;*[(c)] *Department of Physics, Alexandru Ioan Cuza University of Iasi, Iasi;*[(d)] *National Institute for Research and Development of Isotopic and Molecular Technologies, Physics Department, Cluj-Napoca;*[(e)] *National University of Science and Technology Politechnica, Bucharest;*[(f)] *West University in Timisoara, Timisoara;*[(g)] *Faculty of Physics, University of Bucharest, Bucharest; Romania*

JHEP05(2024)162

[28] [a] Faculty of Mathematics, Physics and Informatics, Comenius University, Bratislava;[b] Department of Subnuclear Physics, Institute of Experimental Physics of the Slovak Academy of Sciences, Kosice; Slovak Republic
[29] Physics Department, Brookhaven National Laboratory, Upton NY; United States of America
[30] Universidad de Buenos Aires, Facultad de Ciencias Exactas y Naturales, Departamento de Física, y CONICET, Instituto de Física de Buenos Aires (IFIBA), Buenos Aires; Argentina
[31] California State University, CA; United States of America
[32] Cavendish Laboratory, University of Cambridge, Cambridge; United Kingdom
[33] [a] Department of Physics, University of Cape Town, Cape Town;[b] iThemba Labs, Western Cape;[c] Department of Mechanical Engineering Science, University of Johannesburg, Johannesburg;[d] National Institute of Physics, University of the Philippines Diliman (Philippines);[e] University of South Africa, Department of Physics, Pretoria;[f] University of Zululand, KwaDlangezwa;[g] School of Physics, University of the Witwatersrand, Johannesburg; South Africa
[34] Department of Physics, Carleton University, Ottawa ON; Canada
[35] [a] Faculté des Sciences Ain Chock, Réseau Universitaire de Physique des Hautes Energies — Université Hassan II, Casablanca;[b] Faculté des Sciences, Université Ibn-Tofail, Kénitra;[c] Faculté des Sciences Semlalia, Université Cadi Ayyad, LPHEA-Marrakech;[d] LPMR, Faculté des Sciences, Université Mohamed Premier, Oujda;[e] Faculté des sciences, Université Mohammed V, Rabat;[f] Institute of Applied Physics, Mohammed VI Polytechnic University, Ben Guerir; Morocco
[36] CERN, Geneva; Switzerland
[37] Affiliated with an institute covered by a cooperation agreement with CERN
[38] Affiliated with an international laboratory covered by a cooperation agreement with CERN
[39] Enrico Fermi Institute, University of Chicago, Chicago IL; United States of America
[40] LPC, Université Clermont Auvergne, CNRS/IN2P3, Clermont-Ferrand; France
[41] Nevis Laboratory, Columbia University, Irvington NY; United States of America
[42] Niels Bohr Institute, University of Copenhagen, Copenhagen; Denmark
[43] [a] Dipartimento di Fisica, Università della Calabria, Rende;[b] INFN Gruppo Collegato di Cosenza, Laboratori Nazionali di Frascati; Italy
[44] Physics Department, Southern Methodist University, Dallas TX; United States of America
[45] Physics Department, University of Texas at Dallas, Richardson TX; United States of America
[46] National Centre for Scientific Research "Demokritos", Agia Paraskevi; Greece
[47] [a] Department of Physics, Stockholm University;[b] Oskar Klein Centre, Stockholm; Sweden
[48] Deutsches Elektronen-Synchrotron DESY, Hamburg and Zeuthen; Germany
[49] Fakultät Physik, Technische Universität Dortmund, Dortmund; Germany
[50] Institut für Kern- und Teilchenphysik, Technische Universität Dresden, Dresden; Germany
[51] Department of Physics, Duke University, Durham NC; United States of America
[52] SUPA — School of Physics and Astronomy, University of Edinburgh, Edinburgh; United Kingdom
[53] INFN e Laboratori Nazionali di Frascati, Frascati; Italy
[54] Physikalisches Institut, Albert-Ludwigs-Universität Freiburg, Freiburg; Germany
[55] II. Physikalisches Institut, Georg-August-Universität Göttingen, Göttingen; Germany
[56] Département de Physique Nucléaire et Corpusculaire, Université de Genève, Genève; Switzerland
[57] [a] Dipartimento di Fisica, Università di Genova, Genova;[b] INFN Sezione di Genova; Italy
[58] II. Physikalisches Institut, Justus-Liebig-Universität Giessen, Giessen; Germany
[59] SUPA — School of Physics and Astronomy, University of Glasgow, Glasgow; United Kingdom
[60] LPSC, Université Grenoble Alpes, CNRS/IN2P3, Grenoble INP, Grenoble; France
[61] Laboratory for Particle Physics and Cosmology, Harvard University, Cambridge MA; United States of America
[62] [a] Department of Modern Physics and State Key Laboratory of Particle Detection and Electronics, University of Science and Technology of China, Hefei;[b] Institute of Frontier and Interdisciplinary Science and Key Laboratory of Particle Physics and Particle Irradiation (MOE), Shandong University, Qingdao;[c] School of Physics and Astronomy, Shanghai Jiao Tong University, Key Laboratory for Particle Astrophysics and Cosmology (MOE), SKLPPC, Shanghai;[d] Tsung-Dao Lee Institute, Shanghai; China
[63] [a] Kirchhoff-Institut für Physik, Ruprecht-Karls-Universität Heidelberg, Heidelberg;[b] Physikalisches Institut, Ruprecht-Karls-Universität Heidelberg, Heidelberg; Germany

JHEP05(2024)162

[64] [(a)] *Department of Physics, Chinese University of Hong Kong, Shatin, N.T., Hong Kong;* [(b)] *Department of Physics, University of Hong Kong, Hong Kong;* [(c)] *Department of Physics and Institute for Advanced Study, Hong Kong University of Science and Technology, Clear Water Bay, Kowloon, Hong Kong; China*
[65] *Department of Physics, National Tsing Hua University, Hsinchu; Taiwan*
[66] *IJCLab, Université Paris-Saclay, CNRS/IN2P3, 91405, Orsay; France*
[67] *Centro Nacional de Microelectrónica (IMB-CNM-CSIC), Barcelona; Spain*
[68] *Department of Physics, Indiana University, Bloomington IN; United States of America*
[69] [(a)] *INFN Gruppo Collegato di Udine, Sezione di Trieste, Udine;* [(b)] *ICTP, Trieste;* [(c)] *Dipartimento Politecnico di Ingegneria e Architettura, Università di Udine, Udine; Italy*
[70] [(a)] *INFN Sezione di Lecce;* [(b)] *Dipartimento di Matematica e Fisica, Università del Salento, Lecce; Italy*
[71] [(a)] *INFN Sezione di Milano;* [(b)] *Dipartimento di Fisica, Università di Milano, Milano; Italy*
[72] [(a)] *INFN Sezione di Napoli;* [(b)] *Dipartimento di Fisica, Università di Napoli, Napoli; Italy*
[73] [(a)] *INFN Sezione di Pavia;* [(b)] *Dipartimento di Fisica, Università di Pavia, Pavia; Italy*
[74] [(a)] *INFN Sezione di Pisa;* [(b)] *Dipartimento di Fisica E. Fermi, Università di Pisa, Pisa; Italy*
[75] [(a)] *INFN Sezione di Roma;* [(b)] *Dipartimento di Fisica, Sapienza Università di Roma, Roma; Italy*
[76] [(a)] *INFN Sezione di Roma Tor Vergata;* [(b)] *Dipartimento di Fisica, Università di Roma Tor Vergata, Roma; Italy*
[77] [(a)] *INFN Sezione di Roma Tre;* [(b)] *Dipartimento di Matematica e Fisica, Università Roma Tre, Roma; Italy*
[78] [(a)] *INFN-TIFPA;* [(b)] *Università degli Studi di Trento, Trento; Italy*
[79] *Universität Innsbruck, Department of Astro and Particle Physics, Innsbruck; Austria*
[80] *University of Iowa, Iowa City IA; United States of America*
[81] *Department of Physics and Astronomy, Iowa State University, Ames IA; United States of America*
[82] *Istinye University, Sariyer, Istanbul; Türkiye*
[83] [(a)] *Departamento de Engenharia Elétrica, Universidade Federal de Juiz de Fora (UFJF), Juiz de Fora;* [(b)] *Universidade Federal do Rio De Janeiro COPPE/EE/IF, Rio de Janeiro;* [(c)] *Instituto de Física, Universidade de São Paulo, São Paulo;* [(d)] *Rio de Janeiro State University, Rio de Janeiro; Brazil*
[84] *KEK, High Energy Accelerator Research Organization, Tsukuba; Japan*
[85] *Graduate School of Science, Kobe University, Kobe; Japan*
[86] [(a)] *AGH University of Krakow, Faculty of Physics and Applied Computer Science, Krakow;* [(b)] *Marian Smoluchowski Institute of Physics, Jagiellonian University, Krakow; Poland*
[87] *Institute of Nuclear Physics Polish Academy of Sciences, Krakow; Poland*
[88] *Faculty of Science, Kyoto University, Kyoto; Japan*
[89] *Research Center for Advanced Particle Physics and Department of Physics, Kyushu University, Fukuoka; Japan*
[90] *Instituto de Física La Plata, Universidad Nacional de La Plata and CONICET, La Plata; Argentina*
[91] *Physics Department, Lancaster University, Lancaster; United Kingdom*
[92] *Oliver Lodge Laboratory, University of Liverpool, Liverpool; United Kingdom*
[93] *Department of Experimental Particle Physics, Jožef Stefan Institute and Department of Physics, University of Ljubljana, Ljubljana; Slovenia*
[94] *School of Physics and Astronomy, Queen Mary University of London, London; United Kingdom*
[95] *Department of Physics, Royal Holloway University of London, Egham; United Kingdom*
[96] *Department of Physics and Astronomy, University College London, London; United Kingdom*
[97] *Louisiana Tech University, Ruston LA; United States of America*
[98] *Fysiska institutionen, Lunds universitet, Lund; Sweden*
[99] *Departamento de Física Teorica C-15 and CIAFF, Universidad Autónoma de Madrid, Madrid; Spain*
[100] *Institut für Physik, Universität Mainz, Mainz; Germany*
[101] *School of Physics and Astronomy, University of Manchester, Manchester; United Kingdom*
[102] *CPPM, Aix-Marseille Université, CNRS/IN2P3, Marseille; France*
[103] *Department of Physics, University of Massachusetts, Amherst MA; United States of America*
[104] *Department of Physics, McGill University, Montreal QC; Canada*
[105] *School of Physics, University of Melbourne, Victoria; Australia*
[106] *Department of Physics, University of Michigan, Ann Arbor MI; United States of America*

JHEP05(2024)162

[107] Department of Physics and Astronomy, Michigan State University, East Lansing MI; United States of America
[108] Group of Particle Physics, University of Montreal, Montreal QC; Canada
[109] Fakultät für Physik, Ludwig-Maximilians-Universität München, München; Germany
[110] Max-Planck-Institut für Physik (Werner-Heisenberg-Institut), München; Germany
[111] Graduate School of Science and Kobayashi-Maskawa Institute, Nagoya University, Nagoya; Japan
[112] Department of Physics and Astronomy, University of New Mexico, Albuquerque NM; United States of America
[113] Institute for Mathematics, Astrophysics and Particle Physics, Radboud University/Nikhef, Nijmegen; Netherlands
[114] Nikhef National Institute for Subatomic Physics and University of Amsterdam, Amsterdam; Netherlands
[115] Department of Physics, Northern Illinois University, DeKalb IL; United States of America
[116] [a] New York University Abu Dhabi, Abu Dhabi; [b] University of Sharjah, Sharjah; United Arab Emirates
[117] Department of Physics, New York University, New York NY; United States of America
[118] Ochanomizu University, Otsuka, Bunkyo-ku, Tokyo; Japan
[119] Ohio State University, Columbus OH; United States of America
[120] Homer L. Dodge Department of Physics and Astronomy, University of Oklahoma, Norman OK; United States of America
[121] Department of Physics, Oklahoma State University, Stillwater OK; United States of America
[122] Palacký University, Joint Laboratory of Optics, Olomouc; Czech Republic
[123] Institute for Fundamental Science, University of Oregon, Eugene, OR; United States of America
[124] Graduate School of Science, Osaka University, Osaka; Japan
[125] Department of Physics, University of Oslo, Oslo; Norway
[126] Department of Physics, Oxford University, Oxford; United Kingdom
[127] LPNHE, Sorbonne Université, Université Paris Cité, CNRS/IN2P3, Paris; France
[128] Department of Physics, University of Pennsylvania, Philadelphia PA; United States of America
[129] Department of Physics and Astronomy, University of Pittsburgh, Pittsburgh PA; United States of America
[130] [a] Laboratório de Instrumentação e Física Experimental de Partículas — LIP, Lisboa; [b] Departamento de Física, Faculdade de Ciências, Universidade de Lisboa, Lisboa; [c] Departamento de Física, Universidade de Coimbra, Coimbra; [d] Centro de Física Nuclear da Universidade de Lisboa, Lisboa; [e] Departamento de Física, Universidade do Minho, Braga; [f] Departamento de Física Teórica y del Cosmos, Universidad de Granada, Granada (Spain); [g] Departamento de Física, Instituto Superior Técnico, Universidade de Lisboa, Lisboa; Portugal
[131] Institute of Physics of the Czech Academy of Sciences, Prague; Czech Republic
[132] Czech Technical University in Prague, Prague; Czech Republic
[133] Charles University, Faculty of Mathematics and Physics, Prague; Czech Republic
[134] Particle Physics Department, Rutherford Appleton Laboratory, Didcot; United Kingdom
[135] IRFU, CEA, Université Paris-Saclay, Gif-sur-Yvette; France
[136] Santa Cruz Institute for Particle Physics, University of California Santa Cruz, Santa Cruz CA; United States of America
[137] [a] Departamento de Física, Pontificia Universidad Católica de Chile, Santiago; [b] Millennium Institute for Subatomic physics at high energy frontier (SAPHIR), Santiago; [c] Instituto de Investigación Multidisciplinario en Ciencia y Tecnología, y Departamento de Física, Universidad de La Serena; [d] Universidad Andres Bello, Department of Physics, Santiago; [e] Instituto de Alta Investigación, Universidad de Tarapacá, Arica; [f] Departamento de Física, Universidad Técnica Federico Santa María, Valparaíso; Chile
[138] Department of Physics, University of Washington, Seattle WA; United States of America
[139] Department of Physics and Astronomy, University of Sheffield, Sheffield; United Kingdom
[140] Department of Physics, Shinshu University, Nagano; Japan
[141] Department Physik, Universität Siegen, Siegen; Germany
[142] Department of Physics, Simon Fraser University, Burnaby BC; Canada
[143] SLAC National Accelerator Laboratory, Stanford CA; United States of America
[144] Department of Physics, Royal Institute of Technology, Stockholm; Sweden

JHEP05(2024)162

[145] *Departments of Physics and Astronomy, Stony Brook University, Stony Brook NY; United States of America*
[146] *Department of Physics and Astronomy, University of Sussex, Brighton; United Kingdom*
[147] *School of Physics, University of Sydney, Sydney; Australia*
[148] *Institute of Physics, Academia Sinica, Taipei; Taiwan*
[149] [(a)] *E. Andronikashvili Institute of Physics, Iv. Javakhishvili Tbilisi State University, Tbilisi;* [(b)] *High Energy Physics Institute, Tbilisi State University, Tbilisi;* [(c)] *University of Georgia, Tbilisi; Georgia*
[150] *Department of Physics, Technion, Israel Institute of Technology, Haifa; Israel*
[151] *Raymond and Beverly Sackler School of Physics and Astronomy, Tel Aviv University, Tel Aviv; Israel*
[152] *Department of Physics, Aristotle University of Thessaloniki, Thessaloniki; Greece*
[153] *International Center for Elementary Particle Physics and Department of Physics, University of Tokyo, Tokyo; Japan*
[154] *Department of Physics, Tokyo Institute of Technology, Tokyo; Japan*
[155] *Department of Physics, University of Toronto, Toronto ON; Canada*
[156] [(a)] *TRIUMF, Vancouver BC;* [(b)] *Department of Physics and Astronomy, York University, Toronto ON; Canada*
[157] *Division of Physics and Tomonaga Center for the History of the Universe, Faculty of Pure and Applied Sciences, University of Tsukuba, Tsukuba; Japan*
[158] *Department of Physics and Astronomy, Tufts University, Medford MA; United States of America*
[159] *United Arab Emirates University, Al Ain; United Arab Emirates*
[160] *Department of Physics and Astronomy, University of California Irvine, Irvine CA; United States of America*
[161] *Department of Physics and Astronomy, University of Uppsala, Uppsala; Sweden*
[162] *Department of Physics, University of Illinois, Urbana IL; United States of America*
[163] *Instituto de Física Corpuscular (IFIC), Centro Mixto Universidad de Valencia — CSIC, Valencia; Spain*
[164] *Department of Physics, University of British Columbia, Vancouver BC; Canada*
[165] *Department of Physics and Astronomy, University of Victoria, Victoria BC; Canada*
[166] *Fakultät für Physik und Astronomie, Julius-Maximilians-Universität Würzburg, Würzburg; Germany*
[167] *Department of Physics, University of Warwick, Coventry; United Kingdom*
[168] *Waseda University, Tokyo; Japan*
[169] *Department of Particle Physics and Astrophysics, Weizmann Institute of Science, Rehovot; Israel*
[170] *Department of Physics, University of Wisconsin, Madison WI; United States of America*
[171] *Fakultät für Mathematik und Naturwissenschaften, Fachgruppe Physik, Bergische Universität Wuppertal, Wuppertal; Germany*
[172] *Department of Physics, Yale University, New Haven CT; United States of America*

[a] *Also Affiliated with an institute covered by a cooperation agreement with CERN*
[b] *Also at An-Najah National University, Nablus; Palestine*
[c] *Also at Borough of Manhattan Community College, City University of New York, New York NY; United States of America*
[d] *Also at Center for High Energy Physics, Peking University; China*
[e] *Also at Center for Interdisciplinary Research and Innovation (CIRI-AUTH), Thessaloniki; Greece*
[f] *Also at Centro Studi e Ricerche Enrico Fermi; Italy*
[g] *Also at CERN, Geneva; Switzerland*
[h] *Also at Département de Physique Nucléaire et Corpusculaire, Université de Genève, Genève; Switzerland*
[i] *Also at Departament de Fisica de la Universitat Autonoma de Barcelona, Barcelona; Spain*
[j] *Also at Department of Financial and Management Engineering, University of the Aegean, Chios; Greece*
[k] *Also at Department of Physics, Ben Gurion University of the Negev, Beer Sheva; Israel*
[l] *Also at Department of Physics, California State University, Sacramento; United States of America*
[m] *Also at Department of Physics, King's College London, London; United Kingdom*
[n] *Also at Department of Physics, Stanford University, Stanford CA; United States of America*
[o] *Also at Department of Physics, University of Fribourg, Fribourg; Switzerland*
[p] *Also at Department of Physics, University of Thessaly; Greece*
[q] *Also at Department of Physics, Westmont College, Santa Barbara; United States of America*

JHEP05(2024)162

[r] Also at Hellenic Open University, Patras; Greece
[s] Also at Institucio Catalana de Recerca i Estudis Avancats, ICREA, Barcelona; Spain
[t] Also at Institut für Experimentalphysik, Universität Hamburg, Hamburg; Germany
[u] Also at Institute for Nuclear Research and Nuclear Energy (INRNE) of the Bulgarian Academy of Sciences, Sofia; Bulgaria
[v] Also at Institute of Applied Physics, Mohammed VI Polytechnic University, Ben Guerir; Morocco
[w] Also at Institute of Particle Physics (IPP); Canada
[x] Also at Institute of Physics and Technology, Mongolian Academy of Sciences, Ulaanbaatar; Mongolia
[y] Also at Institute of Physics, Azerbaijan Academy of Sciences, Baku; Azerbaijan
[z] Also at Institute of Theoretical Physics, Ilia State University, Tbilisi; Georgia
[aa] Also at L2IT, Université de Toulouse, CNRS/IN2P3, UPS, Toulouse; France
[ab] Also at Lawrence Livermore National Laboratory, Livermore; United States of America
[ac] Also at National Institute of Physics, University of the Philippines Diliman (Philippines); Philippines
[ad] Also at Ochanomizu University, Otsuka, Bunkyo-ku, Tokyo; Japan
[ae] Also at Technical University of Munich, Munich; Germany
[af] Also at The Collaborative Innovation Center of Quantum Matter (CICQM), Beijing; China
[ag] Also at TRIUMF, Vancouver BC; Canada
[ah] Also at Università di Napoli Parthenope, Napoli; Italy
[ai] Also at University of Chinese Academy of Sciences (UCAS), Beijing; China
[aj] Also at University of Colorado Boulder, Department of Physics, Colorado; United States of America
[ak] Also at Washington College, Chestertown, MD; United States of America
[al] Also at Yeditepe University, Physics Department, Istanbul; Türkiye
[*] Deceased

JHEP05(2024)162